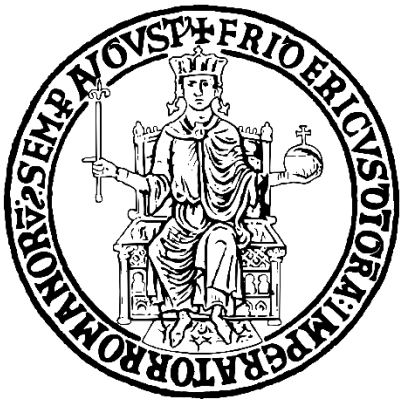

UNIVERSITÀ DEGLI STUDI DI NAPOLI FEDERICO II

DOTTORATO IN INGEGNERIA INDUSTRIALE

XXXVI CICLO

Settore Scientifico Disciplinare: ING-IND/05
Impianti e Sistemi Aerospaziali

SENSING AND DATA FUSION FOR DETECT AND AVOID AND MULTI-UAV COOPERATION IN LOW ALTITUDE ENVIRONMENTS

Federica Vitiello

Relatori

Prof. Giancarmine Fasano
Prof. Roberto Opromolla
Ing. Flavia Causa

Coordinatore

Prof. Michele Grassi

A Gilda,
che sia anche il tuo traguardo

Keywords

Unmanned Aerial Vehicles, Detect And Avoid, Sense And Avoid, Data Fusion, Tracking, Detection, RADAR, Visual Camera, Urban Air Mobility, Advanced Air Mobility, multi-UAV Cooperation.

Abstract

UAVs can undoubtedly bring benefits and advantages in many fields by completing tasks which are considered too dull, dirty and dangerous for human operators while offering a fertile technological ground for the development of innovative applications. Still, the safety of their missions, which foresee their integration in both controlled and uncontrolled civil airspace, is not keeping the pace with their increasing popularity, which is also pushing towards their exponential deployment in urban areas. This is all the more crucial if novel concepts for UAV-based air transportation methods, such as AAM and UAM, are considered. In these latter cases, high volumes of operations are forecasted to occur mostly in low altitude conditions. In these frameworks, DAA and navigation strategies must be designed to enable safe flights of UAVs by providing detection and collision avoidance solutions, with the former, and reliable navigation, with the latter, thus finally unleashing the full autonomous potential of these novel platforms. These two aspects are the major focuses of this thesis.

As far as DAA is concerned, the performance assessment of non-cooperative technologies for the detection and tracking of sUAVs flying in low altitude conditions is tackled. The sensing setup chosen for the application consists of visual cameras and low SWaP RADARs whose performance are analysed both on numerical and experimental bases. The tests clearly show limitations in the standalone implementation of the two sensors, paid in terms of absent distance estimates, for the camera, and coarse angular accuracy, for the RADAR. Innovative fusion solutions are therefore proposed and tested offline on experimental data during ground-to-air campaigns with a low-altitude-flying sUAV. The strategies provide improvements in the angular accuracy of the RADAR-based tracking estimates which likewise positively impacts conflict detection. The experimental approach used for the evaluation sheds a light over the effects of clutter on RADAR data, whose mitigation is either achieved with filtering and centroiding pre-processing steps or by adopting additional RADAR/visual fusion steps acting at detection level. The strategies tested can be also used in the context of AAM/UAM surveillance where performance of distributed sensing exploiting a network of

ground-based RADARs and cameras are assessed. In this case, improvements in terms of track coverage can be achieved by adopting fusion solutions which take advantage of the spatial disposition of the sensors. An innovative solution based on a leader-helper approach is used to improve the track coverage of a single RADAR by injecting measurements from another RADAR comprised in the network. Nevertheless, when multiple RADARs operate with overlapping Fields of View, interference can occur. Therefore, a preliminary strategy to filter interference-affected RADAR measurements is also proposed.

Finally, in the framework of cooperation between multiple UAVs, a "chief-deputy" approach for calibration of onboard magnetometers is designed. The latter foresees a rotation of the chief platform around the deputy to capture relative positioning information by means of visual cameras and GNSS data processing. These can be used to evaluate both onboard and external magnetic disturbances which, if not accounted for, can spoil the quality of heading angle estimates. The strategy proves its efficacy in retrieving sub-degree pointing errors when ground-based and airborne targets are used as control points, thus exceeding the performance of both uncalibrated heading, which does not account for the disturbances, and navigation filter-estimated heading.

Table of Contents

List of Figures

List of Tables

Acknowledgements

Durante la stesura di questa tesi ho rivissuto questi ultimi incredibili tre anni, con buona probabilità i più formativi fino ad oggi. Anni di crescita sfrenata, professionale quanto personale, che mi hanno vista cambiare irreversibilmente, regalandomi la consapevolezza che l'impegno e la determinazione siano gli strumenti più potenti per conseguire successi a volte inimmaginabili. Anni di insegnamenti fondamentali, che hanno confermato quanto il traguardo possa essere raggiunto solo mettendosi alla prova, riformulando l'ansia e la paura per spingere piuttosto che frenare, fallendo, se necessario (a volte auspicabilmente), e condividendo le lezioni imparate, sempre.

I successi, piccoli e grandi, raggiunti durante questo percorso e la trasformazione (tutt'ora in atto) da esso provocata non sarebbero mai stati possibili senza la fitta rete di affetti che, in questi anni, ha assunto la difficile e duale funzione di paracadute e trampolino di lancio. In questo piccolo spazio vorrei quindi dedicare poche ma profondamente sentite parole per ringraziare i nodi di questa rete: le persone che hanno vegliato su di me e senza le quali il volo sarebbe stato sicuramente più arduo, a tratti impossibile.

Il primo ringraziamento va alla mia squadra di supervisori, indispensabili sensori le cui "misure" fuse hanno garantito l'evoluzione della mia traiettoria da un mero tentativo ad un'accurata conferma. Giancarmine, grazie per avermi riportata in bassa quota, spalancando le porte di un mondo nel quale ho ritrovato la mia dimensione ideale con l'aiuto della tua passione per la ricerca, infusa a suon di rock, racconti e consigli. Roberto, grazie per il tuo sostegno che, tra uno scherzo e una risata, mi ha spronata a testare le mie idee senza darmi subito per vinta, facendo sì che riconoscessi il mio valore e iniziassi (finalmente) a credere nelle mie capacità. Flavia, grazie per essere stata la mia spalla, la mia ala protettrice e il mio spirito guida sin dall'inizio, diventando un'amica sincera e preziosa e un esempio di creatività e determinazione al quale farò sempre riferimento.

Infinite grazie ai ragazzi del GNC lab per avermi accompagnata durante questo percorso, condividendo le gioie dei suoi alti e le frustrazioni dei suoi bassi.

L’ambiente familiare che abbiamo creato, le attività ricreative di “team building”, il divertimento, l’innegabile affetto e l’incessante condivisione delle conoscenze acquisite sono la riconferma che il mondo accademico, notoriamente tra i più competitivi, può essere un campo fertile per amicizie straordinarie.

Un ringraziamento speciale a Chester Dolph e il team di ricercatori del Aeronautics Systems Engineering Branch di NASA Langley che mi hanno accolta ed inclusa in un emozionante ambiente di ricerca, facendo avverare il sogno di “essere alla NASA”.

Il ringraziamento più sentito va alla mia famiglia, l’inesauribile sorgente d’amore dalla quale traggo forza e coraggio quotidianamente. Ai miei genitori, per l’assidua presenza e le immancabili parole di incoraggiamento che da sempre illuminano la via. A Marta, la mia più tenace sostenitrice, il cui cuore grande non smette mai di sorprendermi facendomi sentire sempre a casa, anche quando lontana. Ai miei nonni, per il loro affetto incondizionato, percepito in una dimensione che trascende lo spazio ed il tempo. A mia zia Gilda, il mio immortale modello che risplende intensamente ogni giorno di più.

Ai miei amici, quelli nuovi e quelli di sempre, quelli persi e poi ritrovati, un ringraziamento infinito per aver contrastato la pazzia delle scadenze e i silenzi delle difficoltà con la quiete e il rumore della compagnia. Sono fortunata ad avervi.

In ultimo, il ringraziamento al compagno di viaggio le cui cure fanno sembrare più corto il cammino, più leggera la scalata. Nanni, non esistono parole adatte a descrivere la tua infinita pazienza, l’instancabile dedizione e l’incredibile abilità con le quali mi accompagni, rasserenando il cielo in tempesta e illuminando la notte più buia. A te devo la mia serenità.

Chapter 1: Introduction

In the latest years the relevance of Unmanned Aerial Vehicles (UAVs), commonly referred to as drones, in many aspects of the modern life has increased exponentially. Limitless commercial applications can leverage on the high flexibility, scalability and rapidity in deployment of these novel platforms which can support or completely substitute human operators, overcoming their limitations during missions involving different levels of risk. The variety of examples dealing with their exploitation is wide and it ranges from UAV-assisted disaster management [1] to monitoring and inspection [2], [3] and package delivery [4]. The advantages brought by UAVs are reflected in their forecasted fleet size which, in the specific case of commercial applications, is expected to reach numbers as high as 400 000 in Europe by 2050 [5] and 175 000 in the United States by 2035 [6]. Many of these platforms will likely operate in low altitude, generally defined as being below 150 meters, in and around urban areas. In these regards, Urban Air Mobility (UAM), which is a subset of Advanced Air Mobility (AAM), foreseeing UAV-based air transportation solutions, plays a major role.

The innovative concepts of operations and the expected high density of UAVs traffic volumes have raised issues concerning their safety and security, yielding to pressing research questions on the enhancement of the systems which define these platforms. Among these, Detect And Avoid (DAA) technologies, providing the capability to identify and avoid collision threats, and navigation solutions, enabling autonomous localization, path planning and following, appear to be significant areas of focus being both greatly needed to achieve the level of autonomy and safety required for UAVs. Nonetheless, the low altitude flight profiles, the dimensions of the vehicles and the unreliability of Global Navigation Satellite System (GNSS) positioning information in urban areas pose significant challenges in the development of both. These challenges are addressed in this thesis which aims at developing sensing approaches for DAA and UAM/AAM surveillance exploiting non-cooperative strategies, which compensate for the unreliable GNSS information while generating a sensing solution suitable for the detection of all types of intruders,

either transponder-equipped or not, and multi-UAV cooperation strategies for navigation performance improvements.

In this chapter, an introduction to each of these research threads is provided with overviews highlighting the motivations of the study. Specifically, sections 1.1, 0 and 1.3 present the DAA, UAM/AAM surveillance and multi-UAV cooperation frameworks, respectively, while section 1.4 provides an outline of the manuscript, instead.

1.1 DETECT AND AVOID

Sensing strategies enabling DAA represented a widely investigated topic in the UAVs community in the last 15 years [7]-[12], becoming one of the main roadblocks to the integration of UAVs withing controlled and uncontrolled airspace. Many efforts in past research works have been concentrated on medium and large size UAVs flying in the traditional Air Traffic Management (ATM) system with other manned and unmanned aircraft [13], [14]. Therefore, low altitude DAA within the UAV Traffic Management (UTM)/U-Space ecosystem represents a relatively recent field of activity. In fact, UTM/U-Space concepts and rules represent themselves an open area of development, with many efforts relevant to the definition of the airspace structure and of the infrastructure to support safe autonomous flight operations [15], and the consequent needs in terms of Communication, Navigation and Surveillance (CNS) [16]. While near term objectives involve enabling Beyond Visual Line Of Sight (BVLOS) operations for small UAVs (sUAVs), UAM vehicles have appeared as new entrants in this scenario, and their mission profiles potentially involve both traditional ATM and low-altitude airspace.

In this context, the relation among cooperative DAA, non-cooperative DAA and infrastructure-based separation management is still an open area of investigation. This lack of definition also applies to sensing requirements, safety levels, flight rules, and their links. However, a multi-layered conflict management architecture (conceptually similar to what is applied in the ATM context) is widely considered as the concept to be implemented [17]. This vision foresees the integration of strategic path planning and deconfliction, tactical conflict management, and DAA, as different safety measures applicable in different ranges of time to collision. Non-cooperative collision avoidance is the last level of safety, typically associated with a time to

collision of the order of a few tens of seconds, at most. Nevertheless, when flights over urban areas are considered, non-cooperative solutions might be the only available tool to perform safe operations under GNSS-denied or GNSS-challenged conditions.

When non-cooperative sensing architectures are considered, the cluttered low-altitude environments (characterized by the presence of both fixed and moving obstacles), the constrained budgets of flight platforms, and the low detectability of small aircraft flying relatively close to the ground, represent the main issues to be addressed. These sensing challenges have been widely highlighted in the recent literature with strong focus on the exploitation of visual cameras and RADARs for detection and tracking of sUAVs. The former appear as one of the most valid sensor alternatives in terms of Size Weight and Power (SWaP) and cost, however, their operations are strongly influenced by the availability of clear-sky and good visibility conditions which can affect the achieved declaration range. Moreover, the lack of distance measurements is an additional drawback in their exploitation. From this point of view, RADARs represent a weather and illumination independent solution capable of accurate distance (and velocity, if Doppler RADARs are used) measurements, though showing degraded performance when operating in low altitude, highly-cluttered scenarios. To overcome the limitations of purely visual and RADAR-based sensing solutions, in terms of trade-offs between their dependence on environmental conditions and type of information retrieved, fusion strategies can be exploited thus providing accurate range (and range rate) estimates which are typical of RADARs, coupled with accurate angular measurement visual cameras retrieve, instead.

In this thesis different sensor fusion strategies tailored for non-cooperative architectures comprising RADARs and visual cameras are proposed. First, the advantages of a multi-sensor RADAR/visual architecture for DAA, supporting an adaptive conflict detection logic, are discussed using numerical analyses. In the latter, visual cameras are exploited to cover the lateral areas of the Field Of View (FOV) of the own-ship to address the requirement of lower declaration ranges. The feasibility of retrieving range estimates using visual data only is then investigated on an experimental basis, proving that the knowledge of the class of intruders can be

used to reliably identify their distance from the own-ship up to few hundreds of meters and yielding to improved conflict detection performance. The latter needs to be supported by reliable and accurate tracking strategies which, in this thesis, exploit both visual and RADAR data collected during experimental ground-to-air flight tests with sUAVs. The benefits of exploiting both sensors within a data fusion solution are remarked with respect to their standalone implementations by using various fusion approaches which achieve meter-level accuracy on range and sub-degree accuracy on angular estimates using Extended Kalman Filters (EKF) and a Carrier Phase Differential GNSS (CDGNSS) benchmark. The developed fusion strategies range from centralized schemes, exploiting the RADAR as the main sensor for the generation of firm tracks, to de-centralized schemes, where Track-to-Track fusion strategies are used. In the former case, pre-processing of RADAR data, needed to remove clutter, is also proven to be feasible using visual cues, yielding to a Fuse-Before-Track approach where fusion takes place both at detection and tracking levels.

1.2 UAM/AAM SURVEILLANCE

AAM and UAM are concepts of operation for air transportation of people and goods based on novel aircraft models including both UAVs and electrical-Vertical Take Off and Landing (e-VTOL) platforms. These concepts are bound to radically transform the air transportation market by promoting a shift from scheduled operations to on-demand ones [18] where multiple vehicles operate under the control of fewer operators [19]. In this environment, platforms such as air taxis [20], commuting people around urban areas, will operate alongside platforms performing package deliveries, either for private parties or for medical first responders [21], within a highly dense air traffic scenario. Relevant research studies are focused on the investigation of both social/economical aspects potentially affecting the air transportation market [22] as well as on regulatory [23] and technological aspects. In this latter perspective, technological innovations in several systems, including both onboard avionics and air traffic control/management and surveillance systems, are needed to achieve the technological maturity level, also referred to as UAM Maturity Level (UML) [24], required to support the forecasted highly dynamic and highly dense volumes of operations.

A key enabler for the UAM/AAM vision is the design of a detection and tracking solution to be used in a surveillance architecture. In this field, the efficacy of cooperative traffic monitoring systems relying on the broadcast of information from the surrounding traffic, via Automatic Dependent Surveillance-Broadcast (ADS-B) transponders for instance, can be weakened by the absence or unreliability of GNSS information typical of urban areas. Although secondary information sources for ADS-B can be implemented to tackle its dependence on GNSS [25], non-cooperative solutions need to be considered to also strengthen the surveillance architecture towards malicious intrusions within the flight volumes. From this point of view, the DAA concept intercepts the UAM/AAM surveillance one being, in fact, foreseen as a constitutive crucial onboard system for the mitigation of risks associated to in-flight collisions with fixed and moving obstacles [26]. Indeed, the concept of distributed sensing, also including airborne DAA, is being investigated to provide improved air monitoring performance and enable the level of autonomy and reliability required for AAM. In addition to the enhanced surveillance coverage, a distributed network of sensors used to monitor specific air corridors and take-off and landing sights, i.e., vertiports, can also bring advantages in terms of higher precision and accuracy achieved by exploiting the different viewing angles and spatial disposition of the sensors in the network [27]. It appears to be clear that these benefits can only be unlocked by implementing fusion strategies which account for the different components of the sensing network.

Following this research, this thesis discusses experimental assessment of visual and RADAR-based sensing strategies for a network of distributed ground-based sensors and proposes a novel fusion solution to improve track coverage using the RADARs comprised within the network. The strategies are tested on experimental data collected during joint activities with the NASA Langley Research Center, where data were gathered with three distributed sensing nodes observing the flight of up to five sUAVs. First analyses are focused on the benchmarking of different visual-based and RADAR-based detection and tracking strategies, highlighting the feasibility of keeping tracks of multiple objects, either drones or birds, with customized EKF trackers. However, track dropouts are verified for the single sensors' implementations, especially in the RADAR case where the cluttered environment challenges the retrieval of valid measurements. To reduce track

dropouts, fusion strategies can be designed to leverage on the availability of measurements from sensors located in different positions. In these regards, this thesis proposes an innovative RADAR-based helper-leader fusion strategy where a main RADAR (leader) exploits the measurements of the other (helper) to increase the lifespan of its firm tracks, yielding to higher track coverage percentages with respect to the single RADAR implementation. The strategy reproduces a scheme where data between devices located along the monitored flight area need to be exchanged and thus the translation of measurements and inflation of their covariances is required for their injection within the EKF of the leader's tracker. As an additional contribution, an effective RADAR interference mitigation method is also provided within the thesis. The latter gains major relevance when multiple radars operate with overlapping FOVs and is thus used as a data pre-processing step to filter out unwanted, interference-affected measurements before tracking takes place.

1.3 COOPERATION BETWEEN UAVS

The utilization of teams of multiple UAVs using cooperative behaviours is a powerful tool to complete tasks with enhanced efficiency. The possible applications of multi-UAV cooperation are numerous and range from their physical coupling for load transportation [28], [29], to the exchange of information for disaster management, such as wildfires image collection [30], or post-disaster monitoring [31]. Nevertheless, cooperation can play a major role in enabling navigation of single UAVs operating in environments where their autonomous flight might be otherwise hindered. If the focus is set on urban areas, where UAVs will heavily be deployed in the future, different challenges arise. Firstly, the accuracy of GNSS data, on which the absolute localization of own-ships relies, can be strongly weakened or totally absent in scenarios with urban canyons where the presence of spoofing and jamming signals is an additional issue to be considered. Furthermore, the presence of large metallic structures and electromagnetic fields can negatively affect the performance of the onboard Inertial Measurement Unit (IMU) whose magnetometers' reading can be distorted, thus yielding to coarse heading angle estimates.

The work carried out in the context of multi-UAV cooperation is focused on this latter aspect and provides a novel calibration strategy for magnetometers by estimating onboard and external magnetic disturbances and improving the accuracy

of the heading estimate. The strategy exploits both CDGNSS and visual information and is tested offline on experimental data collected with onboard sensors during the flight of two sUAVs. During the flights a chief UAV, for which magnetometers' calibration needs to be performed, is maneuvered as to rotate around a deputy UAV, which is used as an aiding agent for the calibration procedure.

1.4 THESIS OUTLINE

The presented thesis aims at investigating non-cooperative sensing strategies for low altitude sUAVs which can be used to design both DAA and UAM/AAM surveillance technologies. Furthermore, it also explores the feasibility of using multi-UAV cooperation to improve magnetic heading angle estimates. In this latter case, sensing is also required to enable the computation of onboard and external magnetic disturbances. The structure of the manuscript is as follows.

Chapter 2 provides a comprehensive literature review of the stat-of-the art strategies for detection and tracking of UAVs with non-cooperative sensors. In this case, an analysis is provided for all type of sensors, both passive and active, while a majorly detailed discussion for RADARs and visual cameras, which have been used during the research activities, is presented. The review remarks the limitations of the application of single sensors and thus also provides an overview of the fusion strategies utilized by the research community over the latest years.

Analyses focused on the performance of a non-cooperative DAA architecture are presented in Chapter 3. Here, the idea of an adaptive sensing strategy used to design an onboard multi-sensor DAA architecture is discussed and numerical results on its performance are presented. Then, the focus is shifted to purely visual solutions where the feasibility of estimating range from the appearance of targets on frames experimentally collected during sUAVs flights is assessed and its impact on conflict detection is investigated.

The work carried out on RADAR and visual sensing strategies for DAA relies heavily on experimental data collected in relevant scenarios, which can be used to more properly assess the performance in real-world conditions. Therefore, before presenting the developed solutions, details on the experimental tests performed are provided in Chapter 4.

Chapter 5 presents the standalone visual-based and RADAR-based detection and tracking strategies developed and tailored for sUAVs with low altitude flight profiles. Both the proposed tracking strategy, which exploits Kalman filtering approaches, and the detection strategy with different detectors, in the case of visual cameras, and pre-processing step applied on RADAR data are discussed. In the latter case, the effects of noise, mostly related to ground clutter is remarked. Then, fusion solutions based on RADAR/visual information are discussed in Chapter 6 where three main fusion strategies are detailed. These differ in terms of computational complexity and data exchange requirements. The results presented highlight the benefits achievable when information is fused.

In Chapter 7 the focus is set on distributed sensing for UAM/AAM surveillance. In this case a brief introduction to the experimental activities carried out at the NASA Langley Research Center is provided before discussing the proposed strategies and the results thereof. As a first step, benchmarking of different RADAR-only and visual-only sensing strategies is discussed. Then an innovative fusion solution merging data of the RADARs within the sensing network is proposed as a mean to effectively counteract the lack of measurements of one RADAR by exploiting the others, thus improving the track coverage performance.

Chapter 8 proposes the multi-UAV cooperative strategy for magnetometers calibration which simultaneously computes the magnetic disturbances, from the onboard components and the rotating propellers of a multirotor, and the magnetic declination. The results are evaluated by exploiting a pointing accuracy analysis where the heading angle achieved with the calibration technique is compared to the "un-calibrated" one as well as to the estimate from the onboard navigation filter. Tests carried out on experimental data during the flight of two sUAVs show improvements in pointing accuracy using both ground-based and airborne control points.

Finally, Chapter 9 draws the conclusions of the thesis.

Chapter 2: Sensing and Data Fusion: Application to UAV detection and tracking

The safety of UAV missions is an issue with multiple facets which requires thorough investigations and innovations in all the technological aspects defining these novel platforms. From the surveillance and DAA perspective, safety can be achieved through the development of sensing strategies to detect and track objects (fixed and moving) within the environment surrounding the platforms. Detection and tracking can be performed with different sensing modalities which are broadly categorized as cooperative or non-cooperative. While the first show higher localization accuracy, their reliance on GNSS information and on the need for both interrogating (onboard own-ships) and responding (onboard intruders) transponders represent limits which can potentially hinder the safe navigation of UAVs. Therefore, to keep up with the growth of the UAVs' market and enable their final integration in uncontrolled and controlled airspace, where their co-existence with manned aircraft will need to be addressed, DAA and surveillance architectures should be designed to also rely on non-cooperative technologies. The latter can be divided in two categories, passive and active, showing distinctive features which are briefly detailed within this section and summarized in Table 2.1.

Passive sensors rely on external energy sources to "illuminate" the objects to be detected. Hence, Electro-Optical (EO) technologies, such as visual and infrared (IR) cameras, or acoustic devices, such as microphones, fall within this category and exhibit low SWaP characteristics which makes them good candidates for both ground and airborne applications. Visual and IR cameras can both provide accurate angular information which, however, is not coupled with a direct distance measurement. Specifically, IR cameras are less affected by the illumination/weather conditions than their visual counterpart as they rely on heat emissions. However, the larger wavelengths of the latter, leads to larger sensing elements and lower resolutions. Acoustic sensors, on the other hand, detect objects based on their sound signatures,

thus being in most cases too sensitive to the environmental sounds for a reliable use in DAA.

Table 2.1 Major characteristics of sensors used for UAV detection and tracking.

	Sensor	Pros	Cons
PASSIVE	Visual	• Low cost • Low SWaP • High angular accuracy	• Limited by illumination and weather conditions • No direct distance measurement (unless multiple cameras are used)
	Thermal/Infrared	• Low cost • Low SWaP • Independent from illumination/weather	• Lower resolution with respect to visual cameras • No direct distance measurement (unless multiple cameras are used)
	Acoustic	• Low cost • Low SWaP	• Limited by environmental sounds • No distance measurement • No bearing measurement (unless multiple devices are used)
ACTIVE	LiDAR	• Direct range measurement • High pointing and range accuracy	• High cost • Low detection ranges • High computational cost for data processing
	RADAR	• Direct range/range rate measurement • High range accuracy • Weather and illumination independent	• High cost • High power consumption • Interference phenomena can degrade the performance

Active sensors, e.g. Radio Detection And Ranging (RADAR) and Light Detection And Ranging (LiDAR), rely on their own source of energy and exploit its backscattering on the surface of detected objects to retrieve information about their distance. The biggest advantage in their exploitation is therefore represented by the possibility of achieving both range and angular information, as well as radial velocity or range rate in the case of Doppler RADARs, under all-weather-all-time conditions. The typically lower detection ranges of LiDARs, if compared to the novel RADAR technologies, and the computationally expensive data processing steps which need to be applied to their raw measurements (dense 3D point clouds) are the main reasons behind a lower interest of their exploitation for DAA and surveillance applications.

The limits of standalone passive or active sensors implementations can be largely overcome by designing data fusion strategies which can benefit from a wide

spectrum of heterogeneous, sometimes complementary, measurements and achieve higher performance both in terms of solution accuracy and coverage of the area under surveillance.

In the following subsections, a comprehensive review of past and recent literature is provided to highlight the efforts of the scientific community towards the exploitation of non-cooperative sensors for the detection and tracking of UAVs. Specifically, both passive and active technologies are considered and the related references are detailed in subsection 2.1 and 2.2, respectively. Finally, examples of data fusion research paths are discussed in subsection 2.3.

2.1 DETECTION AND TRACKING OF UAVS WITH PASSIVE SENSORS

2.1.1 Acoustic Sensors

Recent literature examples dealing with acoustic detection mostly implement Machine Learning (ML) strategies to distinguish UAVs based on the distinct acoustic signature of their fast-rotating propellers. In reference [32], for instance, a concurrent Neural Network approach is proposed to improve the detection performance with respect to a single network solution. Thus, multiple networks (independently tested) are used during the detection phase and the final detection is selected from the network with the strongest response. This strategy achieves an average accuracy of 96% when detecting multirotor UAVs with varying dimensions, reaching detection ranges of about 380 meters and 500 meters for platforms with diameter below 1 meter and above 1.5 meters, respectively. Reference [33] addresses the issue of separating UAVs sound signals from interference and noise which arise in an outdoor environment. In this case, the blind source separation theory is exploited to estimate the number of signal sources before ML-based detection is applied to strengthen the recognition performance for three different types of small multirotor UAVs.

These studies show promising results in the field of acoustic detection of UAVs, however, they lack discussions the use of the acoustic measurements during tracking or their application for DAA/surveillance tasks. In these regards, references [34]-[36] provide more complete analyses. In reference [34], air-to-air experimental tests with small, fixed-wing UAVs flying on circular patterns, thus emulating mid-air

collision courses, are described. In this case, a sensing aircraft equipped with four microphones is used to detect a propeller-driven target UAV achieving a detection distance of about 678 meters by extracting the harmonic components of the UAV-generated acoustic signal. Reference [35] utilizes a network of 24 different microphones with which the direction of arrival of signals, thus their bearing angle, is estimated and used within a Kalman filter to track intruders. A similar approach has been more recently proposed in [36], where a set of four ground-based stations, equipped with five microphones each, is used to detect and track low flying aircraft. The robustness and reliability of the proposed system is proved over a timespan of ten months during which continuous acquisitions were carried out. However, acoustic detection and tracking is only demonstrated for targets such as helicopter and small General Aviation (GA) aircraft. An example of the latter is reported in Figure 2.1 where snapshots of the tracked GA aircraft, as collected by a ground-based camera steered accordingly to the tracking estimates, are also provided.

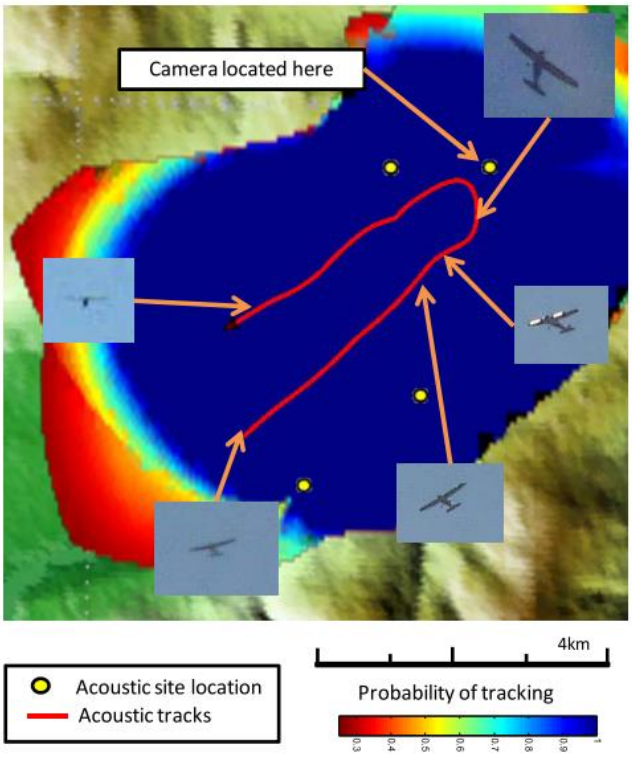

Figure 2.1 Example of tracking of a small aircraft using acoustic measurements [36].

2.1.2 Visual and Infrared Cameras

Due to the poor heat emission of UAVs, there are scarce literature examples which deal with the use of IR-based detection solutions which appear to be more

suitable for UAV-based airborne applications including fire detection [37], ground inspection [38] and surveillance [39]. Few examples dealing with the specific case of UAVs IR detection can be found in references [40], [41]. Specifically, the experimental assessment carried out in [40] highlights the unexpected lower heat footprint of the propellers of small multirotor UAVs if compared to their batteries while reference [41] details a CNN-based detection methodology for UAVs captured within the IR spectrum.

As far as visual cameras are concerned, though their operations are strongly related to the external environment, e.g., weather and illumination conditions, the significant advancements in the computer vision field, fueled by the increasing availability of relevant datasets [42]-[44], their low SWaP characteristics and ease of installation have resulted in a skyrocketing trend of their exploitation. In this context most works focus on spatial-temporal filters or appearance-based ML approaches while fewer literature examples deal with the exploitation of event-based visual cameras, with which motion in the scene can be inferred by means of pixel brightness changes [45]. In reference [46], the CASIA I system by Iris Automation [47] is used onboard a small, fixed-wing UAV to detect the presence of a General Aviation (GA) manned aircraft intruder during flights which include different encounter scenarios and BVLOS operations. The exploited ML-based detection system achieves an average detection range of about 700 meters, while proving its ability in autonomously declaring a collision threat and performing avoidance maneuvers accordingly. In [48], [49], a detection strategy based on a Close-Minus-Open morphological filtering stage, to detect both positively and negatively contrasting objects with respect to the background, is exploited and coupled with temporal filtering based on two different strategies, either hidden Markov model or Viterbi-based filtering. The two proposed solution, tested on data collected during real encounter-like flights of two small fixed-wing UAVs, show comparable performance in terms of detection range while also proving the importance of image compensation and stabilization to reduce jitter within images. This latter point was later explored in [50], where the authors prove increased detection ranges when the image stabilization is achieved using approaches based on inertial sensors rather than on the camera images. A detailed experimental analysis of a visual detection and tracking strategy for DAA can be found in [51] in which a detection pipeline

consisting of on-image horizon line estimation, morphological filters and frame differencing is proposed. The horizon estimation step is exploited to strengthen the strategy towards background changes; thus the detection step is automatically tuned depending on the region of the image (sky or terrain) where the object is first detected. The visual measurements are then passed over to an Extended Kalman Filter (EKF) for tracking, achieving declaration ranges, at which valid tracks are first initiated, settled above the kilometer level in all cases. Interesting experimental highlights are also discussed, showing the degradation of the tracking performance in terms of false track generation, depending on the quality of the image. An example is shown on the left in Figure 2.2 where false tracks generated from lens flares are depicted. The effects of high contrast image regions, such as the terrain ones, on the detection performance of a visual pipeline are remarked in [52] where different detection strategies are tested based on feature detectors such as Shi-Tomasi [53], SURF [54] and FAST [55]. In this work, false detections arising from the terrain are mitigated by only applying the detectors on the above-the-horizon (AH) portion of the camera images. In [56] the authors have expanded this research by also implementing a morphological filtering and image differencing techniques for the retrieval of AH visual detections of a fixed wing sUAV and GA manned aircraft imaged by a small multirotor during flight. The discussed results show an improved accuracy in the case of the morphological strategy which, however, is challenged by the presence of small clouds in the camera FOV. Tracking is also performed exploiting an EKF which builds up estimates of the location of detected objects on the image plane. In an air-to-air DAA scenario, where UAVs should be able to detect threats both above and below-the-horizon (BH), the mitigation of the degraded performance of a visual-based pipeline need to be addressed and solved. A possible solution is proposed in [57] where a CNN approach is used to identify aircraft which are then tracked between frames using temporal filtering, thus making it possible to both achieve detection of aircraft which exhibit small apparent motion (typical of collision courses) and reject detection from other ground-based moving objects such as cars.

Although these studies detail interesting insights on the sensing of flying obstacles by means of visual information, they all focus on either fixed-wing UAVs or GA aircraft targets. When small unmanned multirotor are considered, the visual

detection task is particularly challenged by their reduced dimensions, especially in low altitude conditions which can cause lower visibility near the ground. Examples of research works focusing on the detection of such platforms appear to be more recent and can be found in [57]-[60]. References [58], [59] focus on CNN-based solutions exploited to classify UAVs with respect to similarly appearing objects such as birds, thus improving the overall detection performance by reducing false positives. This concept is illustrated on the right in Figure 2.2 where a UAV and a bird show comparable CNN detection confidence score. Specifically, reference [58] proposes an effective combination of moving objects detection, exploiting image differencing for static background subtraction, and classification, exploiting a CNN approach. However, the proposed solution, though reducing false positives from similar targets, shows its flaws in the presence of dynamic background (wind-shaken vegetation for instance), yielding to poorer performance. References [60], [61] solve the detection task by means of image processing strategies which imply morphological and temporal filters [60] as well as image differencing and optical flow [61] demonstrating that sUAVs can be effectively detected with solutions alternative to CNN-based ones, thus not requiring the same intensive training procedure. Still, as in the case of fixed-wing larger UAVs, small multirotor also need to be reliably detected when appearing both in AH and BH within an image. In this case, CNN can be a powerful tool as demonstrated in [62] where two different neural networks are utilized for small quadcopters either in AH or BH portions of the image. The results achieved show that detection in both conditions is feasible though reduced detection ranges are observed in BH.

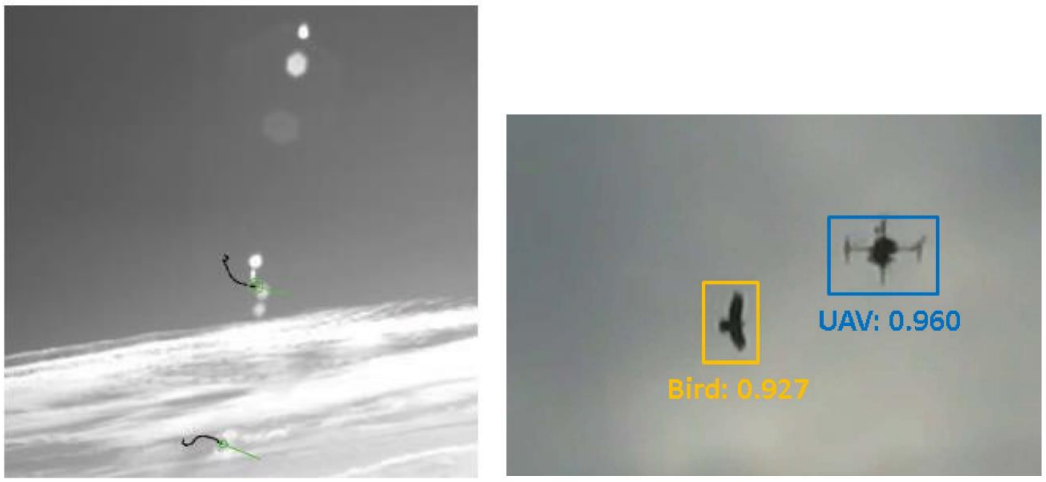

Figure 2.2 Left: False tracks (black) and their prediction over one second (green) generated from lens flares [51]. Right: Example of CNN detection and confidence scores of a multirotor (blue) and bird (yellow) [59].

2.2 DETECTION AND TRACKING OF UAVS WITH ACTIVE SENSORS

2.2.1 LiDARs

The exploitation of LiDAR technology for the detection of UAVs is not widely explored in the available literature. The reasons behind this trend lie in the typically low detection ranges which, couple with the high weight/power budget requirements and the dense 3D point clouds retrieved, makes such devices more suitable for mapping or navigation purposes [62]-[64].

However, in the framework of object detection, the opportunity of retrieving distance measurements provided by 3D LiDARs has attracted the interest of research groups worldwide. An interesting analysis of the characteristics of LiDAR detections when capturing sUAVs during flight is presented in [66]. Here, the authors investigate the dependence of the detection performance on the environmental conditions and reflectivity of the observed UAVs, showing best results in daylight scenarios. In this latter perspective, a demonstration of the point cloud density for two UAVs collected at distances going from 10 meters to 80 meters is depicted in Figure 2.3, thus showing that a white-colored platform (UAV1) is more visible due to its higher reflectivity with respect to a dark-colored one (UAV2). In [67] both static and dynamic (onboard a flying small octocopter) LiDAR acquisitions are analyzed showing that a sUAV can be reliably detected below 15 meters in distance. Still, the appearance of the target in the LiDAR-built 3D map is limited to few 3D points in a highly cluttered environment, with a persistent presence of fixed obstacles

such as trees and buildings. Tracking of a sUAV by means of LiDAR measurements is discussed in [68]. In this case, a voxel-based occupancy map approach is used for the detection of objects in the LiDAR FOV, thus avoiding the computationally and timely expensive sampling/grouping of raw 3D points. Therefore, as a first step clusters of points are generated by grouping points based on their Euclidean distance, then their classification as either background or flying object is performed by analyzing the neighboring voxels. The presented results show that by implementing a multi-target tracking strategy, thus preserving target position estimates during a temporary absence of measurements, recall values can be significantly improved with small losses in position accuracy. The study conducted in [69] proposes a LiDAR obstacle warning and avoidance system as a constitutive element of a DAA architecture. A complete survey of the system architecture, mathematical models and avoidance trajectories generation are provided. Specifically, the performance of the algorithm responsible for the latter are assessed within a simulation environment where a UAV, equipped with the proposed system, is able to detect and avoid fixed obstacles (wires of a power line and buildings). A simulation-based method is also used in [70] where a sUAV is identified as the target to be detected and avoided during encounters, at varying speeds and distances, in UAM corridors. In this case, experimental tests are conducted to retrieve the scanning patter of the device whose behavior is then simulated.

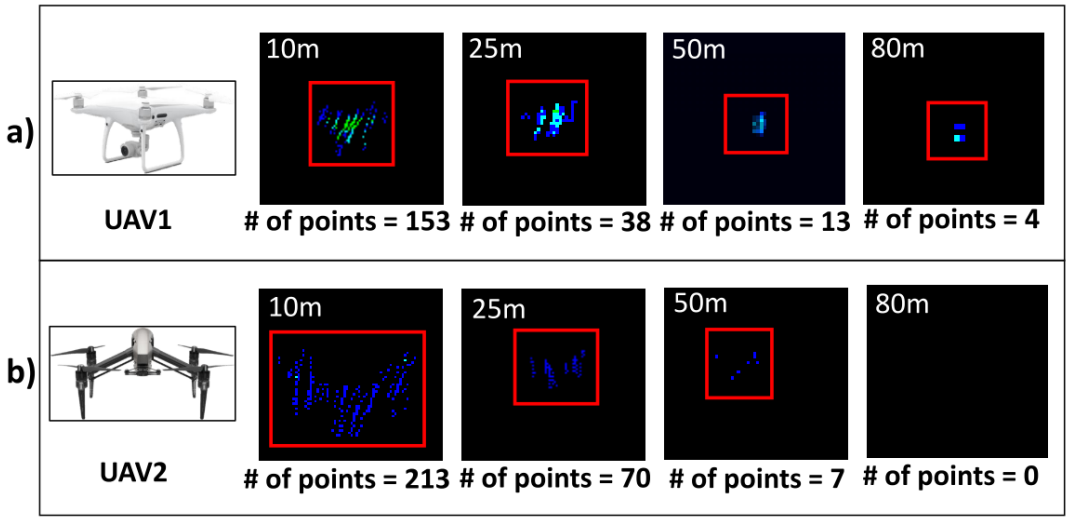

Figure 2.3 LiDAR point clouds for two different UAVs at increasing distances (reported in left corners of each image) [66].

2.2.2 RADARs

RADARs are a well-established technology for the surveillance of the airspace, still their application to the UAV use case can be challenged by low values of Singal to Noise Ratio (SNR), mostly caused by the low reflectivity of sUAVs. Such quantity is expressed in terms of the RADAR Cross Section (RCS) which depends on several factors including the constitutive material of UAV components, their shape, dimensions and the angle at which the signal is intercepted (and reflected). The effects of different materials on the visibility of objects in the RADAR domain is explored in [71], where rotor blades made of plastic, carbon fiber and metallic materials are compared at different frequencies, showing reduced reflections, almost meeting the RADAR measurement capability, for the first case. This concept is also remarked in [72], where an increase in the mean RCS of about 7 dB for carbon fiber UAVs with respect to plastic ones is proved while also remarking the greater RCS signature of electric components, such as the Li-Po batteries. To tackle the low RCS values, the detection of UAVs can be enhanced by means of structural modification of their cases by adding corner reflectors, for instance, [73] which can also enable the calibration of RADARs exploiting flying UAVs [74].

Apart from the low RCS of some UAV types, which can hinder RADAR detections, further challenges arise when such active devices are used, especially when high transmitted powers, thus large detection ranges, are involved. During the acquisition operations, RADARs are affected by the interception of reflections arising from static objects, i.e., clutter, which can be considered as nuisances reducing the visibility of sUAVs [75]. The effect of clutter can be typically mitigated by adopting filtering strategies based on the Doppler measurements (if available) [76] or by reducing the FOV to be covered to avoid reflections from ground, as discussed in [77] for the flight of a fixed-wing UAV equipped with two RADARs, shown in Figure 2.4. When Doppler-based filtering is used, information on objects flying with very low speed or during hovering phases can be easily lost. To avoid this, some research works exploit background removal pre-processing steps either by means of point-by-point subtraction of RADAR data and principal point analysis, easing the extraction of slow-moving targets such as pedestrians in an urban environment [78], or a combination of Gaussian mixture models [79]. In the latter reference, track-before-detect strategies are then applied to detect UAVs flying at a

distance of 200 meters. Nevertheless, in addition to clutter from fixed scatterers, the presence of multiple moving objects, especially when close in space, can also cause the generation of false tracks when used as input during the tracking phase. This is shown in [80], where tracks belonging to a UAV flying at a maximum distance from a fixed RADAR of about 400 meters are merged to tracks of cars moving in the surroundings. As a solution, the authors propose the application of the Hough transform to enhance detection and tracking of UAVs.

The advancement in RADAR technology, especially in the field of FMCW devices, has promoted improvement in their performance for small objects sensing as well as reduction in their dimensions, thus leading to the design of devices which are evermore suitable for airborne applications. This has also been pushed by the recent introduction of low-cost Commercial Off The Shelf (COTS) automotive RADARs. In [81] a demonstration of the greater performance of a FMCW RADAR with respect to a pulsed one is provided for the case of sUAV detections which occurs at greater distances with the first technology. Instead, references [82], [83] compare the performance of similar FMCW RADARs during the flight of a multirotor and fixed-wing UAV, respectively, achieving range detection capability beyond one kilometer in both cases. Specifically, in [82] the authors discuss the good accordance between RADAR tracks and a GNSS benchmark while also proving the capability of the RADAR to sense other moving objects such as birds. A similar study is conducted in [83] where, however, the lower operating frequency band and maximum distance reached by the UAV promote a detection range below 50 meters. A proof-of-concept of a RADAR-based DAA architecture is provided in [84] where experimental tests with multiple small multirotor, with attached corner reflectors to improve their detectability, are observed by a ground-based RADAR achieving detection rages about 250 meters. The exploitation of an automotive RADAR is explored in [85] where different automotive RADARs are used to capture data of a small UAV up to 40 meters. Additional analyses are also provided by installing an onboard RADAR on a multirotor and confirming the accuracy of its tracks by comparison with an available GNSS ground truth.

The research works analyzed so far are greatly contributing to the development of sensing strategies relying on RADAR data which, however, can be difficult to

interpret when classification of detected objects needs to be performed. In these regards, the use of Doppler RADARs, measuring Doppler-shifts, thus radial velocities, can be an advantageous solution. Research works have, in fact, shown the feasibility of distinctly identifying UAVs RADAR signatures by exploiting their micro-Doppler effect, which arises from fast rotating parts such as propellers. Examples can be found in [85]-[87]. Specifically, the difference between UAV- and bird-driven signatures is analyzed in [86]. CNN-based methods can also be used to classify UAVs based on their micro-Doppler behavior. In this context, reference [87] shows promising results, though highlighting the challenges which arise when false alarms, thus other objects, are present in the FOV. Instead, reference [88] provides a novel classification solution which reaches accuracy levels above 90% both in indoor and outdoor environments.

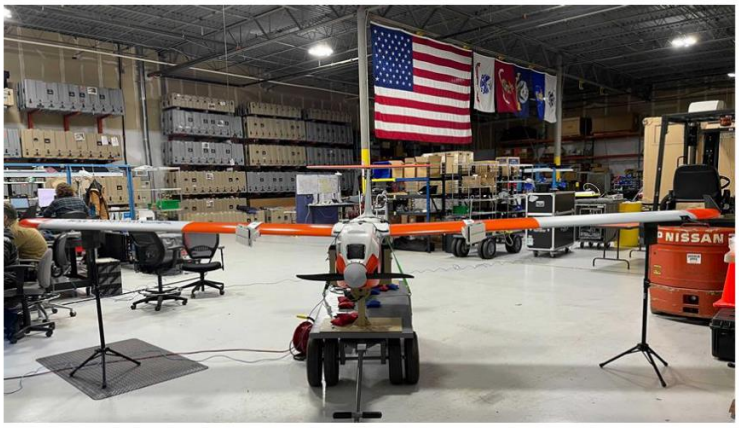

Figure 2.4 RADARs mounted on the wings of a fixed-wing UAV [77].

2.3 DETECTION AND TRACKING OF UAVS WITH MULTIPLE SENSORS

The constraints which arise from the use of sensors in standalone configurations can be overcome by applying fusion strategies designed to leverage on the availability of information, typically complementary in nature, from multiple sources. The related research literature is not as wide as that which focuses on the study of the standalone architectures.

Some of the available examples deal with the fusion of information retrieved both by cooperative and non-cooperative sensors. The idea behind such heterogeneous architecture lies in the fact that UAVs can be more accurately detected if equipped with transponders which, however, might be absent or

weakened by corruption (or interruption) in the reception of GNSS signals. Following this logic, references [89] and [90] propose a multi-sensor DAA architecture which is based on ADS-B data but exploits different non-cooperative sources as well. In [89], such sensors are Radio Frequency (RF) and RADAR ones whose measurements are fused with ADS-B by means of conditional schemes. The latter decide upon which measurement to be kept based on their distance in a cartesian reference frame. As a generical rule, RADAR data is always neglected when ADS-B information is available. In reference [90], a concept coupling the ADS-B information with a LiDAR and visual/thermal cameras is proposed. While the LiDAR can be exploited to measure the distance of intruders, the IR camera is used to strengthen the architecture in bad weather and low illumination conditions. Tests carried out in simulated environments show that the designed architecture would be able to support the maintenance of a safe separation distance between UAVs starting from ranges of 500 meters.

As far as fully non-cooperative architectures are concerned, a wide variety of different multi-sensor strategies, encompassing all previously mentioned sensors, have been proposed in past and recent works. In [91] visual and infrared cameras, whose data is pre-processed by means of ML approaches, are used as primary sensors while audio data is used to detect the proximity of multirotor or helicopter based on their distinctive sound and ADS-B data is used to keep track of all aircraft flying in the test region. The performance achieved in both visual and IR spectrum prove to be comparable while advantages of fusing the output of each sensor are demonstrated in terms of increased percentage of correct drone classifications if compared to the standalone cameras cases. In [92] the authors have also expanded their research by including a low-range RADAR sensor which proves detection capability for a sUAV up to 24 meters in range. Acoustic and visual data are also used in [93] where CNN approaches are exploited to identify the presence of sUAVs during flight, proving higher accuracy when fusion of data is considered. Fusion can also be achieved on sensors of the same type to increase the accuracy of the final estimate or improve the coverage over a certain area. Such concept is proposed in [94], for instance, where a distributed network of RADARs is used to track small UAVs, within a simulation environment, during unreliable, e.g., affected by spoofing, GNSS navigation. Indeed, multiple visual cameras can also be used within

a network as discussed in [95] where a visual detection and tracking task, based on frame differencing and blob feature detection, is exploited on four single cameras distributed around a flight field and imaging a small UAV during flight.

Focusing on the fusion of visual and RADAR data, tracking-level fusion of raw measurements from ground-based co-located visual camera and RADAR are described in [96]. Here, an adaptive strategy is exploited to input the measurement, either visual-based, RADAR-based or both, within an EKF tracker pipeline depending on their availability. The results achieved remark the noisier nature of RADAR data and the higher tack coverage percentage which are achieved when both sensors are used. The implemented tracker is also used in the simulation scenario discussed in [97] where the flight of eVTOLs over the San Francisco Bay are considered, thus emulating a UAM/AAM traffic scenario. The sensors considered are a set of cameras and RADARs which are located along the flight path of the vehicle, with RADARs being concentrated in the area where take-off and landing occurs. In this case, the exploitation of multiple cameras can also serve as an expedient to estimate the distance of detected objects by means of triangulation. Results, shown in Figure 2.5, have been achieved both in good and low visibility, thus reduced camera detection ranges, conditions and highlight the need for at least three cameras to achieve good accuracies. Finally, fusion of RADAR and visual data is also detailed in [98]. In this case, fusion starts at the detection level by projecting RADAR data on images collected by a camera, tracking is then performed using a Kalman filter to estimate the motion of the detected UAVs on the image plane. During this phase, a fused measurement, evaluated as a weighted average between the visual and the projected RADAR data, is exploited.

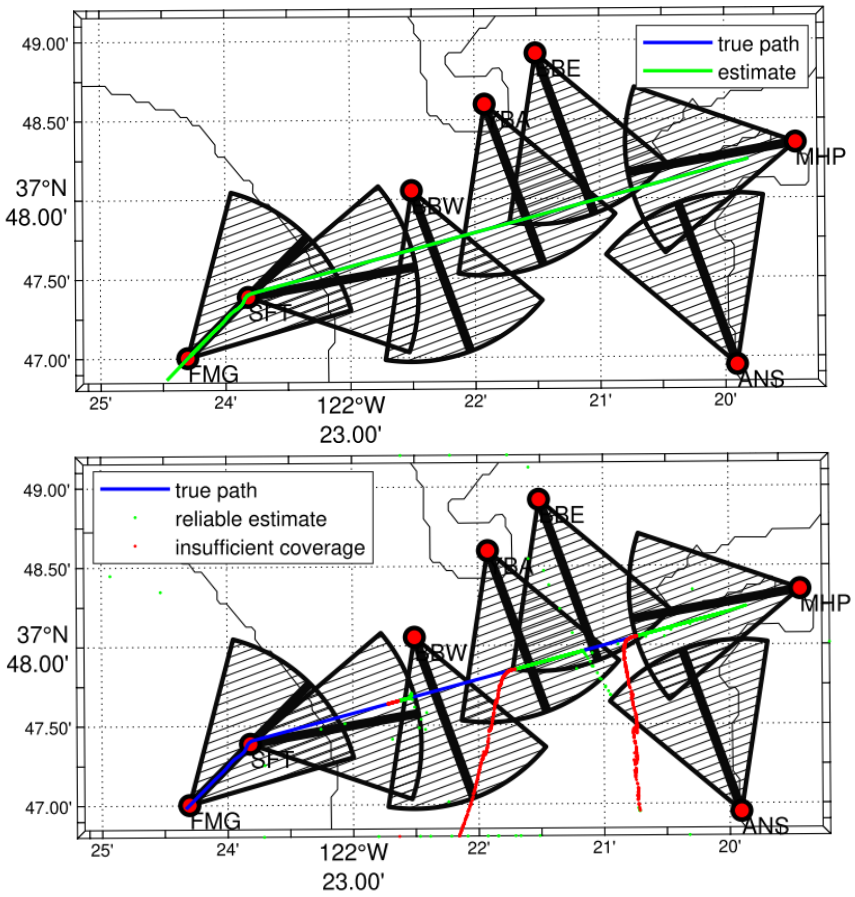

Figure 2.5 Top: true (blue) and estimated (green) trajectory of eVTOL in simulation. Bottom: track divergence (red) caused by low visibility conditions during simulation. Red dots indicate cameras location, RADARs locations are in FMG and MHP [97].

Chapter 3: Adaptive Conflict Detection Strategy

In the framework of non-cooperative DAA solutions, the analysis of missed and false conflict detection probabilities plays a crucial role in the assessment of the performance of the deployed sensing architecture which can be designed to involve multiple sensors, either similar or dissimilar. Given the significant challenges faced by such architectures for low-altitude-flying sUAVs, a promising idea is to tailor sensing resources and approaches towards near collision geometries and given time to collision requirements, thus trying to reach reasonable trade-offs between missed detections and false alarms. In fact, it is clear that conflict conditions change as a function of the obstacle position in the field of regard. In particular, the angle between the line of sight (LOS) to the obstacle and the current own-ship velocity vector plays the major role, with lateral conflicts being characterized by less challenging range requirements. In most studies on non-cooperative sensing, worst case geometries (i.e., near frontal encounters) are considered to define and tune detection and tracking architectures and algorithms, and to verify the possibility to fulfil application requirements. This approach naturally drives towards maximizing the detection range in the whole Field Of Regard (FOR). An alternative approach consists in focusing on time to closest point of approach as the key driver for sensing system design and tuning. The idea of targeting specific values of such time naturally drives towards space/time adaptive sensing concepts.

This chapter explores the feasibility of designing adaptive sensing strategies to improve the performance during conflict detection processes. Two main contributions are tackled and summarized below.

- The idea of space/time adaptive sensing strategies is introduced based on the concept that obstacle detection and tracking, and conflict detection, should account for the variation of closure rates within the field of regard. This concept can support the design and optimization of multi-sensor-based architectures as demonstrated exploiting a numerical simulation

environment where a 2D-horizontal collision scenario between sUAVs is tackled.

- With regards to purely visual architectures, improvements in conflict detection performance are achieved using an adaptive LOS-based criterion which exploits shape-based ranging strategies. The solution is tested on experimental data collected during the flight of two sUAVs and effectively mitigates the over-conservativeness of the visual-based conflict detection criterion.

The chapter is structured as follows. The concept of the adaptive sensing strategy, which exploits information on the variation of closure rates with the speed of the ownship UAV and the angular relative position of the intruder within the FOR is presented in section 3.1. The conflict detection analysis for the proposed multi-sensor architectures is discussed in section 3.2 which also details the statistics for performance evaluation. Section 3.3 presents the shape-based ranging strategy for visual information. Finally, section 3.4 presents the results achieved on adaptive conflict detection within a numerical simulation, while section 3.5 discusses the experimental results on improved visual-based conflict detection.

3.1 ADAPTIVE SENSING STRATEGY CONCEPT

The time to closest point of approach (t_{CPA}) defines the available time for collision avoidance manoeuvring. In the field of sensing architectures design, the idea of targeting specific values of t_{CPA} naturally drives towards space/time adaptive sensing concepts: (1) given the current own-ship speed and a priori information about the (maximum) speed of non-cooperative traffic, it is possible to consider variable sensing strategies within the FOR; (2) the approaches change with time as the own-ship velocity and the information about possible non-cooperative traffic change.

For the sake of concreteness, let us assume an aircraft with vertical flight capabilities (e.g., multirotor UAV), and let us consider speed orders of magnitude that are typical of sUAVs. For simplicity, let us assume horizontal geometries whose graphic representation is illustrated in Figure 3.1 where a collision scenario between an ownship (UAV) and intruder (INT) is depicted.

When the UAV is hovering, it is intuitive that all the FOR needs to be under surveillance in the same way, since maximum possible closure rates do not depend on the angular position of the obstacles (azimuth angle φ in Figure 3.1). As speed increases, if one considers possible collision conditions, there is an increase of closure rates in the velocity direction and a reduction in the lateral areas. As a limit case, when the own-ship speed is much larger that the obstacle one (which of course is true for fixed obstacles), possible conflict conditions are concentrated around the current velocity vector. The dependence of closure rate on the azimuth angle (with respect to the velocity vector) in near-collision conditions can be expressed by numerical or simplified analytical models. As an example, Figure 3.2 reports the closure rate as a function of the azimuth angle for intruder velocity norm (V_{INT}) equal to 15 m/s and for variable ownship velocity norm (V_{UAV} equal to 5, 10, and 15 m/s). The envelope of maximum closure rates for the assumed intruder and ownship velocity is depicted in red. Closure rates in collision conditions can be combined with a target t_{CPA} to define the basic range requirements to be considered for the obstacle sensing system. This is applicable in real-time (accounting for the current velocity) and at design level, where the envelope of worst-case closure rates can be adopted. It is clear that the approach will be conservative for intruders that are slower than the fastest possible ones.

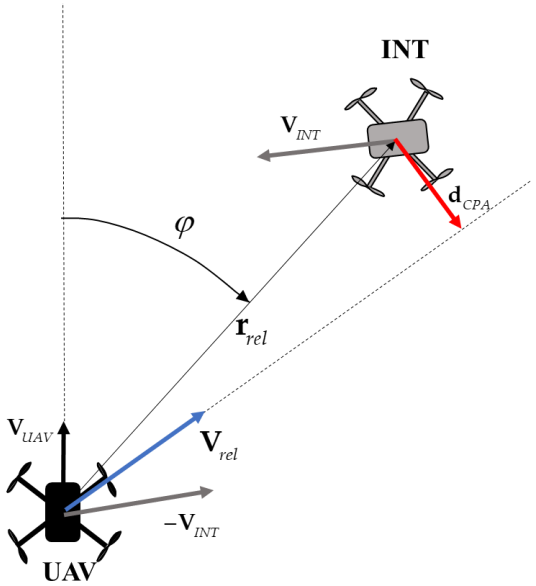

Figure 3.1 Graphic illustration of a collision scenario between an ownship (UAV) and intruder (INT).

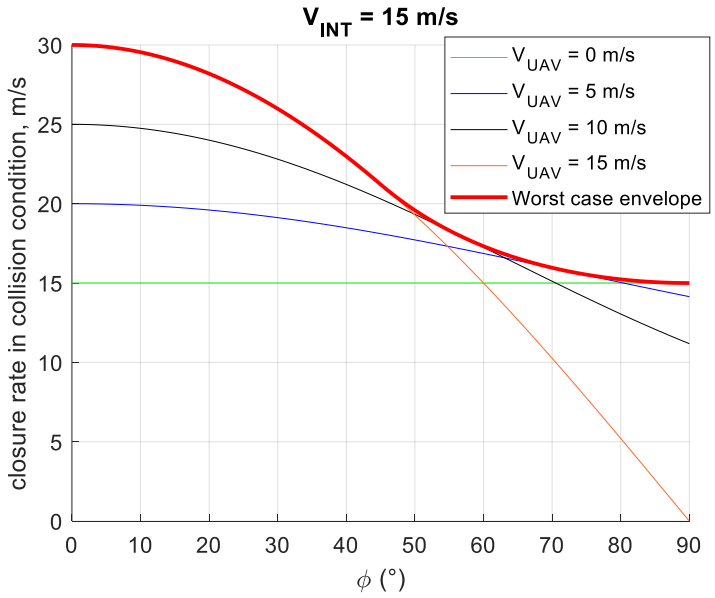

Figure 3.2 Variation of closure rate within the field of regard assuming collision conditions.

From a practical point of view, the adaptive sensing approach can be implemented in different ways. Within detection algorithms, the adopted thresholds and even the structure of the detectors can be adapted to the desired declaration range, potentially leading to a better missed detections / false alarm trade-off whenever the detection range requirements are relaxed. Considering ML-based concepts, the idea is to adapt the detectors and the scoring thresholds to the current conditions. The same concept can be applied to other detection strategies such as the ones based on morphological filtering. At architectural level, the target t_{CPA} and the consequent variable range requirements can be accounted for when selecting multi-sensor-based architectures to cover a wide FOV.

3.2 CONFLICT DETECTION ANALYSIS FOR MULTI-SENSOR ARCHITECTURES

Depending on the available information from sensing sources, different conflict detection criteria can be adopted [10]. With reference to the 2D horizontal scenario of Figure 3.1, if the platforms are constrained to move along a straight line, the distance at closest point of approach can be computed in its vectorial form ($\mathbf{d}_{\mathrm{CPA}}$) as in Eq. (3.1), where $\mathbf{V}_{\mathrm{rel}}$ and $\mathbf{r}_{\mathrm{rel}}$ are the relative velocity and position vectors, respectively.

$$\mathbf{d}_{\mathrm{CPA}} = \frac{\mathbf{r}_{\mathrm{rel}} \cdot \mathbf{V}_{\mathrm{rel}}}{|\mathbf{V}_{\mathrm{rel}}|^2}\mathbf{V}_{\mathrm{rel}} - \mathbf{r}_{\mathrm{rel}} = t_{CPA}\mathbf{V}_{\mathrm{rel}} - \mathbf{r}_{\mathrm{rel}} \tag{3.1}$$

The value of t_{CPA} can be also computed accounting for these quantities as shown in Eq. (3.2).

$$t_{CPA} = \frac{\mathbf{r}_{\text{rel}} \cdot \mathbf{V}_{\text{rel}}}{|\mathbf{V}_{\text{rel}}|^2} \tag{3.2}$$

Based on the definitions in the previous equations, a collision between the two platforms is expected to occur whenever the norm of the estimated $\mathbf{d}_{\text{CPA}}$, as measured by onboard sensors ($d_{CPA,est}$), falls below a threshold ($d_{CPA,th}$). Thus, in the assumed 2D horizontal encounter, the latter quantity can be seen as the radius of a circumference centred at the intruder position and representing a safety area which shall not be violated. Considering the uncertainty in $d_{CPA,est}$ (i.e., σ_{dCPA}), which depends on the chosen non-cooperative sensors specifications and tracking performance, the conflict detection condition can be written as in Eq. (3.3).

$$d_{CPA,est} < d_{CPA,th} + \sigma_{dCPA} \tag{3.3}$$

Due to the dependence on relative position and velocity, this conflict detection criterion is only suitable for a sensing system which measures range and velocity information, as in the case of LiDARs or RADARs. Indeed, when passive (EO) sensors, like visual cameras, are used, a different collision criterion must be applied. In this case, the estimate of the LOS between the ownship and the intruder (typically identified by a couple of angles) is exploited, and a collision can be inferred whenever the intruder LOS rate reaches zero degrees-per-seconds. This latter condition corresponds, in fact, to a constant relative angular position between the two platforms. Such eventuality can be more practically expressed by comparing the sensor estimated LOS rate ($LOSrate_{est}$) with a threshold ($LOSrate_{th}$), again accounting for the uncertainty in the LOS rate estimation ($\sigma_{LOSrate}$). Following these considerations, the visual-based conflict detection condition can be written as in Eq. (3.4).

$$LOSrate_{est} < LOSrate_{th} + \sigma_{LOSrate} \tag{3.4}$$

The identification of a proper value of $LOSrate_{th}$ is critical to the validity of this criterion. This latter quantity can be computed from Eq. (3.1) by assuming near-collision conditions which lead to an approximated definition of the norm of $\mathbf{d}_{\text{CPA}}$ as

in Eq. (3.5), where r is the norm of the relative position vector (range) and $\dot{r}$ (range rate) is obtained from its derivative.

$$d_{CPA} \approx \frac{r^2}{\dot{r}} LOSrate \tag{3.5}$$

Hence, $LOSrate_{th}$ can be computed as in Eq. (3.6) by assuming worst-case conditions, i.e., maximum possible range rate ($\dot{r}_{max}$) and minimum distance (r_{min}), leading, however, to a highly conservative conflict detection criterion.

$$LOSrate_{th} = \frac{d_{CPA,th}|\dot{r}_{max}|}{r_{min}^2} \tag{3.6}$$

In the adopted conflict detection method, $\dot{r}_{max}$ is chosen based on the previous considerations for near collision closure rates variations with ownship speeds and FOR sectors. Instead, to avoid either over- or under-conservative conflict detections, the values of r_{min} are varied depending on the actual distance of the intruder with respect to the ownship.

The proposed concept requires the estimation of distance measurements from visual information. This is carried out by exploiting coarse range estimates achievable using shape-based methods which, however, can only be reliably applied when the dimensions of the projection of the intruder on the image plane are large enough for its class to be recognized (e.g., of the order of few tens of pixels along its main direction). Therefore, three range regions can be defined. A "far range" region ($r \geq r_t$), where the intruder projection occupies only few pixels, and no class/range information is available; a "medium range" region ($r_c < r < r_t$), where lower bounds for intruder range can be set in a more realistic way; a "close range" region ($r \leq r_c$), where range estimates are reasonably accurate and can be exploited for conflict detection (or even used to exploit 3D techniques as in Eq. (3.3) if range rate accuracy is also sufficient).

3.2.1 Statistics for the assessment of conflict detection

To assess the performance of a given architecture at conflict detection level, the probabilities of missed conflict detection (P_{MD}) and false conflict detection (P_{FA}) can be computed. P_{MD} and P_{FA} depend on the operations and results which arise during the tracking phase and are, specifically, related to the probability of declaring

a reliable, i.e., firm, track of an existing intruder. Given the actual presence of an intruder on a collision course with the ownship, a missed detection can occur either if such intruder is not declared by the tracking algorithm or if, though being correctly tracked, the retrieved estimates do not verify any conflict condition (either (3.3) or (3.4)) depending on the available information). Similarly, a false alarm can be caused by the sensing system declaring a non-existing collision with an actual colliding intruder or by the declaration of a false intruder (at tracking level) whose estimates verify the exploited collision criterion. This latter eventuality occurs, regardless of the presence of real intruders, with a probability that is given by the product of the false track generation probability ($P_{FalseTrack}$) and false alarm given a generated false track probability ($P_{FA|FalseTrack}$).

P_{MD} and P_{FA} are strongly related to the collision criterion in use and can be computed by following the approach of [99]. Hence, Gaussian distributions for both $d_{CPA,est}$ and $LOSrate_{est}$ are assumed with mean values equal to their actual values and standard deviations equal to σ_{dCPA} and $\sigma_{LOSrate}$, respectively. The same assumption can be made on the declaration range, i.e., r_{FT}, based on which the firm tracking probability is established. The latter is also assumed to be distributed as a Gaussian random variable with mean equal to μ_{FT} and standard deviation equal to σ_{FT}.

3.3 IMPROVED VISUAL CONFLICT DETECTION STRATEGY

The possibility to improve conflict detection performance of purely visual-based DAA architectures by exploiting estimates of the intruder range is discussed in this section. If the type of intruder, and, consequently, the size of its cross section is known, range estimates can be retrieved using the shape-based ranging principle. Specifically, if N_{pix} is the size of the intruder projection on the image plane (e.g., in the horizontal direction), using the pinhole camera model and under the classical perspective projection geometry, the target range (r) can be estimated as in Eq. (3.7). Here, f is the camera focal length (expressed in pixels), and L is the physical size of the target (in the same direction along which N_{pix} is evaluated).

$$r = \frac{fL}{N_{pix}} \tag{3.7}$$

The value of N_{pix} can be obtained by processing the neighbourhood of the detected position of the intruder on the image plane with binarization techniques to separate it from the local background [100]. If the visual detection task is entrusted to a Deep-Learning-based (DL) neural network, the neighbourhood is defined based on the detected Bounding Box. However, when the intruder is very far, and, consequently, its projection occupies very few pixels, the range estimate is unreliable due to the inherent limited sensitivity shown in Eq. (3.7) and the difficulty in recognizing if the entire intruder shape or only a portion of it produces enough contrast on the image plane. So, a N_{pix} threshold (N_t) should be set, below which the shape-based ranging method is not applicable even if the class of the intruder is known. Clearly, more in general, being the considered DAA framework non-cooperative, the intruder type will likely be unknown a priori. Nevertheless, as the range reduces, it is reasonable to assume that when the projection on the image plane is large enough, image processing algorithms (e.g., relying on artificial intelligence techniques) can identify the class of the intruder and allow selecting the correct value of L. Therefore, another threshold N_c (greater than N_t), must be introduced above which the shape-based ranging principle becomes applicable. The condition $N_{pix}>N_c$ must be verified on a multi-temporal basis (i.e., over a sequence of subsequent frames) so that the estimate of N_{pix} can be confirmed and used for range estimation.

The shape-based ranging principle is integrated within a visual based non-cooperative DAA architecture composed of three main processing blocks, namely detector, tracker, and conflict analyser [62] with the following roles.

- The detector processes images collected by a RGB camera to obtain a set of single frame detections exploiting a You Only Look Once (YOLO) v2 neural network [101].
- The tracker aims at associating multiple detections of the same potential intruder through subsequent frames to generate a firm track and estimate angular rates (further details on the tracking methodology are given in section 5.2).
- The conflict analyser implements a LOS-based conflict detection criterion to establish whether a potential collision is to be declared, processing only the firm tracks.

Range estimation technique is only applied at firm tracking level. This allows using a less conservative LOS-based criterion by substituting the minimum range in Eq. (3.6) with a more realistic range estimate. Hence, the adaptive LOS-based conflict detection criterion is obtained by computing $LOSrate_{th}$ as shown in Eq. (3.8).

$$LOS_{rate,th} = \begin{cases} d_{CPA,th} \dfrac{\dot{r}_{\max}}{r_{\min}^2} & N_{pix} \le N_t \\ d_{CPA,th} \dfrac{\dot{r}_{\max}}{r_c^2} & N_t < N_{pix} \le N_c \\ d_{CPA,th} \dfrac{\dot{r}_{\max}}{r^2} & N_{pix} > N_c \end{cases} \tag{3.8}$$

Specifically, when $N_{pix}<N_c$, a constant r_{min} is assumed and its value is chosen depending on whether N_{pix} is greater or smaller than N_t, in analogy with the "far range" and "medium range" concepts defined in section 3.2. When $N_t<N_{pix}< N_c$, r_{min} can be set to r_c. Whilst, in "far range" condition, $r_{min}=r_t$. Conversely, when N_{pix} is higher than N_c, a new $LOSrate_{th}$ is computed by using a variable r_{min} equal to the actual range estimated by the shape-based technique.

To avoid that a wrong detection (caused by blurred image projections of far-range intruders) at single-frame level can produce very high values of $LOSrate_{th}$, potentially yielding to missed conflict declaration, the condition $N_{pix}>N_c$ must be verified on multi-temporal basis. Therefore, confirmed range estimates are declared if $N_{pix}>N_c$ and there are at least n_f previously estimated ranges, whose difference from the current range is compliant with the maximum possible range rate of the intruder. If the N_{pix} information is missing at a certain epoch (i.e., no single frame detection is associated to the firm track), the value of $LOSrate_{th}$ at the previous epoch is adopted.

3.4 NUMERICAL SIMULATION RESULTS

In the following, the performance of two different multi-sensor architectures, in which different sensors are used to cover specific regions of the own-ship FOR is investigated. The analyses focus on azimuth angles going from -90° to +90°, however, only positive azimuth angles are considered given the symmetry of the problem. Both architectures exploit higher performing sensors in the central sector of the FOR, which requires larger declaration ranges than the lateral ones. Following

this idea, the FOR region in the interval from 0° to 90° can be decomposed in two areas which are highlighted in green and blue in Figure 3.3. The separation of these sectors occurs at a specific azimuth angle (φ_R) with respect to the UAV velocity vector, aligned with the first axis of its body-centered reference frame, (x_B in Figure 3.3). Therefore, higher range sensors are considered to operate in the interval $0°<\varphi<\varphi_R$. Whereas, lower range sensors are used for $\varphi_R<\varphi<90°$. Lateral sensors are assumed to be cameras in both the architectures while the central region is covered by a RADAR and a higher performance visual camera in the first and second architectures, respectively.

Table 3.1 and Table 3.2 list all the parameters relevant to the two architectures. These parameters are selected assuming sUAV-to-sUAV scenarios and also accounting for considerations expressed in section 3.1. More precisely, the quantities σ_{az}, σ_{el}, σ_r and $\sigma_{\dot{r}}$ represent the performance of the single sensors in measuring azimuth, elevation, range and range rate (the latter two only apply to the RADAR case).

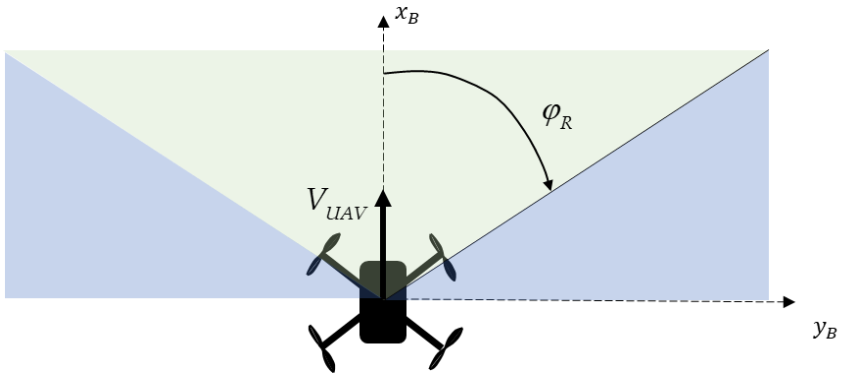

Figure 3.3 Graphic illustration of the FOR of the ownship UAV and the FOV of the different sensors. Central FOR is depicted in green and centered at the x_B axis. Lateral FOR is depicted in blue.

Table 3.1 Statistics of the RADAR-camera simulated architecture.

	RADAR	***Camera***
Covered φ/2	0° - 60°	60° - 90°
μ_{FT}, σ_{FT}	400 m, 50 m	225 m, 50 m
$P_{FalseTrack}$, $P_{FA\|FalseTrack}$	0.1, 0.2	0.1, 0.2
σ_{az}, σ_{el}	1°, 3°	0.2°, 0.2°
$\sigma_{LOSrate}$	0.71 °/s	0.14 °/s
σ_r, $\sigma_{\dot{r}}$	3.25 m, 0.9 m/s	5 m, 1 m/s (in very close range conditions)

Table 3.2 Statistics of the two cameras simulated architecture.

	Frontal camera	***Lateral camera***
Covered $\varphi/2$	0° - 45°	45° - 90°
μ_{FT}, σ_{FT}	275 m, 75 m	225 m, 50 m
$P_{FalseTrack}$, $P_{FA\|FalseTrack}$	0.3, 0.4	0.1, 0.2
σ_{az}, σ_{el}	0.2°, 0.2°	0.2°, 0.2°
$\sigma_{LOSrate}$	0.14 °/s	0.14 °/s
σ_r, $\sigma_{\dot{r}}$	5 m, 1 m/s (in very close range conditions)	5 m, 1 m/s (in very close range conditions)

Figure 3.4 shows the variation of $LOSrate_{th}$ in the FOR for different V_{UAV} values and for a velocity of the intruder which is assumed to be known (from airspace regulations for instance) and equal to V_{INT}=15 m/s. The threshold on distance at closest point of approach is set to $d_{CPA,th}$=30 m. The assumed minimum values of distance are $r_{min}=r_c$=70 m, and $r_{min}=r_t$=150 m in the medium range (70 m<r<150 m) and far-range ($r\geq$150 m) conditions, respectively. The maximum closure rate values ($\dot{r}_{max}$) account for near-collision conditions and the variation in the FOR shown in Figure 3.2. The strong decrease in $\dot{r}_{max}$ (reduced down to 0 m/s) verified when $V_{UAV}=V_{INT}$=15 m/s and the azimuth approaching 90°, yields to a similar behaviour in $LOSrate_{th}$. Thus, to avoid using very low thresholds, leading to an over-conservative condition, a limit on $LOSrate_{th}$ is imposed at 0.8 °/s and 1.6 °/s for the far and medium range cases, respectively. This limit is reflected in the plateau reached by the orange lines of Figure 3.4.

The results of the multi-sensor architectures in terms of P_{MD} and P_{FA} are evaluated for $d_{CPA,th}$=30 m, V_{INT}=15 m/s, t_{CPA}=10 s and varying values of d_{CPA} and V_{UAV}. When focusing on camera-based conflict detection criterion, the proposed adaptive strategy accounting for a varying $LOSrate_{th}$ depending on the range region (Figure 3.4) is adopted. Specifically, the numerical simulation carried out with the aforementioned values results in intruder's ranges which vary in the FOR as shown in Figure 3.5. Here, the lower limits of the far-range (yellow dashed line) and medium range (red dashed line) regions are shown. As it can be seen, in the case of d_{CPA}=50 m (top figure), close-range condition is never verified, and medium-range condition is only verified in the lateral region (φ>80°) when the two UAVs have the same speed. Instead, when d_{CPA}=15 m (bottom figure), close-range condition is only verified for a very small angular sector of the FOR (φ close to 90°). Thus, the d_{CPA}-

based conflict detection criterion for the camera, assuming reliable range estimates achieved with the shape-based method, is practically never used in the cases under consideration.

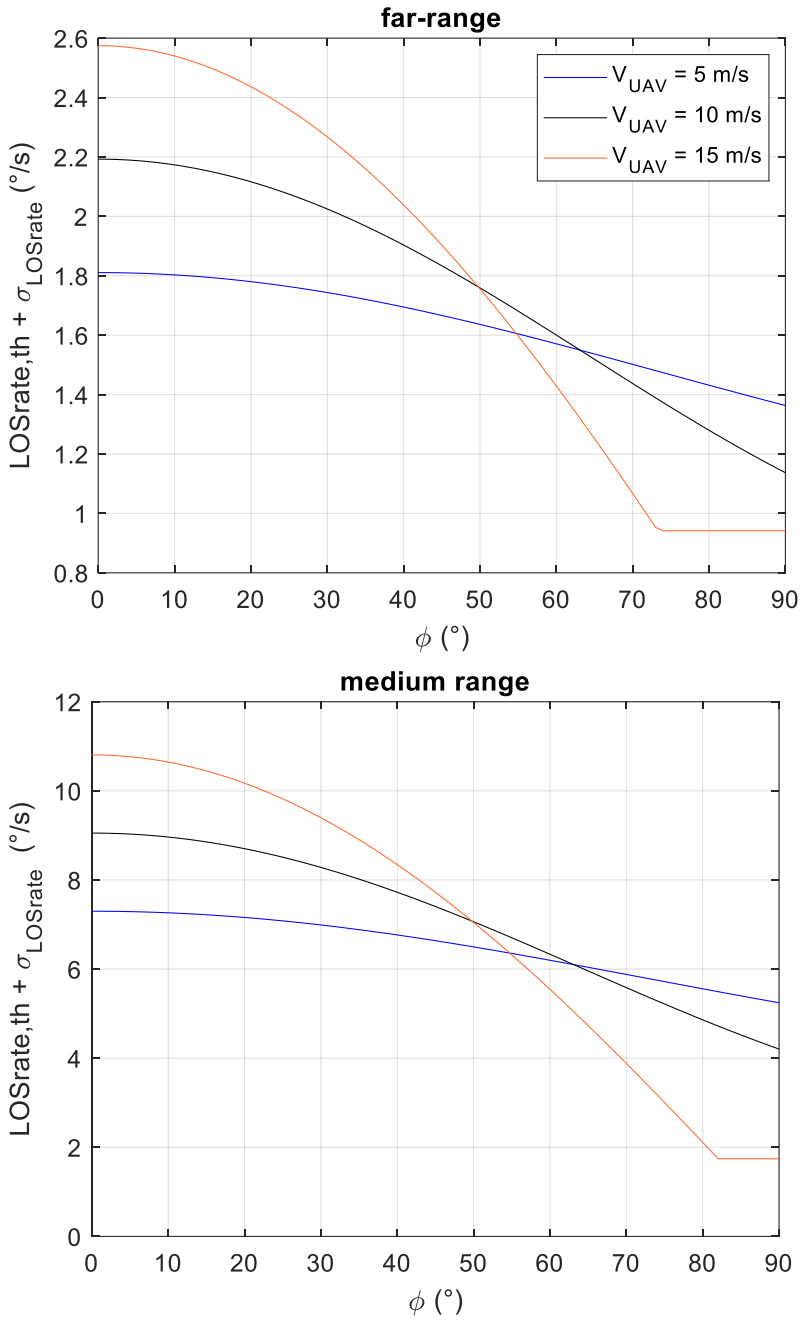

Figure 3.4 *LOSrate*$_{th}$ used in far-range (top) and medium-range (bottom) regions for varying V_{UAV} and V_{INT}=15 m/s.

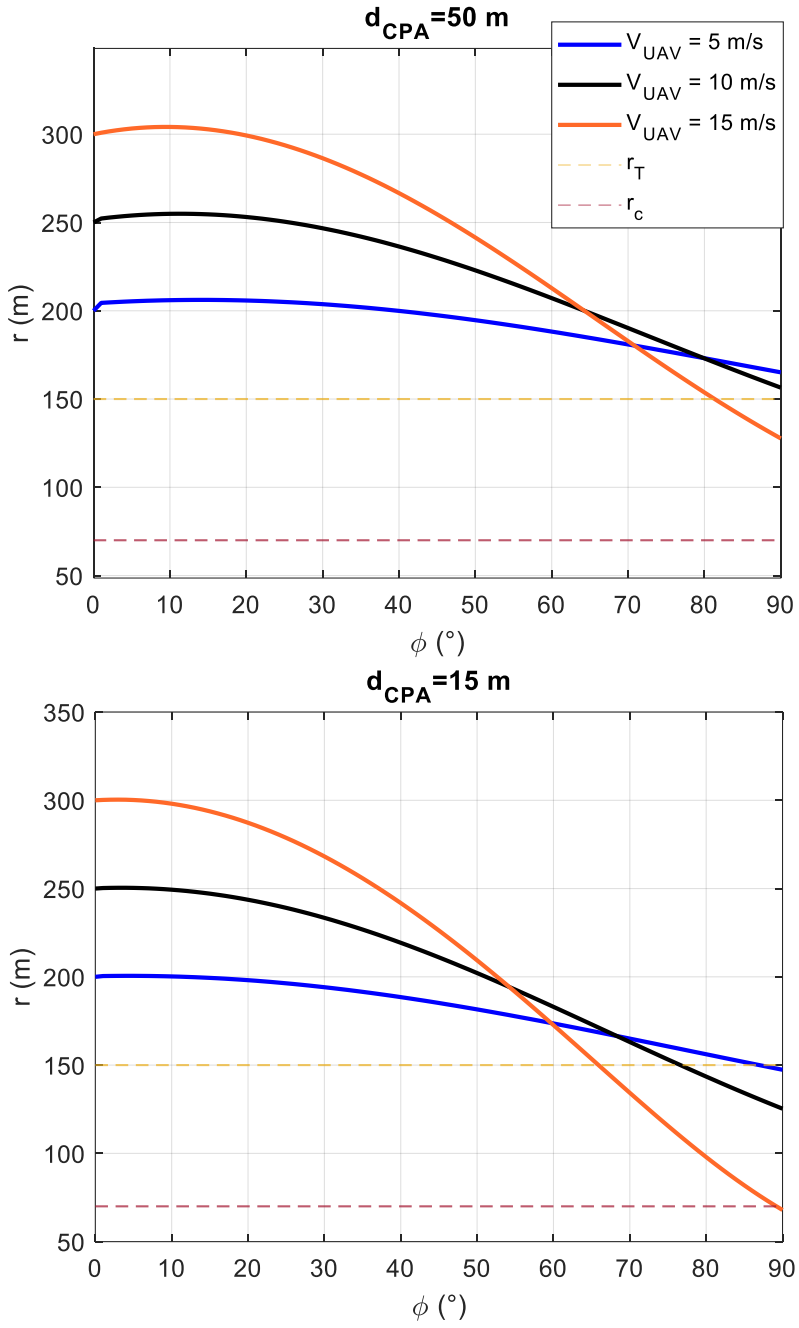

Figure 3.5 Range of intruder for varying V_{UAV} resulting from numerical simulation using t_{CPA}=10 s and V_{INT}=15 m/s. Top: d_{CPA}=50 m. Bottom: d_{CPA}=15 m.

Results for the RADAR-camera system in terms of P_{MD} computed for d_{CPA}=15 m are shown in Figure 3.6 (a). P_{MD} reduces monotonically with increases in the azimuth, except for a sudden peak (of about 0.2) at the boundary between the FOVs of the two sensors (φ=60°). This is due to the reduction of the firm tracking probability when switching from the central RADAR to the lateral visual system. In the central region, assumed to be covered by the RADAR, the higher values of range of the intruder promote a lower firm tracking probability for increasing values of

V_{UAV}, this generates a slight increase in P_{MD}. Indeed, in the lateral regions, P_{MD} improves for increasing V_{UAV} due to the reduction of the range that corresponds to the chosen t_{CPA}. P_{FA} results, at equal t_{CPA} but higher d_{CPA} (50 m), are shown in Figure 3.6 (b). Once again, a degradation in the RADAR-based conflict detection performance is observed (central FOR) for increasing V_{UAV}. The relatively large P_{FA} value is due to the fact that the assumed d_{CPA} is close to the threshold, thus false conflict detections are more likely to occur. As in the case of P_{MD}, a sudden increase in P_{FA} is also verified when transitioning from one sensor to the other. In this case, a second peak can also be noticed at $\varphi \approx 81°$ when V_{UAV}=15 m/s. The latter is due to the transition from far-range to medium range region which triggers the use of a higher $LOSrate_{th}$.

In summary, using a lower performance sensing architecture in the lateral areas of the FOR and exploiting an adaptive conflict detection strategy allows achieving similar performance with respect to the RADAR-based ones exploited in the central area.

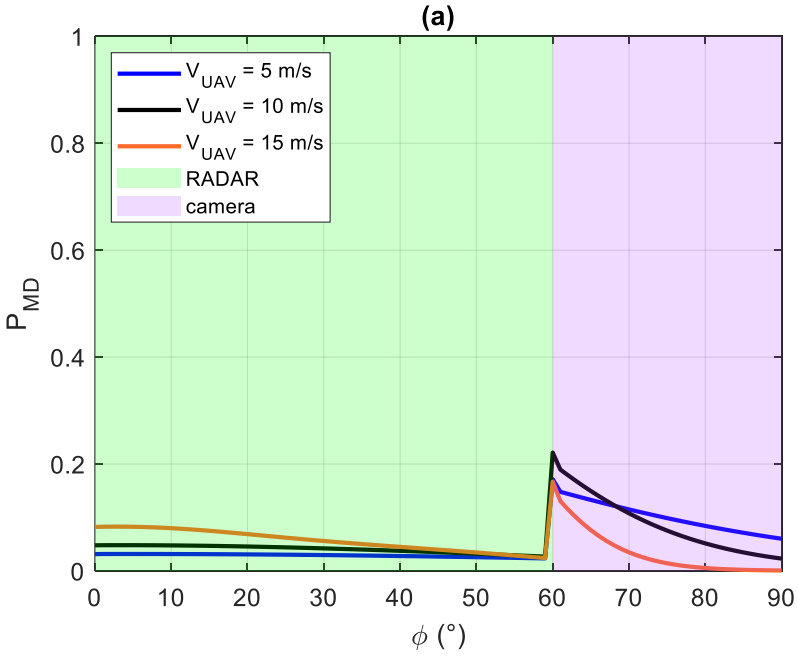

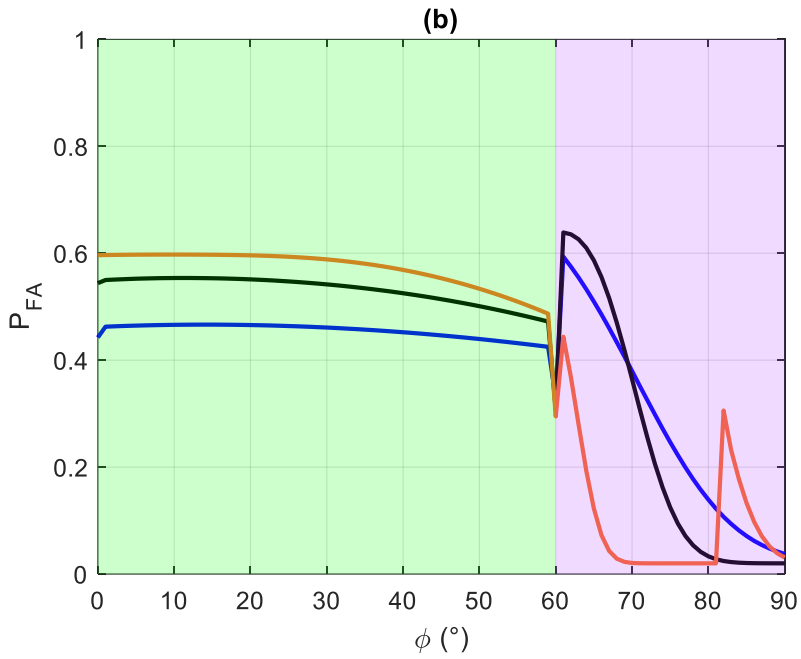

Figure 3.6 Performance of the RADAR-camera architecture for varying V_{UAV}, V_{INT}=15 m/s and t_{CPA}=10 s. (a): P_{MD} at d_{CPA}=15 m. (b): P_{FA} at d_{CPA}=50 m.

In the second architecture, a visual system with a larger declaration range is assumed in the central area of the FOR. The idea is to use different algorithmic settings, thus improving the detection range at the expense of a larger probability of false track generation. Intuitively, due to the lower probability of firm track, such architecture is expected to exhibit worse P_{MD} performance with respect to the RADAR-based ones. Instead, the exploitation of different algorithmic settings in the different areas allows an improvement in P_{FA} performance with respect to an equally set cameras configuration, where the frontal settings are adopted in the entire FOR. This is shown in Figure 3.7, where the comparison between the two configurations, i.e., "different settings" and "equal settings", is presented for V_{UAV} =10 m/s and t_{CPA}=10 s. The exploitation of the different settings, with decreased false track generation probability for the lateral cameras, leads to an advantageous decrease in P_{FA} for φ>45°. This is paid with an increase in P_{MD}, with a peak occurring right at the separation between the two cameras. However, the latter peak appears to be comparable to the values of P_{MD} achieved within the frontal region, thus potentially representing an acceptable performance trade-off.

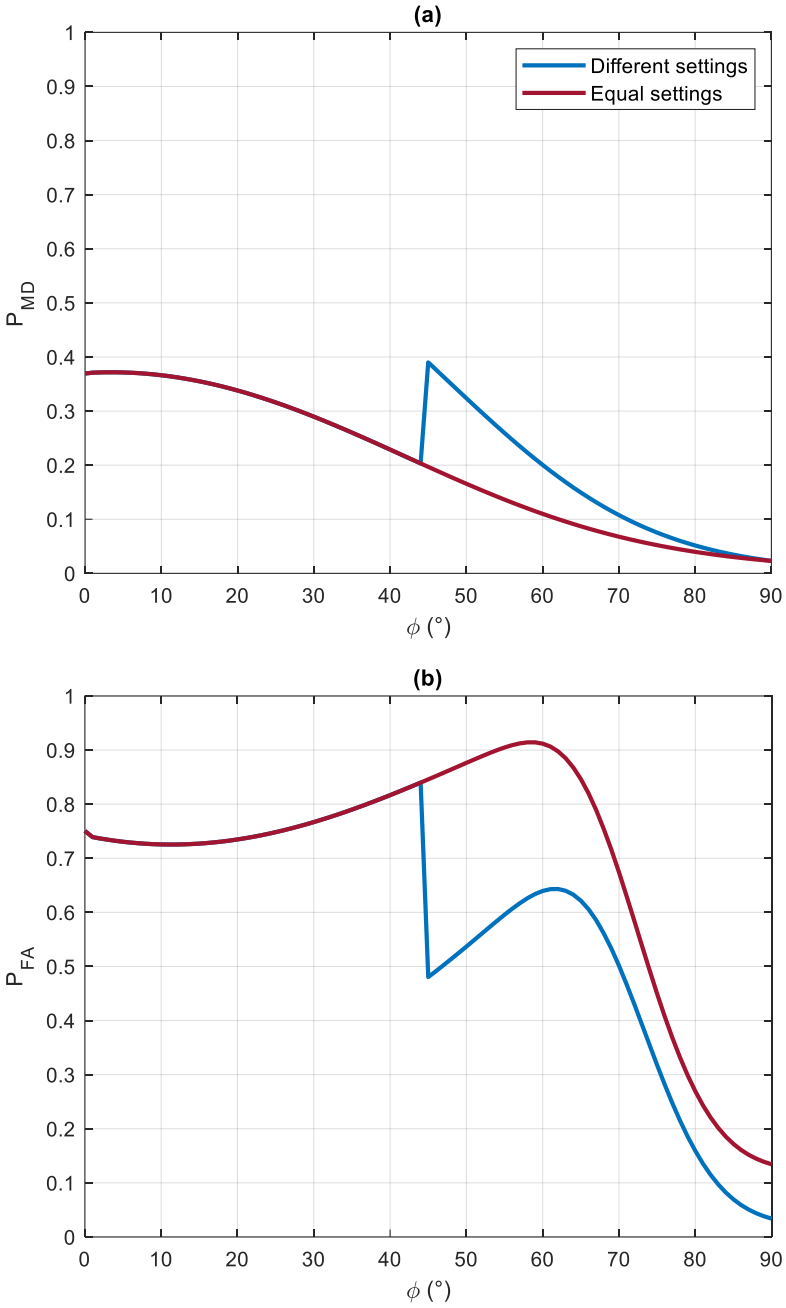

Figure 3.7 Performance of the two cameras architecture (blue line) for V_{UAV}=10 m/s, V_{INT}=15 m/s and t_{CPA}=10 s. Comparison with equally set cameras used in the whole FOR is provided (red line). (a): P_{MD} at d_{CPA}=15 m. (b): P_{FA} at d_{CPA}=50 m.

3.5 EXPERIMENTAL RESULTS ON IMPROVED VISUAL SENSING

Experimental data collected during the flight of two customized DJI M100 platforms are used to evaluate the accuracy of the shape-based ranging method and its effect on a purely visual-based DAA architecture exploiting the proposed adaptive conflict detection criterion (Eq. (3.8)) discussed in section 3.33.3. The platforms are both equipped with an onboard computer, visual camera and an additional GNSS

receiver. During experiments, one drone was used as the own-ship, capturing images of the other drone, “Athena”. Further details on the equipment of the platforms can be found in section 4.3 of the manuscript. The two drones were remotely piloted along trajectories specifically tailored to emulate six encounters during which the intruder appears AH in the own-ship-collected frames. The intruder UAV is shown on ground and during flight (as imaged by the own-ship) in Figure 3.8 .

The estimated range as a function of the true one, merging data of all the encounters, is shown in Figure 3.9. Correct predictions should lie on the black line representing the y=x equation. The figure suggests that the shape-based ranging technique provides a reliable range up to 150 m, which corresponds to N_{pix}=8 pixels, for the specific intruder. The cluster of points located in the right bottom corner of Figure 3.9 identifies the points which return a very small range (and large N_{pix}) even if the true range is very high. However, these incorrect measurements are discarded by the previously described “range tracking” method.

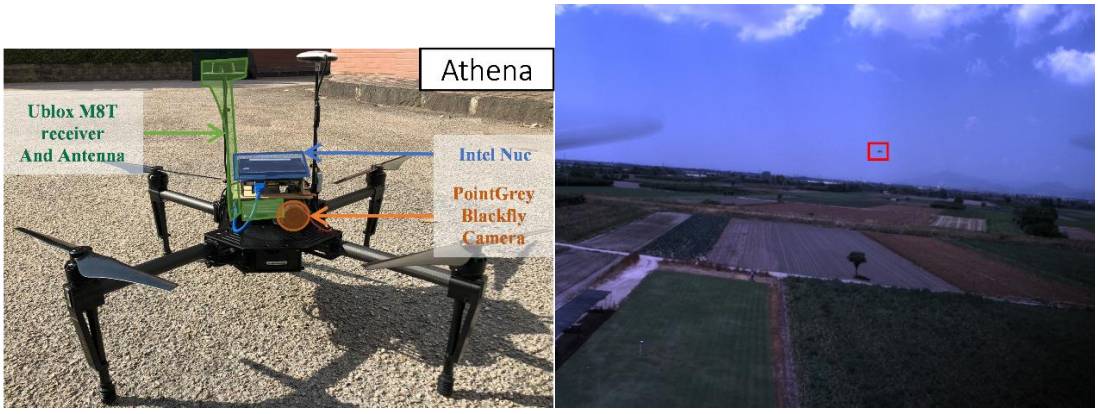

Figure 3.8 Left: Athena (intruder UAV) and its constitutive components. Right: Athena (intruder UAV within the red rectangle) seen by the ownship during flight.

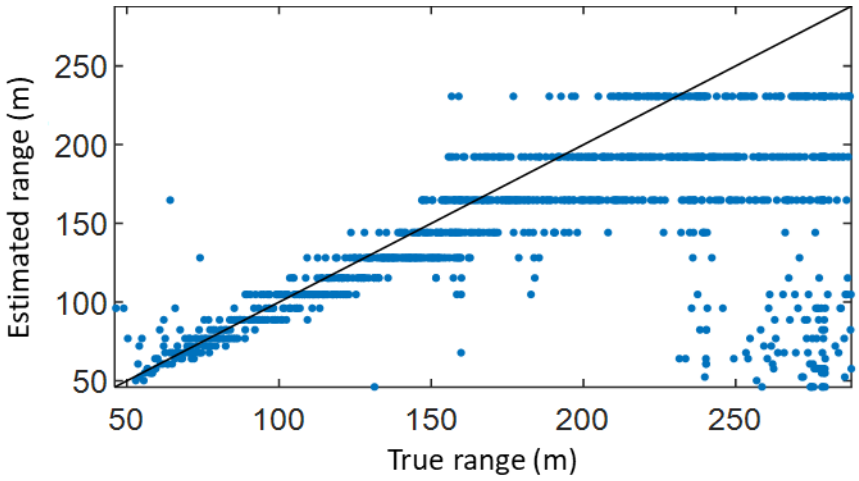

Figure 3.9 Range predicted from shape-based technique, for the six encounters. Estimated vs true range.

Figure 3.10 shows the estimated *LOSrate*, d_{CPA} and their threshold ($d_{CPA,th}$ is set to 30 m), along with the true and estimated range during encounters 1 and 2. True d_{CPA} and *LOSrate* are obtained by processing GNSS data and used as reference for conflict detection performance. True d_{CPA} and its threshold are reported in Figure 3.10b. The first subplot, referred to as a), reports the true and estimated LOS rate by the tracker, along with the LOS rate thresholds $L_t=LOSrate_{th}+\sigma_{LOSrate}$ obtained by setting r_t=150 m, and:

Case 1. $N_t=N_c=\infty$ (blue line), so that the nominal LOS-based criterion, with constant $r_{min}=r_t$=150 m is used along the whole encounter.

Case 2. $N_t=N_c$=8 (orange). In this case the range information can be used when N_{pix}>8, and $r_c=r_t$=150 m.

Case 3. N_t=8 and N_c=16 (yellow). In this case the three zones criterion as in Eq. (3.8) is adopted and a constant r_c=70 m is assumed when the number of pixels is in between N_t and N_c. The value of r_c is the range obtained from Eq. (3.7) with $N_{pix}=N_c$=16.

Estimated ranges by the shape based ranging technique, are reported in Figure 3.10c, only when the multi-temporal analysis provides consistent results. All the confirmed ranges defined both in case 2 and 3 are reported, along with the range thresholds $r(N_{pix})$ associated to N_{pix}=8 and N_{pix}=16. Using an adaptive LOS rate threshold makes the LOS-based criterion more consistent with the actual collision conditions. This is clearly shown in the last part of encounter 2 (right Figure 3.10),

i.e., time>263 s, where the UAV is still in conflict with the intruder ($d_{CPA}<d_{CPA,th}$), but the LOS-based criterion with constant range would not declare collision, unlike the adaptive one.

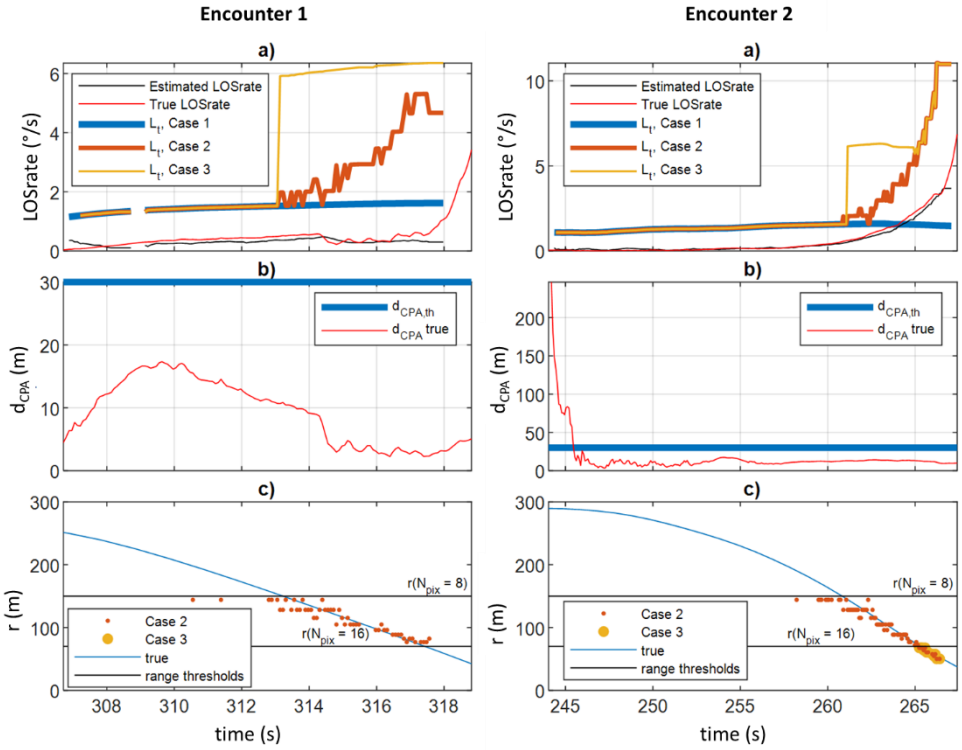

Figure 3.10 a) LOS rate and LOS rate threshold, b) d_{CPA} and d_{CPA} threshold, b) true and estimated range by shape-based ranging technique. Left: Encounter 1. Right: Encounter 2.

Chapter 4: Experimental datasets

The investigation of sensing requirements and performance can be carried out, at a relatively low cost, exploiting simulation-based environments. Research approaches based on this idea have been fuelled by the recent progress in graphics and power budgets of modern processing units which are enabling the generation of synthetic data for both visual and RADAR domains, building up photo-realistic datasets for the training of DL-based detectors [102] and RADAR data for micro-Doppler signature identification [103]. Simulation-based solutions are a powerful and valuable tool, particularly useful in cases where initial assessments are sought. However, the availability of experimental data, collected in scenarios which are relevant to the use case, is a crucial step for the validation and testing of sensing solutions which need to adapt and respond to real world challenges. During this research work, major effort was devoted to the collection of data gathered with low-altitude-flying sUAVs using non-cooperative sensors. Therefore, before presenting the methodologies and results on UAV sensing strategies, this chapter provides a description of the experimental tests carried out to collect data with ground-based sensors, co-located RADARs and visual cameras, and flying sUAVs. The use of multiple sensing sources, with their inherent clocks, requires alignment solutions apt to retrieve a common time-tag, thus enabling data synchronization. In this context, spatial alignment, which implies the attitude determination of sensors within a common reference frame, is also of paramount relevance. Both methodologies, are discussed in this section.

In this work, performance of the proposed sensing strategies are evaluated exploiting two main datasets, corresponding to field tests carried out in different locations. In both, the same ground-based sensing setup and airborne platform were used, as described in section 4.1. The methodologies used for ground-based sensor alignment, also supporting alignment with devices onboard the UAV, are discussed in section 4.2. Finally, flights performed to build-up the datasets are presented in section 4.3.

4.1 GROUND-BASED AND AIRBORNE SETUP

The sensing setup deployed during experiments consists of a low SWaP FMCW scanning array RADAR, visual camera and GNSS receiver and antenna. All devices were connected to a single ground station (Lenovo ThinkPad laptop with Ubuntu operating system) used to trigger data acquisition and logging.

The choice of RADAR device fell on the Echoflight MESA RADAR manufactured by Echodyne [104] whose compact dimensions and wide FOV, listed in Table 4.1, represent highly favourable characteristics for its use in both ground and airborne DAA/surveillance applications. A further useful feature is the availability of different data packets which go from raw measurements (*RVmaps* packet) to fully processed tracks (*tracks* packets). During the acquisitions, the *detections* data packet containing measurements in terms of azimuth (*az*), elevation (*el*), range (*r*) and range rate ($\dot{r}$) was logged, achieving a sampling frequency of about 133 Hz. This choice was made based on the data transmission and storage capability of the ground station, which can hinder the logging of *RVmaps*, and on the need to assess the performance of the sensor with the proposed tracking strategy, thus *tracks* were intentionally avoided. The operational principle of the device implies the generation of consecutive beams to recover a grid-like scan of the whole FOV, whose dimensions are defined based on the minimum and maximum values of azimuth and elevation (az_{min},az_{max}) and (el_{min},el_{max}), respectively. The latter values can be set accordingly to user specifications. The angular distance between two consecutive beams is also user-definable and is referred to as Δaz (horizontal angular separation) and Δel (vertical angular separation) in the following. As far as the visual camera is concerned, the setup is equipped with a RGB Blackfly BFS-U3-31S4C-C USB 3.1 device manufactured by Teledyne FLIR [105]. The latter also respects very low SWaP constraints, typical of this class of devices, showing an instantaneous FOV of about 0.02° and resolution slightly above 3 Megapixels, as also reported in Table 4.2, where the focal length of the lens attached to the camera is also provided. Although providing a maximum frame rate of about 55 fps, during tests the camera was used acquiring frames with a frequency of about 10 Hz, thus better responding to data writing budgets of the ground station while not impacting sensing requirements. A single-constellation uBlox GNSS LEA-6T receiver (with coupled antenna) is also

part of the sensing suite and is used to recover precise localization of the sensors as well as GNSS timing with a frequency of 1 Hz.

Table 4.1 Specifications of RADAR.

Echoflight RADAR	
Frequency	24.45-24.65 GHz
FOV	120° (az) x 80° (el)
Instrumented range	6 km
Operating Power	45 W
Size	18.7 cm x 12 cm x 14 cm
Weight	817 g
Data packets	*Detections,Measurements,Tracks, R/Vmaps*

Table 4.2 Specifications of visual camera.

Blackfly BFS-U3-31S4C-C	
FOV	48° (az) x 37° (el)
IFOV	About 0.02°
Lens focal length	8 mm
Image dimension	2048 x 1536 pixels
Frame rate	55 fps
Weight	36 g

To acquire data from the different sensors, an *ad-hoc* C++ acquisition code was developed and installed on the ground station. The software is responsible for the writing of data in pre-defined .bin files. Each data (from each source) is coupled with a time-tag to enable precise synchronization.

The flight segment used as flying target (or intruder) during tests is a customized version of a DJI M100 platform, “Eagle”, which is shown on ground in Figure 4.1. The UAV is equipped with an onboard computer (Intel NUC with i7 CPU), an additional GNSS single frequency receiver with multi-constellation and raw data capability (uBlox M8T) and a CMOS camera (PointGrey Flea FL3-U3-20E4C-C) with a 8-mm focal length lens. By exploiting data collected by both onboard and ground-based uBlox receivers, highly accurate relative positioning estimates between the two platforms can be retrieved by using CDGNSS processing by means of RTKLIB [106]. Such data is extensively used both as a benchmark for the tracking performance evaluation as well as for the ground sensors attitude determination in NED.

Given the frequency of acquisition of each sensor and the typical 10-minutes flight of Eagle, the datasets used within this work comprise around 18 Gigabytes of frames from the camera and 14 Megabytes of measurements from the RADAR.

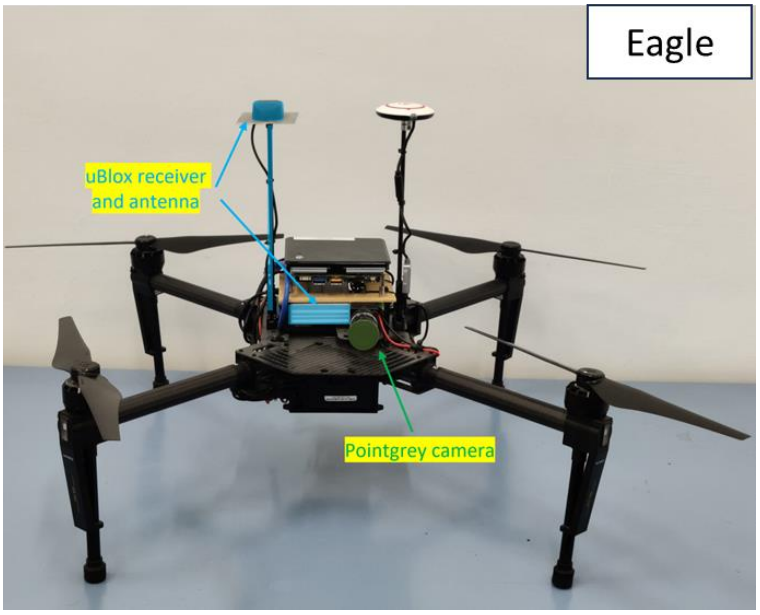

Figure 4.1 sUAV used during flight tests (Eagle) and its constitutive components.

4.2 ALIGNMENT OF SENSORS

The temporal and spatial alignment of sensors is crucial for multi-sensor architectures as it enables the comparison of performance (when different devices are analysed) as well as the fusion of data (when fused solutions are designed). During the performed flight tests, alignment in the time domain is achieved by exploiting a common temporal reference based on GNSS information. The attitude determination of each sensor yields the spatial alignment of their data with respect to a common North-East-Down (NED) reference frame. In this work, attitude determination is performed by exploiting the Quaternion ESTimation (QUEST) algorithm [107].

4.2.1 Temporal alignment of sensors

To achieve temporal alignment, the ground station time (CPU time) of each raw sensor data is saved, yielding to the availability of $t_{CPU,gnss}$, $t_{CPU,rad}$ and $t_{CPU,cam}$ for GNSS messages, RADAR detections and image captures, respectively. While the CPU time-tag could potentially already be used for data synchronization, it would not be sufficient in cases where other sensing devices connected to different computers, e.g., sensors onboard the UAV, need to be considered. To address this

issue, the GNSS time can be exploited as a "universal" temporal reference for all sensors. Thus, the temporal alignment of sensors can be achieved by projecting CPU time-tags of the ground sensors on the GNSS time scale. Specifically, this is achieved by exploiting the ground receiver GNSS time-tags, which can be extracted from its raw messages, and by performing interpolation with CPU times.

4.2.2 Attitude determination

The QUEST algorithm, typically applied for spacecraft attitude determination, can be used to determine the quaternion, or sequence of Euler angles, which parametrizes the attitude of a sensor-bound reference frame with respect to the NED one. Given a unit vector within a reference frame, say $\mathbf{v}=\mathbf{v}^a$, and its corresponding observation within a second reference frame, say $\mathbf{w}=\mathbf{v}^b$, the algorithm directly estimates the rotation matrix from a to b (M_a^b, which verifies $\mathrm{M}\mathbf{v}=\mathbf{w}$) by minimizing the loss function expressed in Eq. (4.1). Here, a_i are a set of non-negative weights.

$$\frac{1}{2}\sum_{i=1}^{n} a_i \left|\mathbf{w}_i - \mathrm{M}\mathbf{v}_i\right|^2 \tag{4.1}$$

In the case under analysis, two different procedures need to be applied to retrieve the matrices from RADAR Reference Frame (RRF) to NED, i.e., $\mathrm{M}_r^n = \left(\mathrm{M}_n^r\right)^{\mathrm{T}}$, and from Camera Reference Frame (CRF) to NED, i.e., $\mathrm{M}_c^n = \left(\mathrm{M}_n^c\right)^{\mathrm{T}}$. In both, $^{\mathrm{T}}$ is used to identify the transpose operator. Attitude angles (heading γ, pitch β and roll φ), defined as the 3-2-1-sequence of Euler angles associated to such matrices, can then be estimated. For the sake of completeness Eq. (4.2) shows the relationship between the rotation matrix M_c^n and the attitude angles (using subscript "c" to indicate camera attitude angles). The same can be written for M_r^n with RADAR attitude angles.

$$
\begin{gathered}
\mathrm{M}_{\mathrm{n}}^{\mathrm{c}}=\mathrm{M}_{\alpha_c}\mathrm{M}_{\beta_c}\mathrm{M}_{\gamma_c} \\
\mathrm{M}_{\alpha_c}=\begin{bmatrix} 1 & 0 & 0 \\ 0 & \cos(\alpha_c) & \sin(\alpha_c) \\ 0 & -\sin(\alpha_c) & \cos(\alpha_c) \end{bmatrix}; \\
M_{\beta_c}=\begin{bmatrix} \cos(\beta_c) & 0 & -\sin(\beta_c) \\ 0 & 1 & 0 \\ \sin(\beta_c) & 0 & \cos(\beta_c) \end{bmatrix}; M_{\gamma_c}=\begin{bmatrix} \cos(\gamma_c) & \sin(\gamma_c) & 0 \\ -\sin(\gamma_c) & \cos(\gamma_c) & 0 \\ 0 & 0 & 1 \end{bmatrix}
\end{gathered} \tag{4.2}
$$

The procedures to estimate the attitude angles are schematically presented in Figure 4.2. The set of observations to be used in each QUEST block is represented by the unit vectors which define the direction of a target of opportunity (adequately chosen for the procedure) with respect to the considered sensor. Thus, the LOS between the sensors and the target is computed either in CRF or RRF, for the camera and RADAR procedure, respectively, while the CDGNSS measurements can be exploited to build the respective observations in NED. The target must be easily and accurately distinguished among the measurements collected by the different sensors. Following this concept, the flying UAV, Eagle in both datasets, can be chosen as target of opportunity since its position in the NED frame is precisely known in terms of the CDGNSS benchmark and its camera and RADAR-retrieved measurements can also be accurately extracted using a supervised approach.

The number of observations which can be used for the QUEST procedure is theoretically unlimited. However, the outcome of the procedure is strongly dependent on the quality and spatial diversity of the deployed measurements. Therefore, as a rule of thumb, data corresponding to fast manoeuvres of the UAV and to short-distance conditions are typically discarded to account for the CDGNSS data latency and improve the exploited unit vectors accuracy, respectively. Therefore, sensors measurements collected when the target is too close (below 100 meters from the ground setup) are discarded. Instead, measurements corresponding to fast manoeuvres can be identified by estimating the azimuth and elevation rates by means of numerical derivation of the available CDGNSS-based relative positioning information. Thus, measurements are discarded if such rates appear to be too high (greater than 1.5 °/s). To improve the accuracy of the solution, the baseline between each sensor (especially between the camera and RADAR with respect to the GNSS

receiver) must also be considered, though the longest baseline (between camera and GNSS receiver) is of about 40 cm.

LOS in the CRF can be computed by manually extracting the exact location of the target, e.g., Eagle, on a series of camera-retrieved frames which respect the aforementioned conditions. Then, pixel coordinates can be transformed in angular estimates by exploiting the knowledge of the camera intrinsic parameters. On the other hand, LOS in RRF are not as immediate to be retrieved as detections belonging to Eagle must be accurately separated from others (clutter, noise, other detected objects) to avoid spoiling the final solution. Therefore, a filtering and centroiding procedure is applied to remove clutter arising from ground echoes and cluster the measurements which likely belong to the same object. This strategy is further detailed in section 5.3. However, the procedure is not free from the presence of residual unwanted detections which could cause errors in the estimation of M_r^n. Thus, an additional condition is applied within the RADAR QUEST block as to only exploit detections which show an error in range, i.e., difference with respect to the CDGNSS-estimated one, smaller than 4 meters.

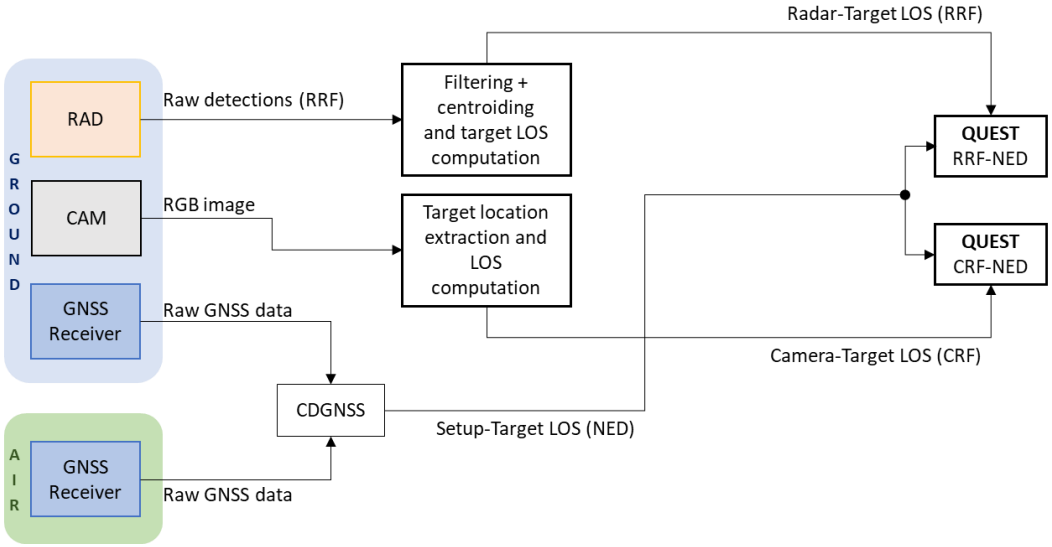

Figure 4.2 Scheme of the attitude determination procedure for RADAR and camera exploiting QUEST.

4.3 FLIGHT SCENARIOS

4.3.1 Dataset 1

Snapshots from experimental tests yielding to dataset 1 are shown in Figure 4.3, where the ground-based sensors are depicted, and Figure 4.4, where Eagle is

captured during flight. The setting for RADAR acquisition were adjusted based on the considered scenario. Thus, the horizontal FOV was set to cover the whole possible extension (az_{min}=-58°, az_{max}=58°), while the vertical one was adjusted as to reduce ground echoes (el_{min}=-4°, el_{max}=36°). The imposed angular separation between the RADAR beams was set to Δaz=4° and Δel=6°. This led to a time needed to cover a single FOV of $\Delta T_{FOVscan}$=1.77 s.

The flight trajectory followed by Eagle, as retrieved with the CDGNSS benchmark, and the location of the sensing setup are shown on a satellite map on the left in Figure 4.5. The flight lasted around 10 minutes and was characterized by a sequence of approaching maneuvers, i.e., encounters, emulating near-collision conditions with the ground setup.

Figure 4.3 Experimental setup during tests for dataset 1: RADAR, camera and GNSS antenna. Zoom over RADAR and camera provided on the right.

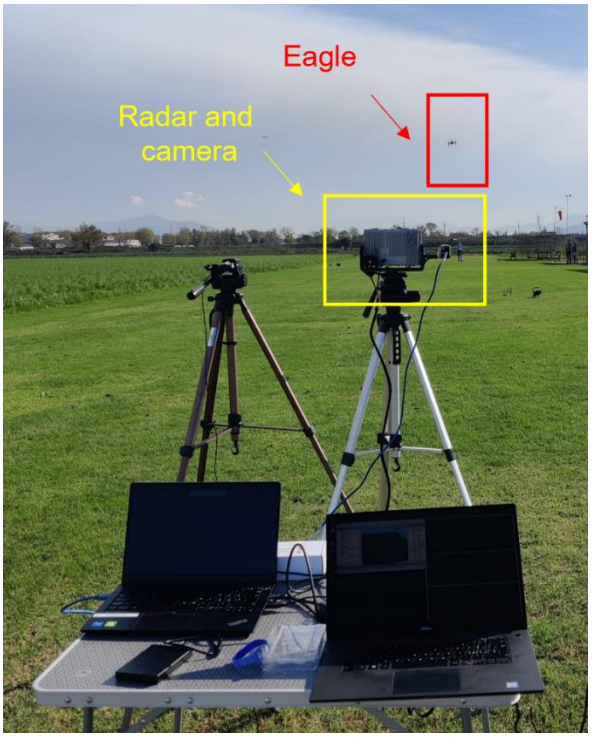

Figure 4.4 Snapshot from flight tests showing Eagle during flight (red rectangle) as captured from behind the sensing setup. Dataset 1.

These maneuvers are typically characterized by steep decreases in range and increases in elevation which prove the advance of Eagle with respect to the setup. Two of these encounters, labeled as “encounter 1” and “encounter 2”, are highlighted in the CDGNSS-based benchmark reported on the right in Figure 4.5 showing range, azimuth and elevation of Eagle with respect to the NED frame centered at the location of the sensing architecture (North and East directions shown in yellow on the left in Figure 4.5). For the sake of clarity, it has to be considered that the azimuth in NED is defined as the angle measured from North towards East, while the elevation is defined as the angle measured from the North-East plane towards the negative Down direction.

Both encounters have similar characteristics with a duration of about 20 seconds and a variation of about 5° both in azimuth and elevation (starting from initial values of 135° and 6° for azimuth and elevation, respectively). As far as variations in range are concerned, during encounter 1 a higher maximum range (about 160 m) is verified at the beginning of the approach. This is lowered down to about 110 m in the case of encounter 2. The two encounters highlighted are used for

preliminary assessment of standalone RADAR and visual sensing strategies (Chapter 5 of this manuscript).

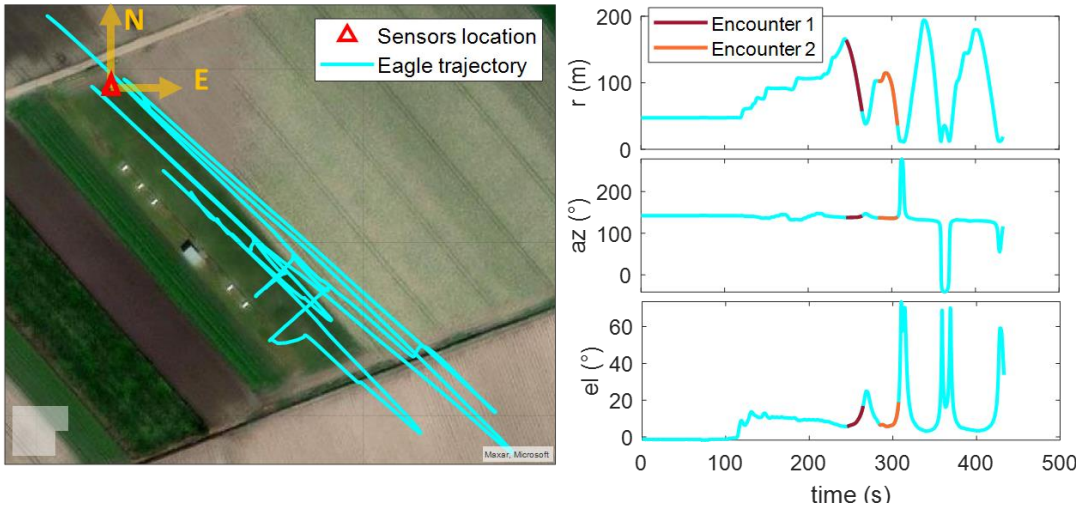

Figure 4.5 Eagle trajectory. Left: trajectory shown on a satellite map reporting location of sensor and definition of North (N) and East (E) directions. Right: trajectory variation in time in terms of range, azimuth and elevation. Encounters considered for the analysis are highlighted with different colours. Dataset 1.

The application of the QUEST algorithm on this dataset results in the retrieval of the attitude angles listed in Table 4.3. For the sake of clarity of the results' interpretation, it has to be noted that both CRF and RRF follow a Forward-Right-Down convention.

Table 4.3 Results of the QUEST procedure on RADAR and camera for dataset 1.

	γ (°)	β (°)	α (°)
RADAR	143.5	0.59	4.17
Camera	136.5	2.97	1.34

4.3.2 Dataset 2

For dataset 2, a different flight location was chosen. This enabled the execution of tests tailored for the evaluation of the detection range of the sensing architecture, especially in the RADAR case. For the latter, in fact, the maximum range capability, as per data sheet, can easily reach the kilometre level for a sUAV.

Snapshots from the flight tests performed for the generation of dataset 2 are shown in Figure 4.6 where both the ground setup and Eagle are imaged.

Figure 4.6 Snapshot from flight tests showing Eagle during flight (red rectangle) as captured from behind the sensing setup. Eagle is also shown during flight on the right. Dataset 2.

Both flight fields used for datasets 1 and 2 have similar characteristics, with low density of obstacles potentially obstructing the FOV of the sensors. Therefore, the same RADAR settings used for dataset 1 were also applied in this case as the only effect to be mitigated is represented by ground echoes. In this case, two different flights of Eagle were performed and used at analyses level for the proposed sensing strategies. Once again, these flights, of 10-minutes each, were characterized by sequences during which Eagle was manually piloted to perform inbound trajectories towards the ground setup. The CDGNSS benchmark is once again shown both on a satellite map, highlighting the trajectory of Eagle during the whole flights, as well as in terms of the time variation of range, azimuth and elevation. These are depicted in Figure 4.7 for flight 1 and Figure 4.8 for flight 2, respectively. The encounters performed during these flights are mostly used to assess the performance of different RADAR/visual fusion solutions (Chapter 6 of the manuscript) where the distances reached, slightly above 500 meters, can represent a more challenging sensing condition than those of dataset 1.

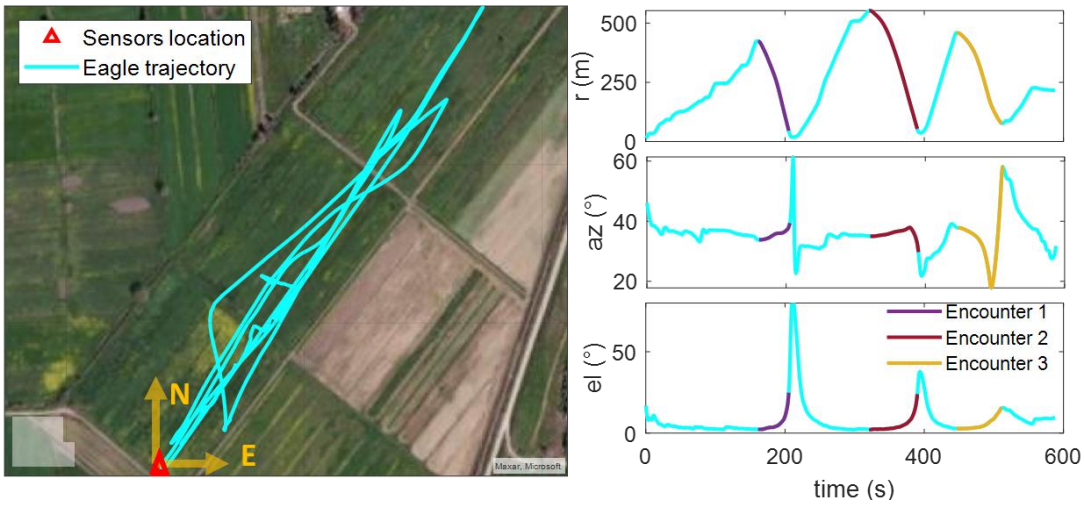

Figure 4.7 Eagle trajectory. Left: trajectory shown on a satellite map reporting location of sensor and definition of North (N) and East (E) directions. Right: trajectory variation in time in terms of range, azimuth and elevation. Encounters considered for the analysis are highlighted with different colours. Flight 1, dataset 2.

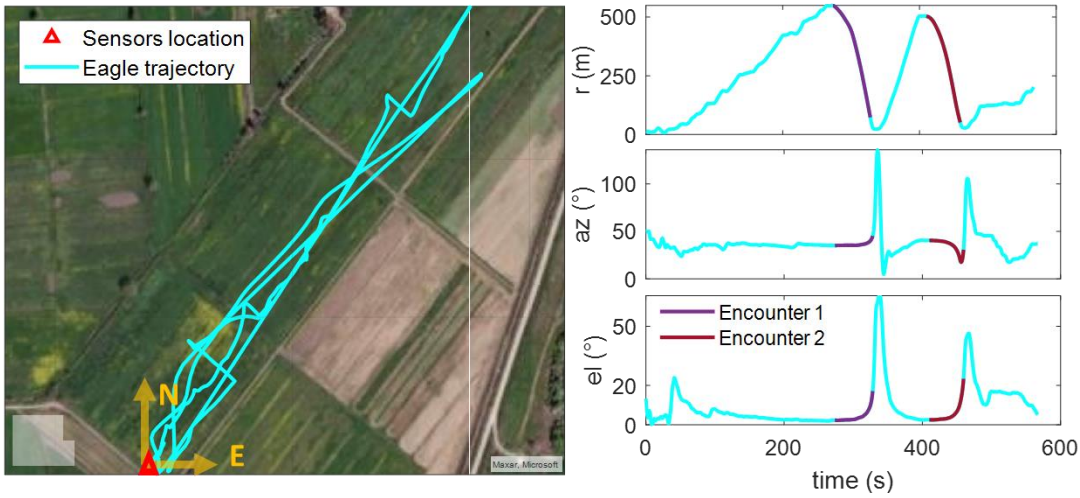

Figure 4.8 Eagle trajectory. Left: trajectory shown on a satellite map reporting location of sensor and definition of North (N) and East (E) directions. Right: trajectory variation in time in terms of range, azimuth and elevation. Encounters considered for the analysis are highlighted with different colours. Flight 2, dataset 2.

Specifics on each encounter as highlighted with different colors in the figures, are reported in Table 4.4 where the first two columns list the flight number and encounter number following the temporal succession shown in the CDGNSS benchmark of the previous figures. Results from the application of the QUEST procedure on dataset 2 are listed in Table 4.5 where the lower heading angles with respect to dataset 1 (Table 4.3) can easily be noticed. The latter result from the orientation of the flight field, whose axis, aligned with the pointing direction of the sensors, is closer to the North direction with respect to dataset 1.

Table 4.4 Characteristics of encounters in dataset 2.

Flight	Encounter	Duration (s)	Range variation (m)	Azimuth variation (°)	Elevation variation (°)
1	1	44.1	[46.2, 422.9]	[33.8, 39.4]	[2.3, 24.9]
1	2	69.1	[53.7, 552.3]	[29.8, 37.9]	[2.2, 23.9]
1	3	64.7	[77.5, 458.8]	[17.9, 58.1]	[2.8, 15.4]
2	1	54.6	[72.7, 548.6]	[35.2, 45.3]	[2.3, 17.1]
2	2	49.5	[51.6, 503.7]	[17.4, 40.5]	[2.5, 23.4]

Table 4.5 Results of the QUEST procedure on RADAR and camera for dataset 2.

	γ (°)	β (°)	α (°)
RADAR	35.8	5	2.3
Camera	36.5	6.5	-0.5

Chapter 5: Standalone Visual-based and RADAR-based Sensing Algorithms

The design of a DAA sensing architecture must account for the execution of different tasks to successfully declare the eventuality of a collision and perform timely avoidance manouvres. Such tasks start with the surveillance of the environment surrounding the own-ship, which can either be equipped with onboard sensors and/or receiving information about the air traffic by communicating with ground stations. A detection phase is then performed to determine the presence of obstacles or aircraft in the proximities. To improve the confidence over the presence of such threats and estimate their kinematics, a tracking phase typically follows. Within a DAA architecture, the main scope of a tracking algorithm is to generate reliable tracks for intruders of interest at a range compatible with safe execution of eventual avoidance manoeuvres, and to provide reliable and accurate estimates relevant to position and velocity of these intruders. Furthermore, this also allows reducing the false alarms, which can arise from the detection of objects whose dynamics does not suggest possible collisions, and increasing the measurement rate with respect to raw sensor data.

In this chapter, the algorithms used for tracking based on the standalone RADAR- and visual-based information are presented. First, an overview of the structure and basic principles is provided in section 5.1, which briefly discusses the Kalman filtering -based tracking process. Then, vertical discussions on the implementation of such process for visual and RADAR tracking are presented in section 5.2 and 5.3, respectively, where details on the measurements used are also provided. In the visual case, different detectors are tested (and furtherly also implemented within the fusion strategies of Chapter 6) based on either feature-based approaches (morphological filtering with adaptive template matching) or appearance-based recognition with Deep Learning (DL). To conclude the discussion, experimental results analysing performance of the tracking algorithms are provided in section 5.4. Specifically, in the first part, preliminary results on the use of the

visual tracking algorithm with DL detector and the RADAR tracking algorithm on dataset 1 are introduced. Then, to test the strategies in more challenging conditions, involving higher ranges, analyses on dataset 2 are also discussed.

5.1 OVERVIEW OF THE TRACKING ALGORITHMS

Tracking is the process of estimating the state of a moving object allowing improvements in the quality (accuracy/reliability) of noise-affected sensors' raw measurements and achieving information not directly available from such measurements. The complexity of a tracking algorithm can be increased in cases where multiple targets move within the surveillance volume and thus need to be reliably tracked. In this case, multi-target tracking needs to be performed. A convenient structural partition of the basic functional elements of a multi-target tracking process is provided in Figure 5.1. The core of the structure is represented by the "Filtering and Prediction" block, where the state estimation cycle is performed. Such cycle comprises prediction phases, during which previous state estimates are used to retrieve the current state estimate (thus performing time updates), and filtering phases, where the current state is filtered (or corrected) based on the availability of external information (measurements). The gating task is responsible for generating "gates" around the predicted state which are used to evaluate the feasibility of exploiting an available measurement for state filtering. This is determined using measurement-to-track association criteria which yield to the assignment of a measurement to a given track and to the execution of different track maintenance steps.

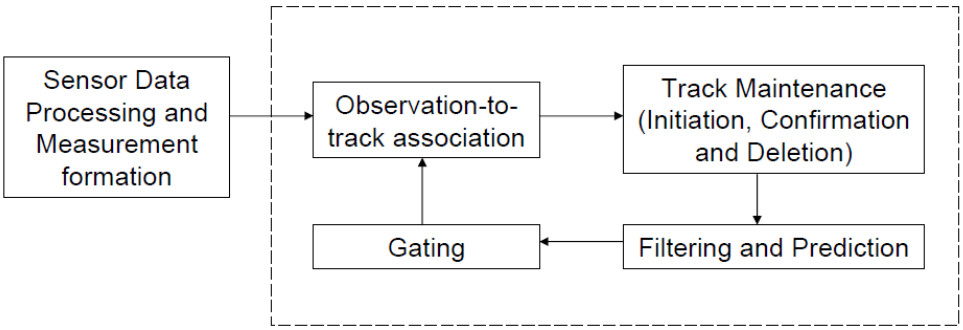

Figure 5.1 Basic functional elements of a multi-target tracking process [108].

From a state estimation point of view, the tracking algorithms exploited in this work are based on linear and Extended Kalman Filters, KF and EKF respectively.

The state estimation operation thus follows the classic prediction-correction scheme [109] which is depicted in its discrete form in Figure 5.2 for a single cycle going from time *k-1* to *k*. In the figure, the symbol ˆ identifies predicted quantities. The scheme assumes that the state of the target evolves with a linear dynamic model represented by a known input and an additive, zero-mean white noise (process noise) with known covariance matrix (Q). Measurements are considered to be a known function of the state (expressed through function *h*) with an additive zero-mean white measurement noise, with covariance expressed in the matrix R.

The process develops following the steps of Figure 5.2. Thus, for each existing track, the state (**x**) is predicted at time instant *k* exploiting the previous estimate at time *k-1* and a state transition matrix (Φ). Associated sensor measurements (**z**) retrieved at time *k* can then be used to perform a correction of the estimated state at the very same time instant. This correction step passes through the computation of the Kalman gain (K) which considers the uncertainty in the exploited measurement and its relationship with the state, expressed within matrix H. A logic similar to the state thread is also used for the state covariance, expressed in matrix form as P. The latter, when predicted, accounts for the uncertainty in the assumed linear velocity dynamics which is parametrized within the process covariance matrix (Q).

In the implementation proposed, both trackers exploit a Nearly Constant Velocity (NCV) model which results from the Singer acceleration model [110] for a filter sampling time (*T*) much larger than the target manouvering time. The state model thus assumes a linear dynamic with either linear (visual case) or non-linear (RADAR case) relationship with the measurements. Thus, on a model level, the only difference between the two implementations lies in the expression of function *h* relating the measurement with the state, e.g., $\mathbf{z}=h(\mathbf{x})$. Its non-linearity in the RADAR case requires linearization and computation of the Jacobian matrix $H=\partial h/\partial \mathbf{x}$ (blue block in Figure 5.2).

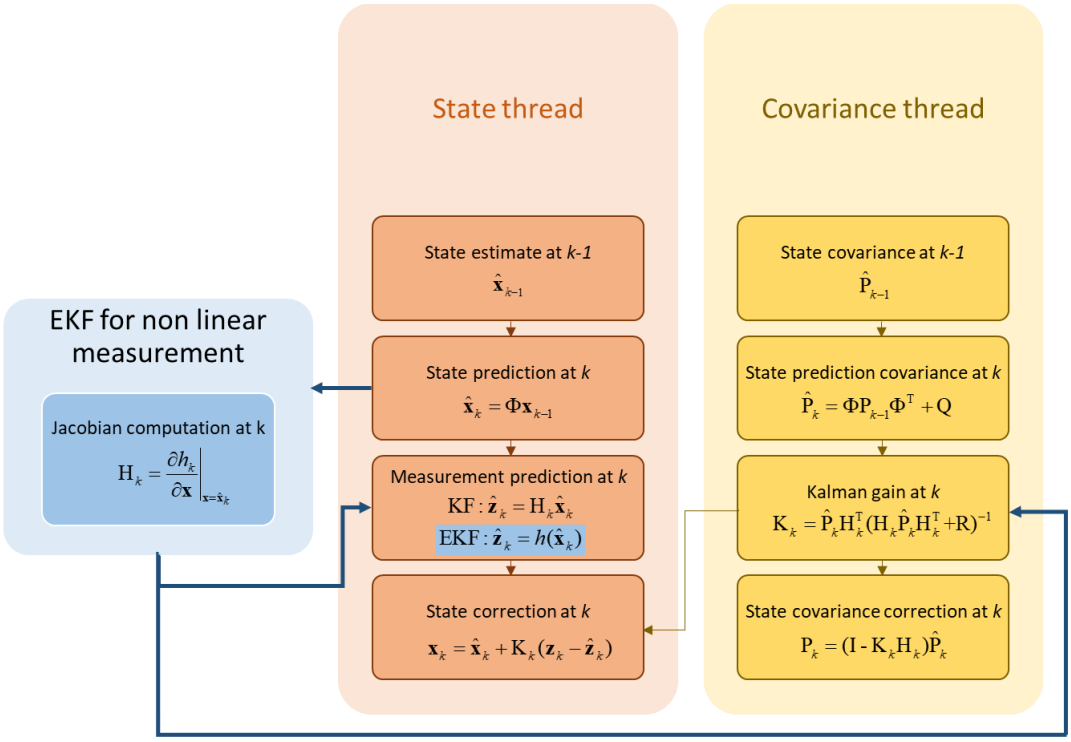

Figure 5.2 Flowchart of the KF and EKF tracking steps during one cycle (time *k*) given measurement availability.

Both the RADAR and visual tracking algorithmic architectures share similar structure and working principle, considering different track status defined as single un-associated detections ("one plot" tracks, following typical terminology adopted in RADAR tracking), tentative tracks (in need of further confirmation), and firm tracks, which are deemed reliable enough to provide intruder declaration and support conflict detection and eventual avoidance manoeuvring logics. This is schematically shown in the diagram of Figure 5.3. Following the principles of Figure 5.1, a measurement retrieved at a given time is sequentially checked for association with the firm/tentative/one plot tracks available at the current time instant and numbered with n_{FT} and n_{TT} in the case of firm and tentative tracks, respectively. In the visual tracker case, the logic to associate detections and tracks depends on the type of track that is considered (i.e., firm or tentative), exploiting the full filtering and prediction pipeline only for firm tracking. In the RADAR case, the logic is similar at all levels and exploits probabilistic data association methods [108] based on the Mahalanobis distances. In lack of association, tracks are updated using prediction-only state estimations. In both RADAR and visual trackers, a track deletion mechanism, to be performed when no successful association is obtained for a reasonable time, is also implemented to avoid tracking error divergences. Association and track deletion

criteria vary depending on the considered sensor and will therefore be detailed in the following subsections.

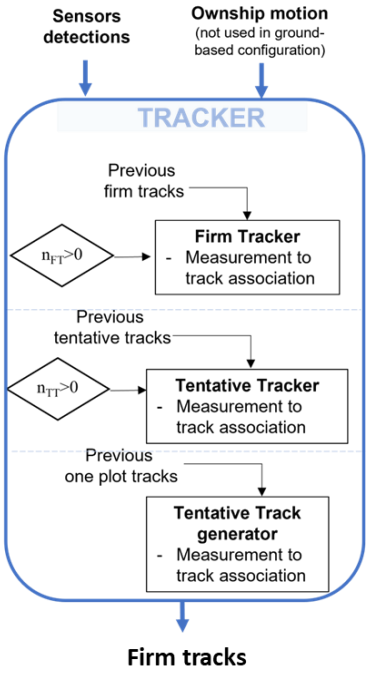

Figure 5.3 Logic followed by the visual-based and RADAR-based trackers.

For the sake of completeness, it has to be noticed that both designed algorithms work on measurements expressed in the North-East-Down (NED) reference frame, while each sensor measurement is, intuitively, retrieved in its own coordinate system, namely Camera Reference Frame (CRF, identified with apex "*c*" in the following) and RADAR Reference Frame (RRF, identified with apex "*r*" in the following) in the visual and RADAR case, respectively. Consequently, the knowledge of attitude angles of both sensors with respect to the NED reference frame is needed. If the sensing architecture is mounted onboard the own-ship, the attitude information varies dynamically and can be derived from the navigation system. In the case of ground-fixed sensors, the attitude is constant and can be estimated exploiting CDGNSS measurements as previously discussed in section 4.2. It is worth mentioning that, though tested in ground-to-air scenarios, the strategies proposed in this manuscript can be adapted to account for airborne sensors installation by incorporating the information on the own-ship attitude, as also highlighted in Figure 5.3.

5.2 VISUAL-BASED SENSING ARCHITECTURE

5.2.1 Visual measurements

The visual-based tracking algorithm uses as inputs detections provided by different detectors which extract a set of candidate targets on the image plane, identified by pixel coordinates (x_{pix},y_{pix}). From this information, angular estimates in CRF can be derived by exploiting the knowledge of the camera intrinsic parameters. The latter can be estimated by exploiting calibration procedures and toolboxes such as [111]. To build the angular estimates, pixel coordinates are normalized as shown in Eq. (5.1), where (c_x,c_y) are the coordinates of the camera principal point.

$$x_{pix,n} = \frac{x_{pix} - c_x}{f};\ \ y_{pix,n} = \frac{y_{pix} - c_y}{f} \tag{5.1}$$

Then, radial and tangential distortions are corrected yielding to normalized, undistorted pixel coordinates (x_n,y_n) which can be used to compute the azimuth (az^c) and elevation (el^c) angles in CRF as shown in Eq. (5.2).

$$az^c = \text{atan}(x_n);\quad el^c = \text{atan}(-y_n \cos(az)) \tag{5.2}$$

The angular information retrieved with these steps is then rotated in the local North-East-Down (NED) reference frame, centred at the camera location, by exploiting the rotation matrix from CRF to NED (M_c^n).

5.2.2 Visual tracking

In the cases considered to test the visual sensing architecture, the target flies in open sky and the sensing setup is located on the ground. Therefore, only AH visual detections of sUAVs are looked for by the detectors in the image plane. The horizon line which separates the terrain and sky regions on the image plane can be computed by accounting for the camera attitude angles in the local NED frame as shown in [112]. In the latter, the computation is performed for an onboard camera accounting for the own-ship attitude and the camera mounting parameters, the method is therefore simplified in the case considered for these analyses, where ground-based fixed cameras (with constant attitude angles) are considered.

The pixel coordinates extracted by the detectors are then transformed into angular information which is used to build two different measurement vectors

$\mathbf{z_{az}}$=[*az*] and $\mathbf{z_{el}}$=[*el*] for azimuth and elevation, respectively. The horizontal and vertical dynamics of the tracked objects are, in fact, decoupled and two independent linear KFs which exploit the state vectors $\mathbf{x_{az}}$=[*az*,*aż*] and $\mathbf{x_{el}}$=[*el*,*el̇*] are used. In the latter, azimuth and elevation rates are represented by the symbols *aż* and *el̇*. Therefore, all the matrices which define the KF model, described in the previous section, are doubled for application to the two state vectors. Specifically, Eq. (5.3) lists the expression of the matrices used by the two trackers. Here, *T* is the tracker sampling time and the subscript "*x*" is used to identify either azimuth or elevation fields as matrices are defined equally for both cases.

$$\begin{aligned} \Phi_x &= \begin{bmatrix} 1 & T \\ 0 & 1 \end{bmatrix} \\ \mathrm{Q_x} &= q_x \begin{bmatrix} \frac{T^3}{3} & \frac{T^2}{2} \\ \frac{T^2}{2} & T \end{bmatrix} \\ \mathrm{R}_x &= \sigma_x^2 \\ \mathrm{H}_x &= \begin{bmatrix} 1 & 0 \end{bmatrix} \end{aligned} \tag{5.3}$$

However, depending on which state vector, hence which measurement, is being considered the values of q_x and σ_x can vary. The former scale factors can be chosen according to the expected velocity of sUAVs within the time *T*, while the latter represent the quality of azimuth and elevation measurements.

As far as track deletion is concerned, firm, tentative and one plot tracks are preserved in the absence of associated measurements, for a maximum number of tracking steps equal to N_{maxFT} , N_{maxTT}, N_{maxOT}, respectively.

The discussion on the visual tracking solutions is divided in two separate subsections where the approaches, based on the two tested detectors, are presented in greater details.

5.2.2.1 Deep learning approach

Within this approach a CNN comprising You Only Look Once (YOLO) v2 detection layers [101], trained to search for objects above the horizon line, is used. The data for training is built from experimental flight tests involving the same sUAV

described in section 4.1, during flights different from those used for the analyses performed in this manuscript. Further details can be found in [62]. The tracking algorithm, whose flow diagram is schematically presented in Figure 5.4, also exploits the confidence score output by the detector; detections with a score greater than a threshold (S) are considered reliable enough for use during tracking. Therefore, one-plot tracks are constituted of all measurements respecting this condition. Measurement-to-track association for tentative track generation are evaluated based on gates centred on the previous one-plot track expressed with the Euclidean distance shown in Eq. (5.4). Here, the pixel coordinates are (u,v) and the subscript refers to two subsequent time steps during tracking.

$$d_{track} = \sqrt{\left(u_i - u_{i-1}\right)^2 + \left(v_i - v_{i-1}\right)^2} \tag{5.4}$$

The detection closest to the track, according to such distance, is considered for association which is deemed successful if $d_{track}<\tau_{tr,gen}$. The latter threshold is chosen based on the camera IFOV and acts as to discard detections corresponding to targets with very fast angular motion on the image plane, thus likely not representing a collision threat. This approach is also used both in Tentative and Firm Tracker blocks where the threshold can also be set differently to design more or less strict association requirements. Specifically, since firm tracking is the only step during which tracks are predicted and corrected using Kalman filtering, association is verified using track prediction. Once a firm track is generated, the Kalman filtering process on the state estimates ($\mathbf{x_{az}}$ and $\mathbf{x_{el}}$) is performed.

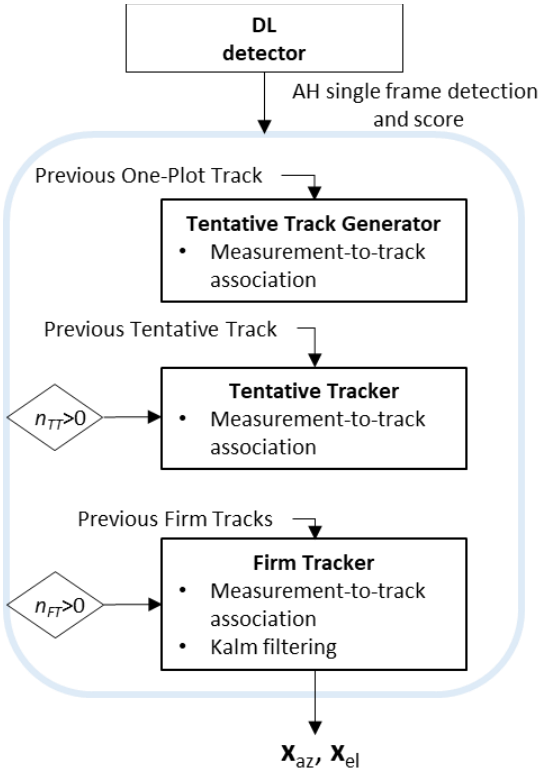

Figure 5.4 Flow diagram of visual-based tracking algorithm exploiting DL detector.

5.2.2.2 Morphological filtering and adaptive template matching approach

The detection process used in this case, comprises both top and bottom hat morphological filtering along with local image analysis on frames retrieved by the visual camera, as discussed in [112] and reported as MF detector in the flow diagram of Figure 5.5. Specifically, a square structuring element is used for the application of the two filters. Then, a sequence of global and local thresholding is applied to isolate the detection of sUAVs of interest. In the first, the removal of the background (AH, sky region) is targeted, thus pixels are isolated if their intensity is higher than a threshold imposed on the pixel intensities in the filtered image. These isolated pixels constitute the regions where local thresholding is then applied to refine the achieved detections.

The detections retrieved by the MF detector are used to generate tentative and firm tracks by exploiting the association criterion on Euclidean distance expressed in Eq. (5.4). At firm tracking stage, detections for state filtering are no longer provided by the MF operator (which will indeed continue feeding the tentative tracker looking for other objects of interest), but by means of template matching. Specifically, the correlation criteria [113] based on intensity of pixels is applied to compare a template

with a search window, built on the current image and centred at the track prediction. The pixel corresponding to the correlation peak (if greater than a threshold T_{peak}) is identified as a possible candidate to be passed to the firm tracker. Once a track is confirmed, the first template is generated from the current image as a rectangular bounding box of $N_{x,temp} \times N_{y,temp}$ pixels centred at the associated detection. The template dimensions are chosen by considering that the observed object is typically unknown, thus, to account for different classes of UAVs, a reasonable choice is that of setting the template length to be greater than its height. However, during the intruder motion, its size on the camera frames can strongly change, varying from few pixels, in long-range condition, to several tens of pixels in close range conditions. Therefore, a fixed template would cause a quick loss of the target and a strong divergence in the firm tracking error. To avoid this unwanted effect, a template update criterion is implemented to generate new templates whenever the number of pixels occupied by the target on the image plane (N_{tgt}) changes significantly. Three regions can then be designed based on N_{tgt}, thus accounting for the target transition between far ($N_{tgt} \leq N_{far}$), medium ($N_{far} < N_{tgt} \leq N_{med}$) and close-range regions ($N_{med} < N_{tgt} \leq N_{close}$). At each new region entrance, the template is updated and its dimensions are changed in relation to the new length of the target on the image plane, also expressed in pixel terms (L_{tgt}), considered as the target dimension which is expected to more likely show a significant variation. At each firm tracking step, the values of N_{tgt} and L_{tgt} are estimated by applying edge detection techniques on a smaller, halved in size, search window. If a template update is found to be needed, its length is changed (increased if approaching encounters are considered) to $L_{tgt}/2$ pixels, and its height is also changed as to always keep the same length-to-height ratio, i.e., $N_{x,temp}/N_{y,temp}$.

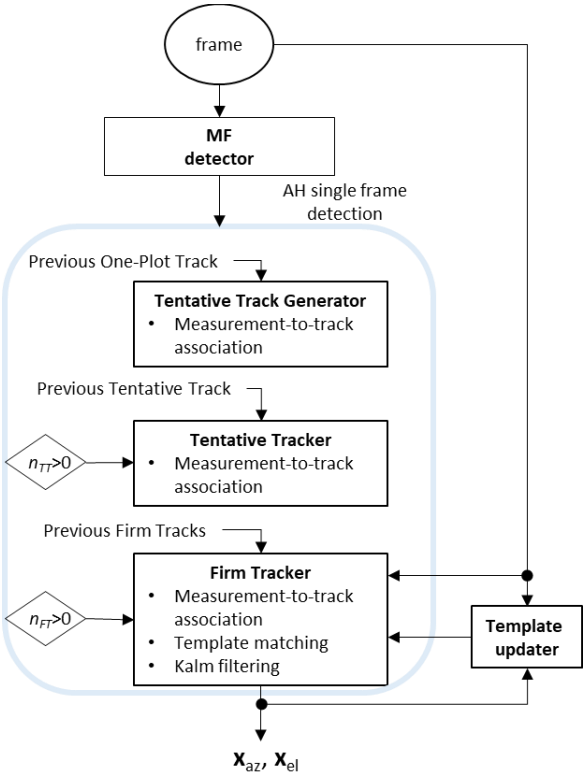

Figure 5.5 Flow diagram of visual-based tracking algorithm exploiting MF-TM approach.

5.3 RADAR-BASED SENSING ARCHITECTURE

5.3.1 RADAR measurements

The operational principle of the RADAR exploited during the research activities was previously introduced in section 4.1 and is graphically represented on the left in Figure 5.6, where the beams are depicted as orange ellipses. After the completion of a single FOV scan, the pattern is repeated, thus different RADAR frames are generated. A graphic illustration of the azimuth-elevation pattern within a single RADAR frame is given on the right in Figure 5.6 where the angular distance between two consecutive beams in the horizontal (Δaz) and vertical (Δel) directions are also highlighted.

Due to the device sensitivity to clutter and noise, pre-processing steps are applied on the measurements. Specifically, as an initial step, Doppler-based filtering is applied to remove all measurements having $\dot{r}<\dot{r}_{th,low}$, thus plausibly arising from ground and static objects. Once filtered, measurements undergo a centroiding procedure which is used to furtherly ease the handling of RADAR data, thus also easing the following tracking process. The centroiding step is based on the idea that the resolution of the device, especially in angular terms, can promote the generation

of different measurements of the same object in a single frame. Thus, at each frame, clusters of detections which appear to be adjacent in azimuth or elevation and have comparable ranges are identified and merged. In more practical terms, these clusters verify differences in azimuth, elevation and range which are smaller or equal to the values of Δaz, Δel and Δr, respectively. The latter threshold can be set equal or slightly greater than the range resolution of the RADAR depending on the expected sensor performance. If identified, a cluster of detections is merged by computing an average of its corresponding measurements. Specifically, the elevation measurement, is weighted over the power scattered back by the detected target as to reduce the impact of side lobe detections.

At the end of the filtering and centroiding process, measurements are rotated in the NED frame centred at the RADAR location by exploiting the rotation matrix from RRF to NED (M_r^n).

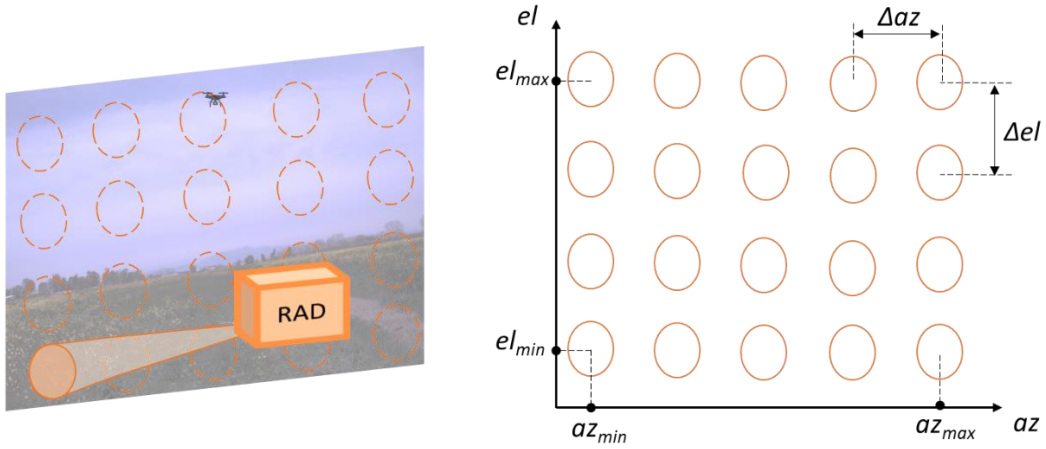

Figure 5.6 Left: Graphic illustration of scanning pattern of the RADAR (RAD). Generated beams are depicted as orange ellipses. Beam observed at given time instant is highlighted in orange. Right: Graphic illustration of a single RADAR frame in the azimuth and elevation field.

5.3.2 RADAR tracking

The RADAR-based tracker exploits a cartesian state vector which contains the relative position (x,y,z) and velocity ($\dot{x}$,$\dot{y}$,$\dot{z}$) of targets with respect to the RADAR location in NED. This yields a definition of the state vector as $\mathbf{x}$=[x,y,z,$\dot{x}$,$\dot{y}$,$\dot{z}$]. The measurement vector is expressed as $\mathbf{z}$=[r,az,el,$\dot{r}$] and contains filtered and centroided measurements, instead. Conversely to the visual-only case, the pipeline foresees the application of prediction-correction schemes at each step, thus propagating all types of tracks from one-plot to firm ones. This choice depends on the frequency with

which valid measurements are retrieved, thus being usable for tracking. Such frequency is much lower with respect to the visual case, especially after the application of filtering and centroiding procedures. The difference between the predicted and the actual measurement, normalized with respect to the uncertainty in both quantities, is used for evaluation of the measurement-to-track association. Such difference can be formulated in terms of the Mahalanobis distance shown in Eq. (5.5).

$$\xi = (\mathbf{z} - \hat{\mathbf{z}})\,[\mathrm{H}\hat{\mathrm{P}}\mathrm{H}^{\mathrm{T}} + \mathrm{R}]^{-1}\,(\mathbf{z} - \hat{\mathbf{z}})^{\mathrm{T}} \tag{5.5}$$

Association is deemed successful when such difference is smaller than a threshold $\xi_{RAD,th}$. Given the chi-squared distribution of ξ, the threshold can be set accordingly to the chi-squared distribution table for a number of degrees of freedom which is defined by the number of elements contained within the **z** vector [114]. Specifically, for a four-elements vector, as in the RADAR case, $\xi_{RAD,th}$ can be set to 13.28, which corresponds to a 0.99 probability of preserving a valid measurement.

Due to the non-linearity of the measurement vector, the matrix H utilized throughout the EKF, needs to be computed by linearization of the relationship between measurement and state. This can be written in terms of the components of vector $\mathbf{h}(\mathbf{x})=[h_1,h_2,h_3,h_4]$ which are formulated in Eq. (5.6). State transition matrix is defined in Eq. (5.7), where I is the identical 3 x 3 matrix, O is a 3 x 3 matrix of null elements and T is the filter sampling time. Process noise matrix is defined in Eq. (5.8) and measurement covariance matrix, with squared covariance of measurements (σ^2) along the diagonal, is defined in Eq. (5.9). In the former, the scale factors, i.e., q_x, q_y, q_z, are tuned in relation to the expected maximum velocity of the tracked object within the interval T.

$$\begin{aligned}
h_1 &= r(\mathbf{x}) = \sqrt{x^2 + y^2 + z^2} \\
h_2 &= az(\mathbf{x}) = tg^{-1}\left(\frac{y}{x}\right) \\
h_3 &= el(\mathbf{x}) = \sin^{-1}\left(\frac{z}{\sqrt{x^2 + y^2 + z^2}}\right) \\
h_4 &= \dot{r}(\mathbf{x}) = \frac{x\dot{x} + y\dot{y} + z\dot{z}}{\sqrt{x^2 + y^2 + z^2}}
\end{aligned} \tag{5.6}$$

$$\Phi = \begin{bmatrix} \mathrm{I} & \Delta\mathrm{T} \\ \mathrm{O} & \mathrm{I} \end{bmatrix}; \Delta\mathrm{T} = T\mathrm{I} \tag{5.7}$$

$$\mathrm{Q} = \begin{bmatrix} \mathrm{Q}_3 & \mathrm{Q}_2 \\ \mathrm{Q}_2 & \mathrm{Q}_1 \end{bmatrix}$$

$$\mathrm{Q}_3 = \begin{bmatrix} q_x \dfrac{T^3}{3} & 0 & 0 \\ 0 & q_y \dfrac{T^3}{3} & 0 \\ 0 & 0 & q_z \dfrac{T^3}{3} \end{bmatrix}; \mathrm{Q}_2 = \begin{bmatrix} q_x \dfrac{T^2}{2} & 0 & 0 \\ 0 & q_y \dfrac{T^2}{2} & 0 \\ 0 & 0 & q_z \dfrac{T^2}{2} \end{bmatrix} \tag{5.8}$$

$$\mathrm{Q}_1 = \begin{bmatrix} q_x T & 0 & 0 \\ 0 & q_y T & 0 \\ 0 & 0 & q_z T \end{bmatrix}$$

$$\mathrm{R} = \begin{bmatrix} \sigma_r^2 & 0 & 0 & 0 \\ 0 & \sigma_{az}^2 & 0 & 0 \\ 0 & 0 & \sigma_{el}^2 & 0 \\ 0 & 0 & 0 & \sigma_{\dot{r}}^2 \end{bmatrix} \tag{5.9}$$

The track deletion criteria adopted in the RADAR-based tracking algorithm are designed to be adherent to the sensor operation. Specifically, the time needed by the RADAR to build a single frame, thus completing a whole FOV scan ($\Delta T_{FOVscan}$), is taken into account. Tracks are thus maintained in prediction-only condition, i.e., in absence of successful associations, when the time elapsed from the last correction of a given track is $N_{maxFTscans}$, $N_{maxTTscans}$ and $N_{maxOPTscans}$ times greater than $\Delta T_{FOVscan}$ for firm, tentative and one plot tracks, respectively.

5.4 RADAR AND VISUAL TRACKING RESULTS

5.4.1 Results on dataset 1

In this section, preliminary results on RADAR-based and visual-based tracking results are presented. The results are achieved by applying the methodologies discussed in the previous sections to the experimental data contained within dataset 1. Specifically, first analyses for the visual-based tracker are provided by applying the DL-based approach. For the sake of clarity and compactness, in the following

discussions firm, tentative and one-plot tracks will be referred to as FT, TT and OT, respectively.

5.4.1.1 RADAR detections and centroiding

The RADAR acquisition during the flights of dataset 1 resulted in the generation of 81459 beams and the collection of about 480 detections per second. The previously described filtering and centroiding steps are thus used to only extract detections corresponding to targets of interest. Specifically, filtering is carried out with a value of $\dot{r}_{th,low}$=0.9 m/s. An example of the results achieved after measurements filtering and centroiding is shown in Figure 5.7. Here unprocessed range measurements retrieved within the 10 minutes of acquisition are reported as dots showing multiple colors. Each color represents the measurements retrieved in a single beam. Instead, the green dots depict all range measurements achieved after the application of the proposed strategy. These are labeled as "Eagle detections" as they are mostly related to the flying UAV with a minor presence of unremoved noise/clutter measurements. A drastic reduction in the total number of measurements, dropped down to 300, is achieved at the end of the procedure.

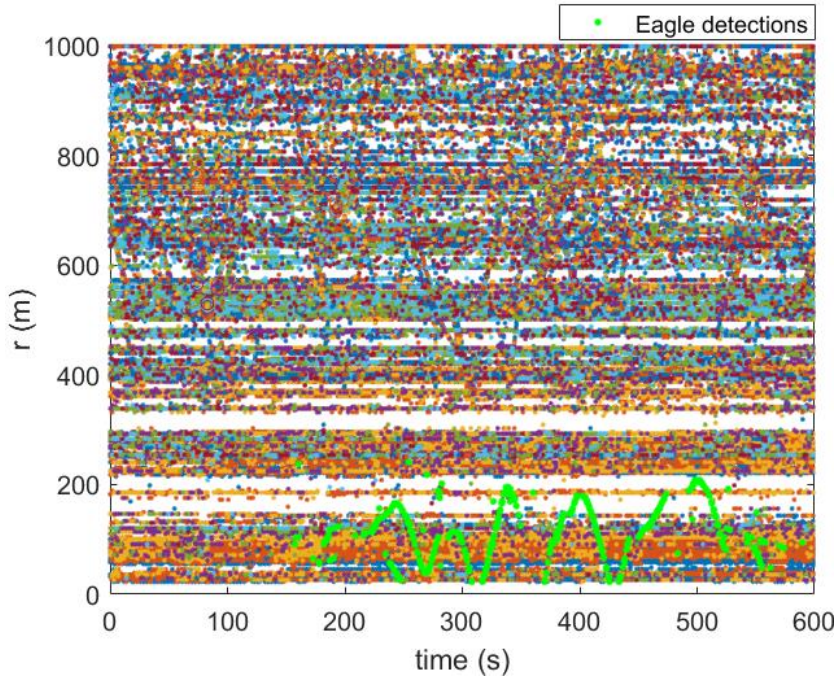

Figure 5.7 RADAR range measurements before (multi-colored dots) and after (green dots) the application of the filtering and centroiding procedure.

5.4.1.2 Tracking results

The trackers exploit a sampling time T=0.1 s and account for the uncertainty in RADAR and camera measurements which are reported in Table 5.1. The latter values were selected based on an a-priori assessment of the accuracy of sensors, carried out exploiting the available CDGNSS benchmark. Visual measurements extracted by the DL detector must verify a confidence score greater than the threshold S=0.4 in order to be used during tracking, while the dimensions of the gate for their association is $\tau_{tr,gen}$=5 pixels. As far as track deletion logic is concerned, the values of N_{maxOT}=1, N_{maxTT}=2 and N_{maxFT}=20 are chosen for the visual tracker, while $N_{maxFTscan}$=4, $N_{maxTTscan}$=3 and $N_{maxOTscan}$=1 are used by the RADAR tracker.

Table 5.1 Uncertainty in RADAR and camera measurements used for tracking.

	$\sigma_{\dot{r}}$ (m/s)	σ_r (m)	σ_{az} (°)	σ_{el} (°)
RADAR	0.9	3	2	6
Camera	-	-	0.2	0.3

Visual tracking results for encounter 1 are shown in Figure 5.8 where the tracker-estimated azimuth, elevation, and their rates are reported in NED. Detections used at firm tracking level (red dots) and resulting firm tracks (red line) are depicted. OT and TT detections are also shown as green circles and black dots, respectively. The tracking results are shown in comparison with the CDGNSS benchmark (blue line). RADAR tracking results on the same encounter are shown in Figure 5.9 with the addition of range and range rate estimates with respect to the visual case. Figure 5.10 depicts the errors of both strategies with respect to the CDGNSS benchmark. Statistics in terms of root mean square (rms) errors are listed in Table 5.2.

From the accuracy perspective, visual tracking performance appears to be satisfactory, as witnessed by the low RMS listed in Table 5.2. Sudden increase in all errors can be noticed in the last part of the encounter (starting at time>260 s) as a consequence of the lack of DL detections, which causes the track to only be predicted before being deleted. However, such performance deterioration can be expected and is to be imputed to the training process of the detector, which is focused at increasing the declaration range, thus naturally being less performant in close range conditions (with larger on-image dimensions of the intruder). Still, the visual algorithm is able to track the intruder until it reaches a distance of 74 m from the camera, below which Eagle detection scores become too small for firm tracking

use. Tracking error statistics for the RADAR case highlight coarser performance with respect to the visual solution in terms of angles and angular rates. As expected from the higher vertical beam width, this is particularly true in the elevation case, however, angular errors RMS are lower than 1°, in azimuth, and lower than 3°, in elevation. Firm track of the intruder is retrieved with a delay of 3 seconds with respect to the encounter start. This is to be imputed to the lack of initial associated measurements. However, once generated, the RADAR-based firm track is able to reliably follow the intruder for the remaining part of the encounter, while estimating range and range rate with errors below 1 m and 1 m/s, respectively.

The performance trends achieved on encounter 1 are also verified during encounter 2. The error statistics relative to this case are listed in Table 5.3 showing an overall increase in RMS. This is due to a lower number of RADAR detections with respect to encounter 1. In the visual case, loss of detections also occurs when approaching the end of the encounter. Still, the visual tracker confirms errors below 1° and 1 °/s in angles and angular rates, respectively.

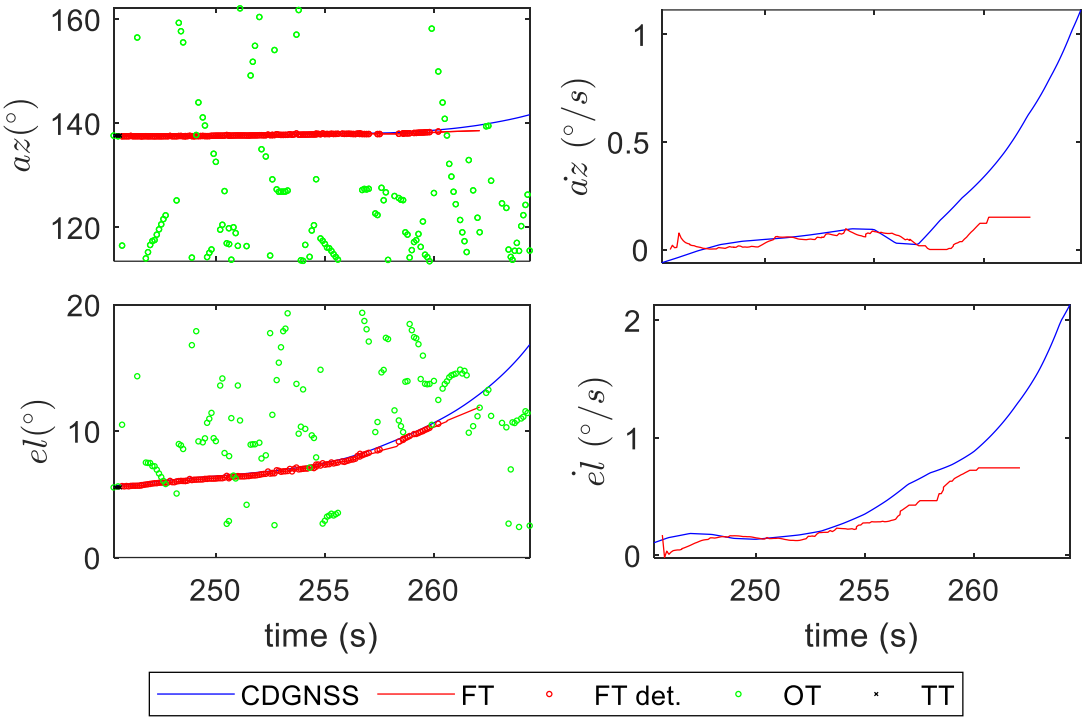

Figure 5.8 Dataset 1 - Encounter 1. Results from visual tracking compared with benchmark.

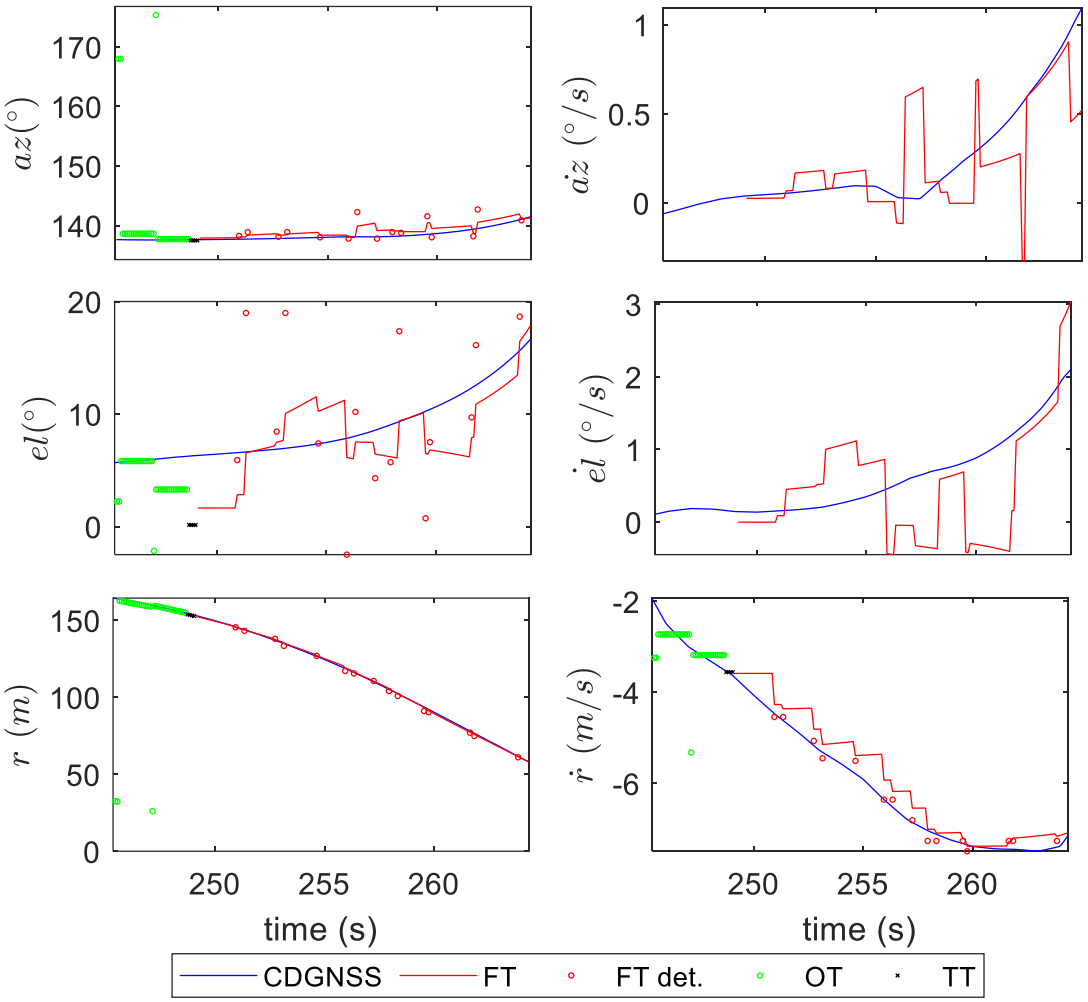

Figure 5.9 Dataset 1 - Encounter 1. Results from RADAR tracking compared with benchmark.

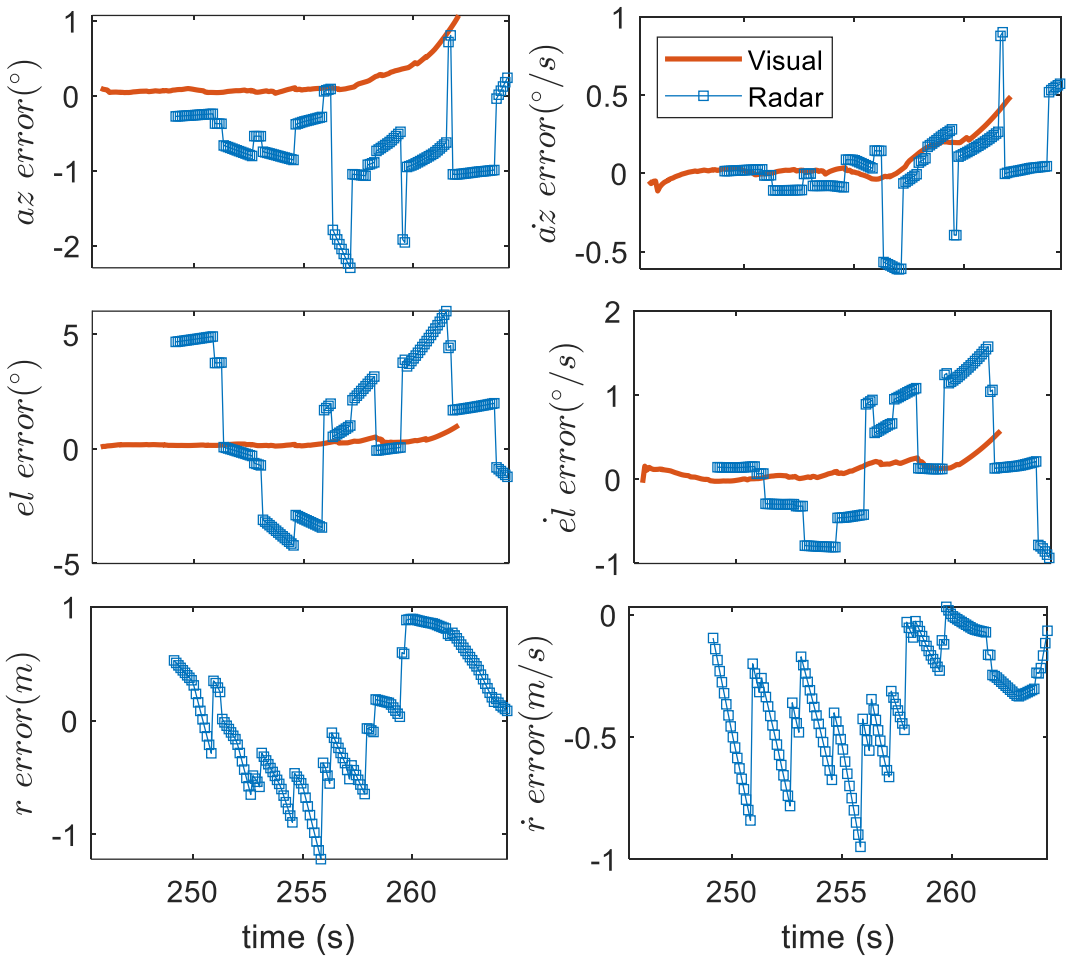

Figure 5.10 Dataset 1 – Encounter 1. Comparison of visual and RADAR tracking errors.

Table 5.2 Dataset 1 - Encounter 1. RMS for visual DL-based tracker and RADAR tracker.

	r error (m)	*ṙ* error (m/s)	*az* error (°)	*aż* error (°/s)	*el* error (°)	*ėl* error (°/s)
RADAR	0.54	0.41	0.80	0.24	3.1	0.71
Camera	-	-	0.29	0.07	0.21	0.17

Table 5.3 Dataset 1 - Encounter 2. RMS for visual DL-based tracker and RADAR tracker.

	r error (m)	*ṙ* error (m/s)	*az* error (°)	*aż* error (°/s)	*el* error (°)	*ėl* error (°/s)
RADAR	1.0	1.02	2.61	1.32	4.02	0.83
Camera	-	-	0.55	0.29	0.68	0.61

5.4.2 Results on dataset 2

Further results on the standalone visual- and RADAR-based tracking strategies are presented in this section where dataset 2 is exploited. Both visual strategies based on DL and MF-TM detectors are used and their performance in terms of accuracy are compared with the RADAR tracking solution. To properly assess such performance, the higher range encounter of flight 1, with maximum range slightly above 500

meters, is used. Tracker settings are the same used during analyses on dataset 1. For the visual MF-TM case the threshold T_{peak} is set to 0.55 with initial template dimensions of 5x11 pixels.

Results achieved with the two visual strategies are shown in Figure 5.11 and Figure 5.12 for DL and MF-TM approaches, respectively. A difference can immediately be noticed in terms of the distribution of OT (green circles). In the first case, these appear to be more concentrated in time and result from the identification of objects whose appearance is similar to Eagle. This happens, for instance, at time≈382 s where OTs of a bird can be seen. However, such track never successfully associates, thus no firm track (or tentative track) is ever generated as a result of the adequate choice of threshold $\tau_{tr,gen}$. In the MF-TM case, instead, OT are more distributed along the azimuth-elevation plots. The majority of this tracks are generated by the detections of small clouds in the upper parts of the image, as witnessed by the high values of the elevation measurement. In terms of performance, both strategies achieve similar accuracies, as reported in the RMS values of Table 5.4, with declaration ranges also comparable and reaching 500 meters. For the sake of clarity, it has to be remarked that such range is not an output of the visual pipeline and is evaluated based on the CDGNSS benchmark, instead. In both cases, OT tracks which actually belong to Eagle before the generation of its FT can be noticed. A TT can also be noticed in the DL case at time≈334 s (range about 520 meters), however, this never verifies association due to the very dim appearance of Eagle which only occupies few pixels on the image plane, causing either missed detections or detections with score lower than *S*.

As far as template matching and update performance are concerned, the values of N_{far}=14 pixels, N_{med}=20 pixels and N_{close}=30 pixels are considered to trigger template updates. This choice results in the generation of four templates with increasing dimensions. These are shown in Figure 5.13 where the dimensions are also reported.

The results of the RADAR-based tracking strategy are shown in Figure 5.14 and the achieved RMS values are also reported in Table 5.4. The declaration range, which is estimated by the tracking process, is surprisingly comparable to the visual one and only slightly higher (about 520 meters). As expected, the results achieved on

dataset 1 are confirmed in this case too, with angular accuracies being not comparable with the visual one, below 1° in azimuth and 2° in elevation. Nevertheless, range and range rate show the expected satisfactory values, with RMS below 2 m and 0.5 m/s, respectively.

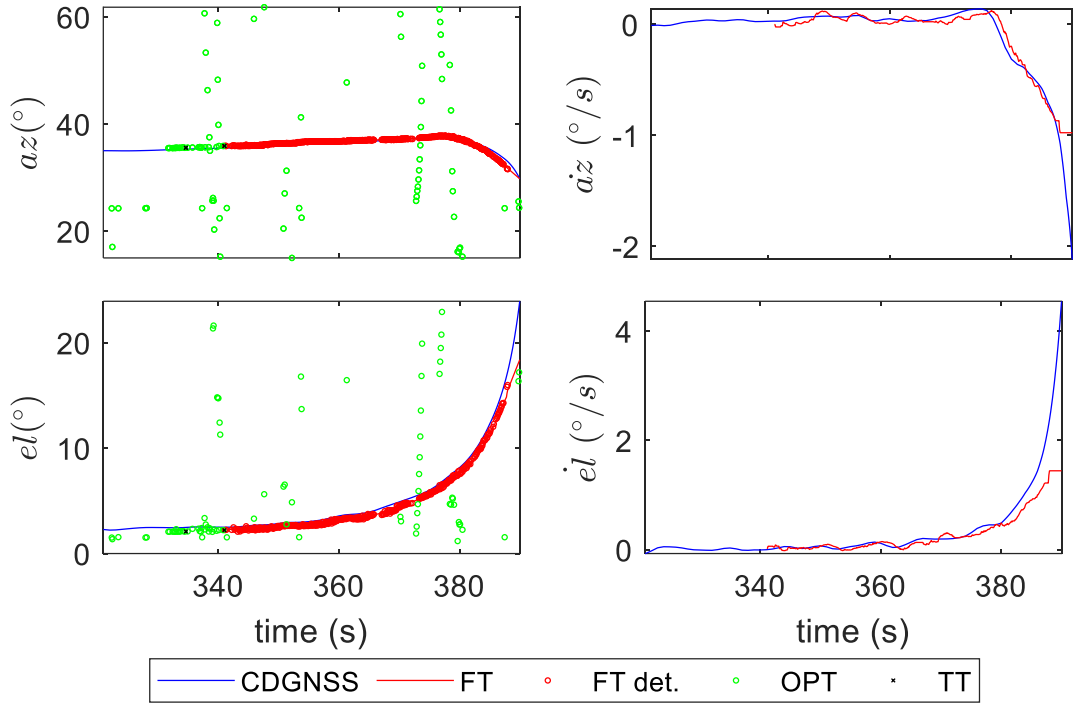

Figure 5.11 Dataset 2 - Flight 1 – Encounter 2. Results from DL-based visual tracking compared with benchmark.

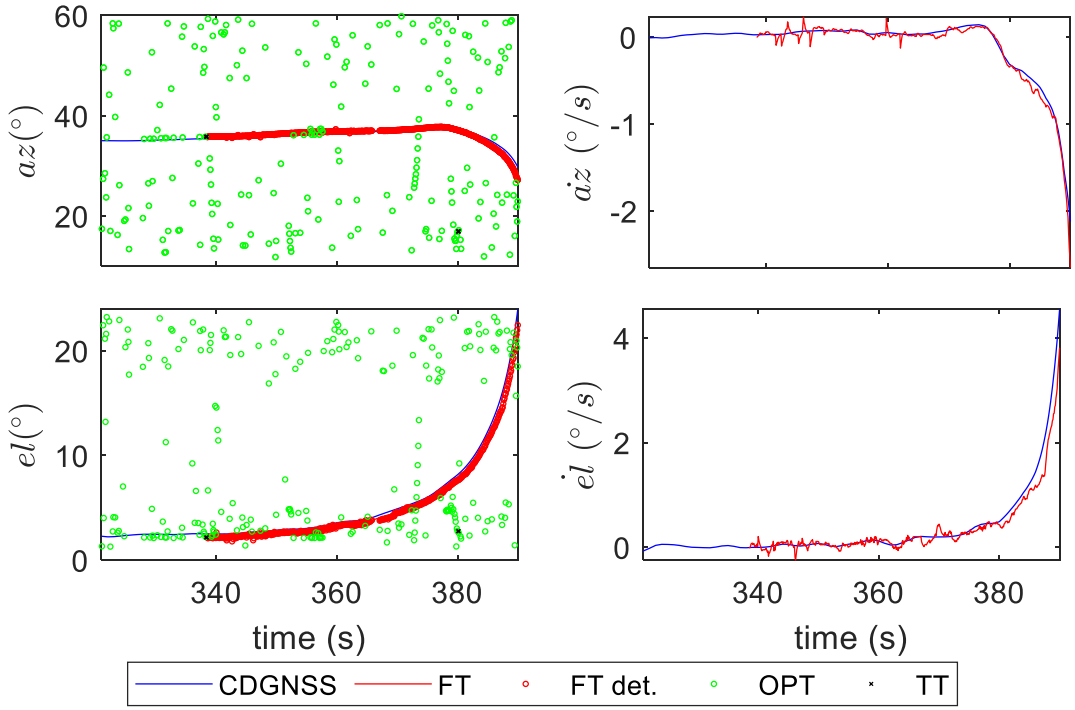

Figure 5.12 Dataset 2 - Flight 1 – Encounter 2. Results from MF-TM visual tracking compared with benchmark.

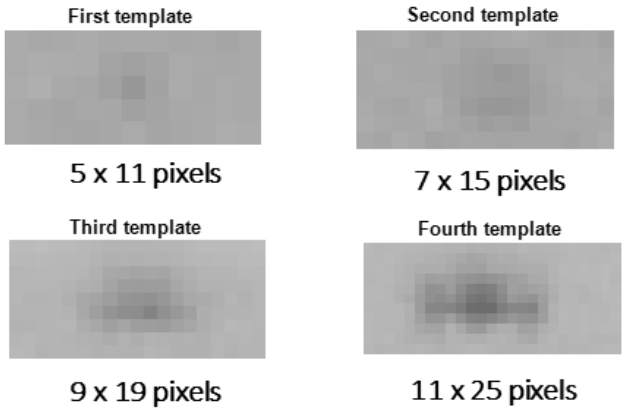

Figure 5.13 Dataset 2 – Flight 1 – Encounter 2. Templates generated during visual tracking with MF-TM approach. Dimensions of template are reported under each figure.

Table 5.4 Dataset 2 – Flight 1 - Encounter 2. RMS for visual DL, visual MF-TM and RADAR trackers.

	r error (m)	$\dot{r}$ error (m/s)	*az* error (°)	$\dot{az}$ error (°/s)	*el* error (°)	$\dot{el}$ error (°/s)
RADAR	1.46	0.32	1	0.24	1.85	0.44
Camera DL	-	-	0.23	0.05	0.41	0.06
Camera MFTM	-	-	0.26	0.04	0.37	0.07

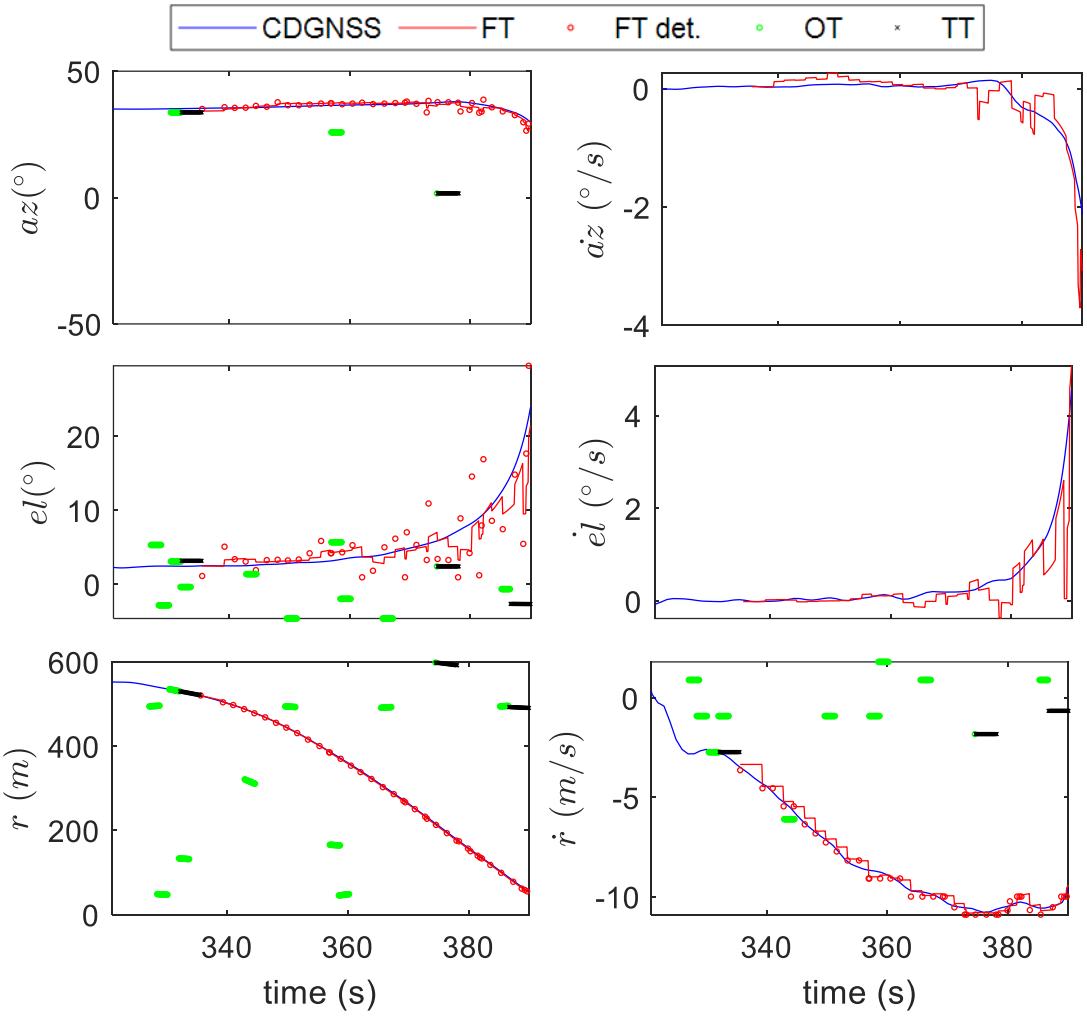

Figure 5.14 Dataset 2 - Flight 1 – Encounter 2. Results from RADAR tracking compared with benchmark.

Chapter 6: Fusion Strategies for Detect And Avoid

Data fusion approaches can be used to overcome the limits of standalone architectures and provide more accurate tracking solutions, which can be used to improve conflict detection and thus better support avoidance strategies. In the previous chapter of this manuscript, the performance of purely visual- and RADAR-based sensing architectures have been presented, thus highlighting advantages and limits in their exploitation. Specifically, highly accurate angular information is retrieved with the visual camera which, however, is not capable of any distance measurement. Although visual-based ranging estimates can be achieved by exploiting shape-based criteria, these depend on the knowledge of the intruder class, which dictates the choice of its dimensions, and can only be reliably applied up to limited distances of few hundreds of meters, as experimentally demonstrated in section 3.5. On the other hand, RADARs can achieve accurate distance (and radial velocity) information which can thus be employed to detect possible collisions using a less conservative criterion based on the distance at closest point of approach. Still, the latter also depends on the accuracy of angular rate estimates, as analytically demonstrated in [115], [116], which is coarser if a standalone RADAR architecture is used. Therefore, in this chapter, different RADAR/visual fusion strategies are proposed to leverage on the complementarity of the measurements and reduce the overall dependence of the architecture on the external environment, paid in terms of strong clutter presence (for the RADAR) and weather and illumination conditions (for the camera).

Fusion can be broadly classified based on the location where it is designed to take place, centralized or de-centralized (sensor-level), and on the level of processing applied on the data to be fused [115]-[117]. Within a centralized strategy, measurements (raw or processed) collected by the sensors are shared with a fusion center where, as the name suggests, their fusion is attempted. For this to be achieved, data sharing is required with consequent high costs in terms of communication links. Instead, in a de-centralized strategy each sensor processes its data independently and

fusion is performed on their final estimates by means of track-to-track fusion (T2TF) logics. In this case, computational power weighs over the single sensor and communication constraints can be relaxed as the data transmission is reduced.

The solutions discussed in this chapter encompass both centralized and de-centralized schemes and are tested on data collected during ground-to-air experimental tests with a sUAV flying in low altitude conditions. Specifically, encounters of dataset 2 are considered (section 4.3). The setup exploited consists of a low SWaP Echoflight RADAR, RGB visual camera and GNSS receiver and antenna for time synchronization, precise localization and CDGNSS benchmark generation. Details on the different strategies along with the logic behind their exploitation are provided in the following points.

1. The first solution proposed employs a hierarchical centralized fusion scheme (adapted from [14]) where the RADAR acts as the main sensor for firm track generation and the camera is used to improve the accuracy of the final solution. Thus, the detection phase can be considered de-centralized (each sensor is responsible for its own measurement retrieval and processing), and visual and RADAR measurements are combined within a unique EKF at firm tracking only. The choice of main sensor is made to provide high declaration ranges while strengthening the whole architecture towards the external conditions. The RADAR is, in fact, less impacted by weather and illumination and more performant in terms of detection ranges, thus being more capable and robust in the timely declaration of intruders within a DAA scenario [95].
2. A novel fusion solution is then proposed to provide an alternative to the RADAR data filtering and centroiding procedure described in section 5.3. This builds up on the centralized scheme of the previous point and adds computational complexity with the combination of two fusion steps. The first acts before tracking, leading to the definition of “Fuse-Before-Track”, where the camera is used as an aiding sensor for the filtering of RADAR data; the other takes place during tracking exploiting the hierarchical scheme introduced in the previous point. With respect to the latter, this

solution also increases the amount of data to be exchanged between sensors.

3. As a final solution, a de-centralized strategy is investigated by completely decoupling the RADAR and visual sensing processes. Thus, in this strategy, the data exchanged between the sensors is drastically reduced as only estimated firm tracks are required during fusion. This approach can be a powerful tool to perform data fusion within architectures where the sensors are tightly integrated with processing logics to produce higher-level tracking information only while the access to raw data is not possible or practical. The strategy provides combination of heterogeneous information, cartesian relative state for the RADAR and spherical relative state for the camera, exploiting sensor registration.

The remaining of the chapter is organized as follows. Section 6.1 reports the details of the hierarchical fusion strategy which is based on the centralized scheme where RADAR and visual measurements are combined within an EKF tracker. Such solution is tested exploiting two different visual-based detection algorithms, either based on deep learning approaches or on morphological filtering with adaptive template matching. The second central fusion scheme with "Fuse-Before-Track" (FBT) methodology is presented in section 6.2 while the T2TF logic and the mathematical model used to compare heterogeneous state vectors is presented in section 6.3. Finally, results achieved with the different strategies and the analyses thereof are provided in section 6.4.

6.1 HIERARCHICAL STRATEGY

On an algorithmic level, the difference with respect to the standalone RADAR tracker can only be noticed during firm tracking, where a double filtering scheme is implemented to account for the different measurements. The state vector used within the tracker is expressed as $\mathbf{x}=[x,y,z,\dot{x},\dot{y},\dot{z}]$ and, as in the case of the standalone RADAR solution, contains relative position and velocity of the targets expressed in terms of the cartesian coordinates in NED. Two measurement vectors are then built based on the different sensors; a RADAR measurement vector $\mathbf{z}_{\mathrm{RAD}}=[r,az_{RAD},el_{RAD},\dot{r}]$ with filtered and centroided measurements from the RADAR; a visual measurement vector $\mathbf{z}_{\mathrm{CAM}}=[az_{CAM},el_{CAM}]$ with azimuth and elevation retrieved by the pixel

coordinates extracted with visual detectors. Both measurements are rotated in the NED frame centered at the ground-based setup before being used during tracking.

The two visual detectors introduced in Chapter 5, either based on the DL approach or on the combination of morphological filtering and adaptive template matching, are used within the fused RADAR/visual strategy. Thus, two different fusion solutions are designed depending on the type of visual detector. The solutions are described in the following subsections.

6.1.1 Fusion with Deep Learning visual detector

The flow diagram of the RADAR/visual fused solution with DL-based measurement is shown in Figure 6.1. As also carried out in the purely visual solution (section 5.2), only measurements with a confidence score greater than a threshold (S) are used during tracking. However, in this case, these are only checked for association with firm tracks retrieved by the RADAR. Thus, when at least one firm track exists, two sequential processes are executed depending on which measurement is available. These processes are schematically represented by the RADAR and camera modules in Figure 6.1. In the former, which is the first to run, RADAR measurement-to-track association yielding to RADAR-based state correction in case of successful association. Then, if visual measurements are available, visual-based measurement-to-track association is attempted. In this case, either the RADAR-filtered state or the predicted one, depending on the outcome of the RADAR module association, is used. Thus, although the RADAR is used to decide if a firm track should be initiated, once generated visual measurements are used independently from the RADAR.

The different size of the visual measurement vector with respect to the RADAR one (accounting for two elements instead of four), makes it necessary to define a new measurement Jacobian matrix ($\mathrm{H_{CAM}}=\partial h(\mathbf{x})/\partial \mathbf{z}_{\mathrm{CAM}}$) which only contains the derivatives of azimuth and elevation with respect to the state components (built by only using the expressions of *h2* and *h3* from Eq. (5.6)). The measurement covariance matrix used in the visual module ($\mathrm{R_{CAM}}$) also accounts for the lower number of measurements thus being a 2 x 2 diagonal matrix.

The measurement-to-track association criteria exploited in the RADAR and camera modules are both based on the evaluation of the Mahalanobis distance. In the

RADAR case, the very same expression of Eq. (5.5) is used. In the visual case, such distance (ξ_{CAM}) is computed as shown in Eq. (6.1), instead. Here, $\hat{\mathbf{z}}_{CAM}$ is the vector containing the measurement prediction in terms of azimuth and elevation only.

$$\xi_{CAM} = (\mathbf{z}_{CAM} - \hat{\mathbf{z}}_{CAM})^T [H_{CAM}\hat{P} H_{CAM}^T + R_{CAM}]^{-1} (\mathbf{z}_{CAM} - \hat{\mathbf{z}}_{CAM}) \quad (6.1)$$

Visual measurement-to-track association is deemed successful if the distance is smaller than a threshold, $\xi_{CAM,th}$, set accordingly to the chi-square distribution of ξ_{CAM} with two degrees of freedom rather than four. This reduction thus verifies the condition $\xi_{CAM,th}<\xi_{RAD,th}$ with $\xi_{CAM,th}$=9.24.

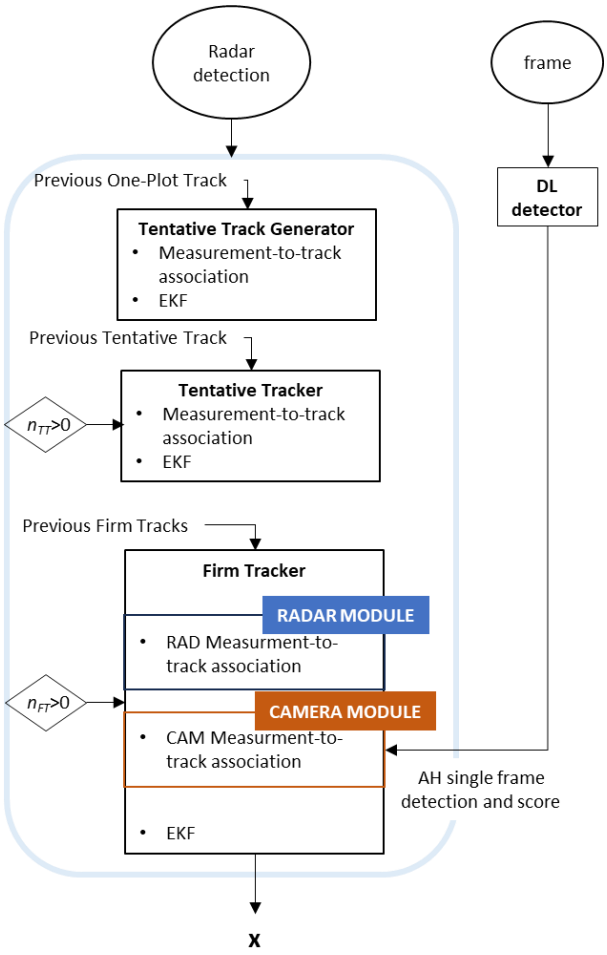

Figure 6.1 Flow diagram of the fused visual/RADAR EKF with DL-based measurements.

6.1.2 Fusion with morphological filter detector and adaptive template matching

The flow diagram of the fusion strategy exploiting morphological filtering and adaptive template matching is depicted in Figure 6.2. In this case the logic is similar to the previous one, thus exploiting visual detections only during firm tracking. Specifically, following the diagram of Figure 5.5, the measurements retrieved with

the morphological filtering approach of section 5.2 are used when RADAR firm tracks are initiated. Specifically, such measurements are used to generate a visual template (with dimensions $N_{x,\text{temp}}$x$N_{y,temp}$) of the object whose track is initiated. To do so, the association of MF measurements to such track must first be verified exploiting the same criterion used for the DL measurement fusion (thus computing the Mahalanobis distance of Eq. (6.1)). These steps are carried out within the "Template Generator" block of Figure 6.2. Once generated, the double correction scheme introduced in section 6.1.1, is used during firm tracking. However, in this case, measurements are no longer retrieved by the MF detector but with the template matching approach, instead. As in the visual-only case, template updates need to be performed to generate novel templates, with different dimensions, during the tracking procedure. Differently from the standalone visual case, however, such updates can be triggered based on the estimated distance (r_{est}) of tracked objects. Thus, a logic similar to the one discussed in section 5.2 can be implemented to identify the transition between different range-based regions and update the template when the target passes from far to medium ($r_{est} \leq r_{far}$) and from medium to close ($r_{est} \leq r_{med}$) range regions.

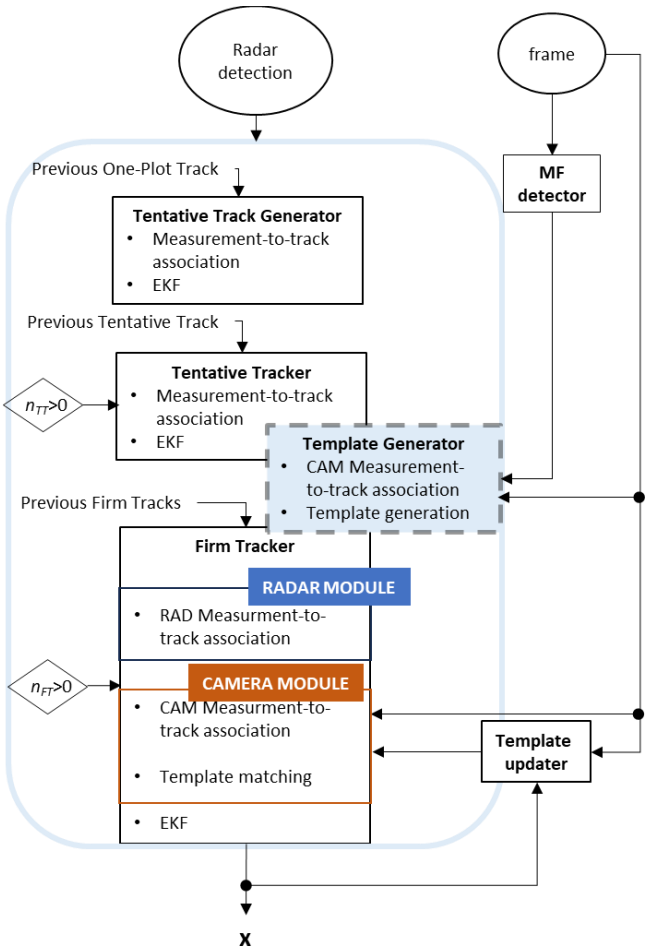

Figure 6.2 Flow diagram of the fused visual/RADAR EKF with MF-based measurement and adaptive template matching.

6.2 FUSE-BEFORE-TRACK STRATEGY

The FBT fusion strategy is here detailed using different subsections. The former, presents the innovative fusion step designed to act on the measurement level to filter RADAR detections. The latter, focuses on the tracking and DAA-related performance assessment providing the methods used to evaluate distance and time at closest point of approach. The tracking strategy is the same of the hierarchical solution discussed in the previous sub-section and its presentation is therefore omitted.

6.2.1 FBT methodology

In the FBT step, RADAR measurements are projected on the image plane and compared to the corresponding visual detections (extracted with the DL detector) to verify their consistency with the visual data, which are not affected by the same clutter phenomenology. This processing step requires to account for the asynchrony

between the two sensors' acquisition, as raw RADAR detections and RGB images are collected with different frequencies. Given a frame acquired by the camera at time t^*_{cam}, all RADAR data whose time-tag falls in the interval $t^*_{cam} \pm \Delta t_{cam}/2$ (where Δt_{cam} is the interval between two consecutive frame acquisitions) are considered as candidate measurement for this confirmation step.

Once the subset of closest-in-time RADAR measurements is identified, a Doppler-based filter is applied to discard detections plausibly arising from static ground echoes (i.e., all RADAR measurements with Doppler below a threshold $\dot{r}_{th,low}$ are removed). Then the directions of the remaining RADAR beams are projected on the image plane. To do so, the unit vectors representing the center of such beams are first rotated from RRF to CRF (using the attitude matrices computed with QUEST), leading to the coordinates x_{RAD}, y_{RAD} and z_{RAD}. Then, they are converted in pixel coordinates (i.e., u_{rad} and v_{rad}) solving the inverse mapping problem accounting for the plumb-bob intrinsic camera model [120] as shown in Eq. (6.2) where $fc(1)$, $fc(2)$ are the components of the focal length of the camera in pixels, $kc(1),..,kc(4)$ are the distortion coefficients, and (c_x,c_y) are the principal point coordinates.

$$
\begin{aligned}
u_{RAD} &= fc(1)\left[\frac{x_{RAD}}{z_{RAD}}\left(1+kc(1)r^2+kc(2)r^4\right)+2kc(3)\left(\frac{x_{RAD}}{z_{RAD}}\right)\left(\frac{y_{RAD}}{z_{RAD}}\right)+kc(4)\left(r^2+2\left(\frac{x_{RAD}}{z_{RAD}}\right)^2\right)\right]+ \\
&+c_x \\
v_{RAD} &= fc(2)\left[\frac{y_{RAD}}{z_{RAD}}\left(1+kc(1)r^2+kc(2)r^4\right)+kc(3)\left(r^2+2\left(\frac{y_{RAD}}{z_{RAD}}\right)^2\right)+2kc(4)\left(\frac{x_{RAD}}{z_{RAD}}\right)\left(\frac{y_{RAD}}{z_{RAD}}\right)\right]+ \\
&+c_y \\
r &= \sqrt{\left(\frac{x_{RAD}}{z_{RAD}}\right)^2+\left(\frac{y_{RAD}}{z_{RAD}}\right)^2}
\end{aligned}
\tag{6.2}
$$

An illustration of a RADAR beam projection is shown in Figure 6.3, where the image plane (x_{IMG}-y_{IMG}) is depicted. Beams whose projection fall outside the image plane borders are discarded as their confirmation with visual data cannot be performed. The projected RADAR beam is used as the center of a rectangular Region Of Interest (ROI) whose half-width (Δu) and half-height (Δv) are expressed in pixels and are chosen accounting for the angular dimensions of the RADAR beam, both in azimuth and elevation, and the camera IFOV. Furthermore, the size of the ROI is also adjusted with respect to the image dimensions, thus using reduced values

of Δu and Δv depending on the location of the ROI's center with respect to the image margins. At this stage, consistency of the RADAR measurements is verified if one or more visual detections fall within the limits of the newly built ROIs, thus confirming that the corresponding set of RADAR measurements can be preserved and furtherly used for tracking. Indeed, RADAR measurements whose confirmation is not verified are discarded.

RADAR detections which have been confirmed with the FBT procedure are also time-tagged using the time of the frame which has enabled their confirmation. Therefore, at the end of this process, RADAR and visual measurements to be injected in the tracker are referred to the same time epoch.

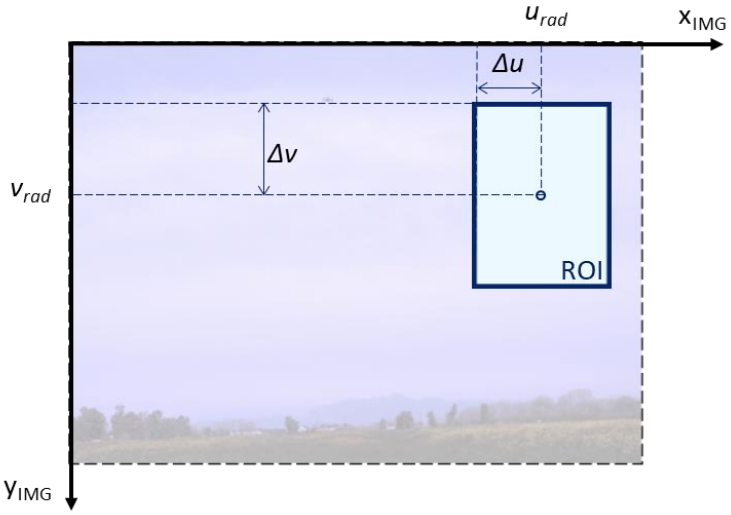

Figure 6.3 Graphical illustration of the generation of a ROI from RADAR beam projection on the image plane.

6.2.2 Conflict detection methodology

Firm tracks are generated exploiting the FBT-filtered RADAR measurements and the visual measurements which are used within a unique EKF exploiting the strategy of section 6.1. The retrieve tracks are then further processed to determine whether they represents a collision threat. This is done through a conflict detection analysis which relies on the computation of the time to closest point of approach (t_{CPA}) and the distance at closest point of approach (d_{CPA}) with the formulations shown in section 3.2. However, a further analysis is here proposed decoupling the horizontal ($d_{CPA,hor}$) and vertical ($d_{CPA,vert}$) components of $\mathbf{d}_{\mathrm{CPA}}$ which are separately investigated. This separation makes it possible to be more adherent to the definition of a cylindrical safety region following the Near-Mid-Air Collision (NMAC) concept

[121]. The uncertainty in the estimation of the components of $\mathbf{d}_{CPA}$, i.e., $\sigma_{dCPA,hor}$ and $\sigma_{dCPA,vert}$ along horizontal and vertical directions, are also evaluated. These depend strongly on the uncertainty arising from tracking estimates as shown in Eq. (6.3).

In such equation, the squared uncertainty in range (σ_r), azimuth (σ_{az}), elevation (σ_{el}), range rate ($\sigma_{\dot{r}}$), azimuth rate ($\sigma_{a\dot{z}}$) and elevation rate ($\sigma_{e\dot{l}}$) are exploited. These quantities are computed by transforming the state covariance matrix P, expressed in cartesian terms, in a spherical one $P_s=D_sP(D_s)^T$ where D_s is the Jacobian of the spherically-expressed state with respect to its cartesian representation.

$$\begin{aligned}\sigma^2_{dCPA,hor} &= \left(\frac{\partial d_{CPA,hor}}{\partial r}\right)^2 \sigma^2_r + \left(\frac{\partial d_{CPA,hor}}{\partial \dot{r}}\right)^2 \sigma^2_{\dot{r}} + \left(\frac{\partial d_{CPA,hor}}{\partial az}\right)^2 \sigma^2_{az} + \left(\frac{\partial d_{CPA,hor}}{\partial a\dot{z}}\right)^2 \sigma^2_{a\dot{z}} + \\ &+ \left(\frac{\partial d_{CPA,hor}}{\partial el}\right)^2 \sigma^2_{el} + \left(\frac{\partial d_{CPA,hor}}{\partial e\dot{l}}\right)^2 \sigma^2_{e\dot{l}} \\ \sigma^2_{dCPA,vert} &= \left(\frac{\partial d_{CPA,vert}}{\partial r}\right)^2 \sigma^2_r + \left(\frac{\partial d_{CPA,vert}}{\partial \dot{r}}\right)^2 \sigma^2_{\dot{r}} + \left(\frac{\partial d_{CPA,vert}}{\partial az}\right)^2 \sigma^2_{az} + \left(\frac{\partial d_{CPA,vert}}{\partial a\dot{z}}\right)^2 \sigma^2_{a\dot{z}} + \\ &+ \left(\frac{\partial d_{CPA,vert}}{\partial el}\right)^2 \sigma^2_{el} + \left(\frac{\partial d_{CPA,vert}}{\partial e\dot{l}}\right)^2 \sigma^2_{e\dot{l}}\end{aligned} \tag{6.3}$$

6.3 TRACK-TO-TRACK STRATEGY

In the track-to-track fusion strategy, the estimates retrieved by Local, standalone sensor-based Trackers (LTs) are sent to a Fusion Center (FC) where their association (track-to-track association, T2TA) is attempted to decide whether the two tracks are related to the same object and are, therefore, suitable for fusion. The proposed strategy is schematically represented in Figure 6.4 where the two sensor-level LTs (visual and RADAR-based), are shown. The RADAR LT exploits filtered and centroided measurements rotated in NED ($\mathbf{z}_{RAD}$) within the EKF tracker presented in section 5.3, thus retrieving estimates of a state vector expressed as $\mathbf{x}_{RAD}=[x,y,z,\dot{x},\dot{y},\dot{z}]$ whose covariance matrix is P_{RAD}. On the other hand, the visual LT uses the DL-based detection approach and builds estimates $\mathbf{x}_{CAM}=[az,el,a\dot{z},e\dot{l}]$ with uncertainty contained within the covariance matrix P_{CAM}, exploiting camera-retrieved angular measurements in NED ($\mathbf{z}_{CAM}$) within the KF structure presented in section 5.2. Therefore, while the $\mathbf{x}_{RAD}$ vector contains the cartesian components of the

relative position and velocity of the tracked object, the $\mathbf{x}_{CAM}$ vector only contains bearing (line of sight) and bearing rate information, expressed in terms of the azimuth and elevation angles, and their derivatives. Once a FT is established by both LTs, the corresponding state estimates ($\mathbf{x}_{RAD,FT}$ for the RADAR and $\mathbf{x}_{CAM,FT}$ for the camera) and state covariance matrices ($P_{RAD,FT}$ and $P_{CAM,FT}$) are passed to a fusion center where T2TF is performed upon T2TA verification. However, both association and fusion steps must account for the heterogeneity of the two state vectors [122], [123] which are defined in different spaces. This issue can be solved by exploiting camera/RADAR calibration which is taken into account within the FC. Specifically, the RADAR-based estimate is converted in polar coordinates by exploiting the non-linear relationship $g(\mathbf{x}_{RAD,FT})$ whose components are listed in Eq. (6.4) where $[\Delta x_{RC},\Delta y_{RC},\Delta z_{RC}]$ is the camera position vector with respect to the RADAR in NED.

$$
\begin{aligned}
g_1 &= az(\mathbf{x}_{RAD,FT}) = tg^{-1}\left(\frac{y-\Delta y_{RC}}{x-\Delta x_{RC}}\right)\\
g_2 &= el(\mathbf{x}_{RAD,FT}) = \sin^{-1}\left(\frac{z-\Delta z_{RC}}{r}\right)\\
g_3 &= a\dot{z}(\mathbf{x}_{RAD,FT}) = \frac{-(y-\Delta y_{RC})\dot{x}+(x-\Delta x_{RC})\dot{y}}{(x-\Delta x_{RC})^2+(y-\Delta y_{RC})^2}\\
g_4 &= e\dot{l}(\mathbf{x}_{RAD,FT}) = -\frac{\frac{\dot{z}}{r}}{\sqrt{1-\frac{(z-\Delta z_{RC})^2}{r^2}}} + \\
&+\frac{\frac{z\left[(x-\Delta x_{RC})\dot{x}+(y-\Delta y_{RC})\dot{y}+(z-\Delta z_{RC})\dot{z}\right]}{r^3}}{\sqrt{1-\frac{(z-\Delta z_{RC})^2}{r^2}}}\\
r &= \sqrt{(x-\Delta x_{RC})^2+(y-\Delta y_{RC})^2+(z-\Delta z_{RC})^2}
\end{aligned}
\tag{6.4}
$$

From this expression, a Jacobian matrix $G=\partial g(\mathbf{x}_{RAD,FT})/\partial \mathbf{x}_{RAD,FT}$ can be computed and used to weight the two estimates after their association has been verified. Association is performed adopting the Mahalanobis distance criterion which, in this case, must consider the residual between the two estimates and account for their uncertainties, contained within their covariance matrices. The resulting Mahalanobis distance (ξ_F) is evaluated as follows.

$$\xi_F = (\mathbf{x}_{CAM,FT} - g(\mathbf{x}_{RAD,FT}))^T (GP_{RAD,FT}G^T + P_{CAM,FT})^{-1} \ldots (\mathbf{x}_{CAM,FT} - g(\mathbf{x}_{RAD,FT})) \quad (6.5)$$

For T2TA to be valid, the condition $\xi_F < \xi_{F,th}$ must be verified where the threshold ($\xi_{F,th}$) must be chosen according to the degrees of freedom of ξ_F which are equal to the number of estimate contained within $\mathbf{x}_{CAM,FT}$ (4 in the analyzed case). If a successful association condition is found, the two states are exploited to define a fused state estimate ($\mathbf{x}_{FUSED,FT}$) and its covariance ($P_{FUSED,FT}$) using the gain matrix (K_F) as follows.

$$\begin{aligned} K_F &= P_{RAD,FT}G(GP_{RAD,FT}G^T + P_{CAM,FT})^{-1} \\ \mathbf{x}_{FUSED,FT} &= \mathbf{x}_{RAD,FT} + K_F(\mathbf{x}_{CAM,FT} - g(\mathbf{x}_{RAD,FT})) \\ P_{FUSED,FT} &= (I - K_FG)P_{RAD,FT} \end{aligned} \quad (6.6)$$

The proposed T2TF method is based on the availability of both LT-estimated states and covariances. Therefore, if the aforementioned visual and RADAR LTs are implemented, it can only be exploited once both LTs have reached the firm tracking step. This limitation is mostly imposed by the visual LT which is designed as to exploit a linear KF only at firm tracking level, thus making the information of a state covariance matrix unavailable when lower-level tracks are established.

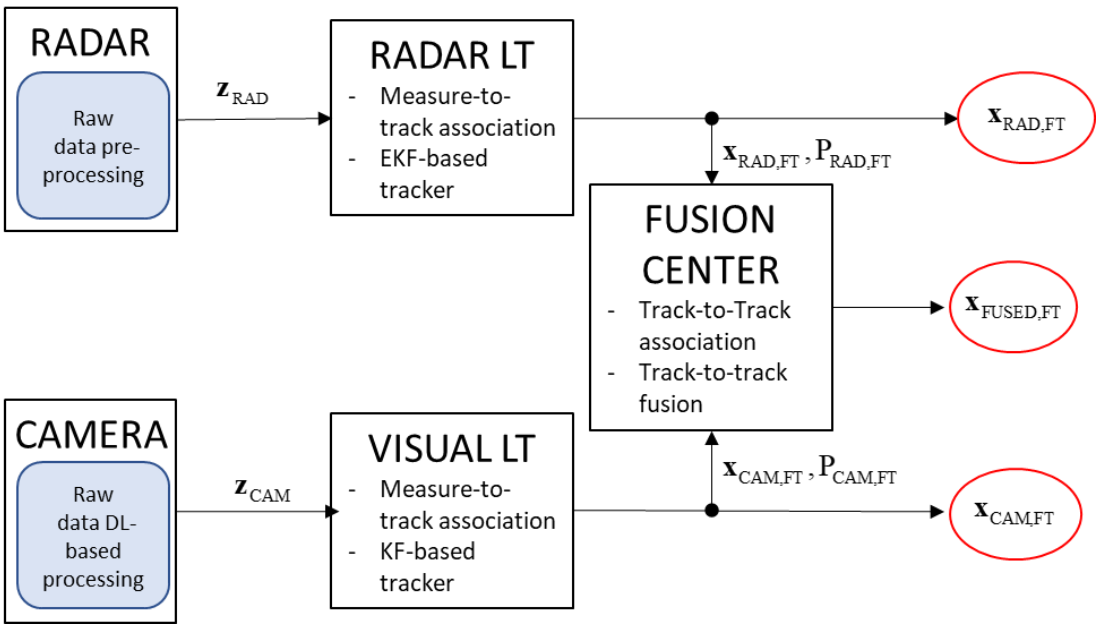

Figure 6.4 Scheme of the proposed Track-to-Track fusion strategy.

6.4 EXPERIMENTAL RESULTS

6.4.1 Hierarchical Fusion Results

In this subsection the results of the hierarchical fusion strategies with the two visual approaches of section 6.1 are presented. The strategies are tested on the same encounter used for the standalone visual and RADAR strategies discussed in section 5.4 (dataset 2, flight 1, encounter 2). The latter maximizes the range achieved by Eagle during flight, thus enabling the analysis of the performance in a more challenging condition with respect to the other two encounters. Settings used for the tracker are the same of the EKF-RADAR-only one (section 5.3), with a sampling time T=0.1 s; visual DL measurements are only used when their score is higher than S=0.4. Results are shown in Figure 6.5 and Figure 6.6 for the DL and MF with TM approaches, respectively. To ease the understanding of the figures, only results relative to firm tracking are shown. Specifically, the RADAR and visual measurement used for firm track correction are depicted as blue and green shaded circles. As it can be noticed, in the last part of the encounter (time>385 s) a slightly higher number of visual measurements is used with the MF-TM approach rather than the DL one. This occurrence can be imputed to the higher difficulty of the CNN detector whose training was focused on identification of the sUAV at large distances. As far as the declaration range is concerned, due to the hierarchy of the strategy, this is all imputed to the generation of a firm track from RADAR measurements. As a consequence, the same range as the standalone RADAR EKF case is achieved (about 520 meters). As far as template matching is concerned, templates generated during the tracking process are shown in Figure 6.7 where their dimensions are also reported. Starting from the first template, generated right after the first firm track initiation, other templates are generated using the thresholds on the estimated range of r_{far}=350 m and r_{med}=150 m.

To better highlight the difference between the two implementations (labelled as “Rad DL” and “Rad MFTM” for DL-based and MF with TM approaches) and the benefits with respect to the standalone RADAR case, firm tracking errors are reported in Figure 6.8 and the root mean square (rms) values are listed in in Table 6.1. In both figure and table, the standalone RADAR case (“Rad only”) is also reported to remark the results. With respect to the latter, angular accuracies are much

improved, with RMS values dropped down to below the degree level for both azimuth and elevation while range and range rate do not seem to show any significant variation.

It is possible to conclude that the advantages of exploiting a fused strategy, rather than a standalone RADAR-based one, are proven in terms of a better angular and angular rate accuracy (sub-degree), coupled with the highly accurate range and range rate estimates (below meter and meter-per-second levels). Declaration range is also comparable to maximum of the encounter.

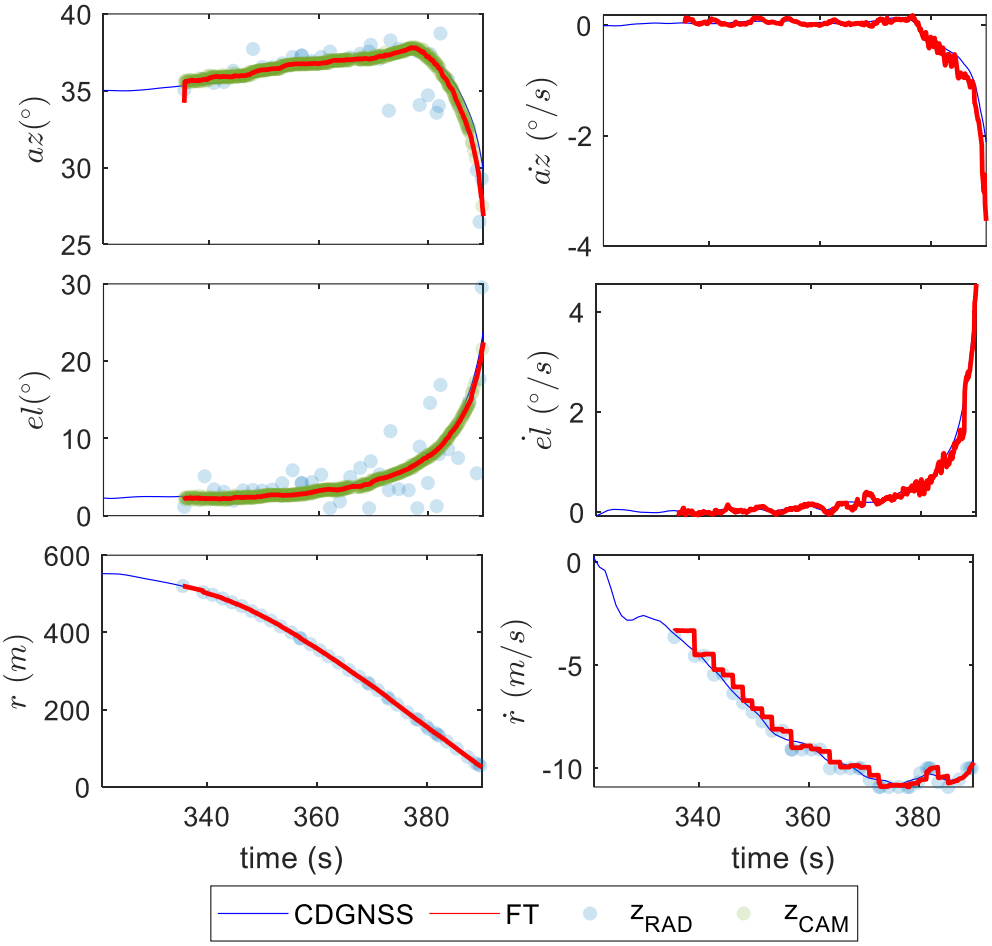

Figure 6.5 Dataset 2 – Flight 1 – Encounter 2. Results of the hierarchical visual/RADAR fusion strategy with DL-based measurements.

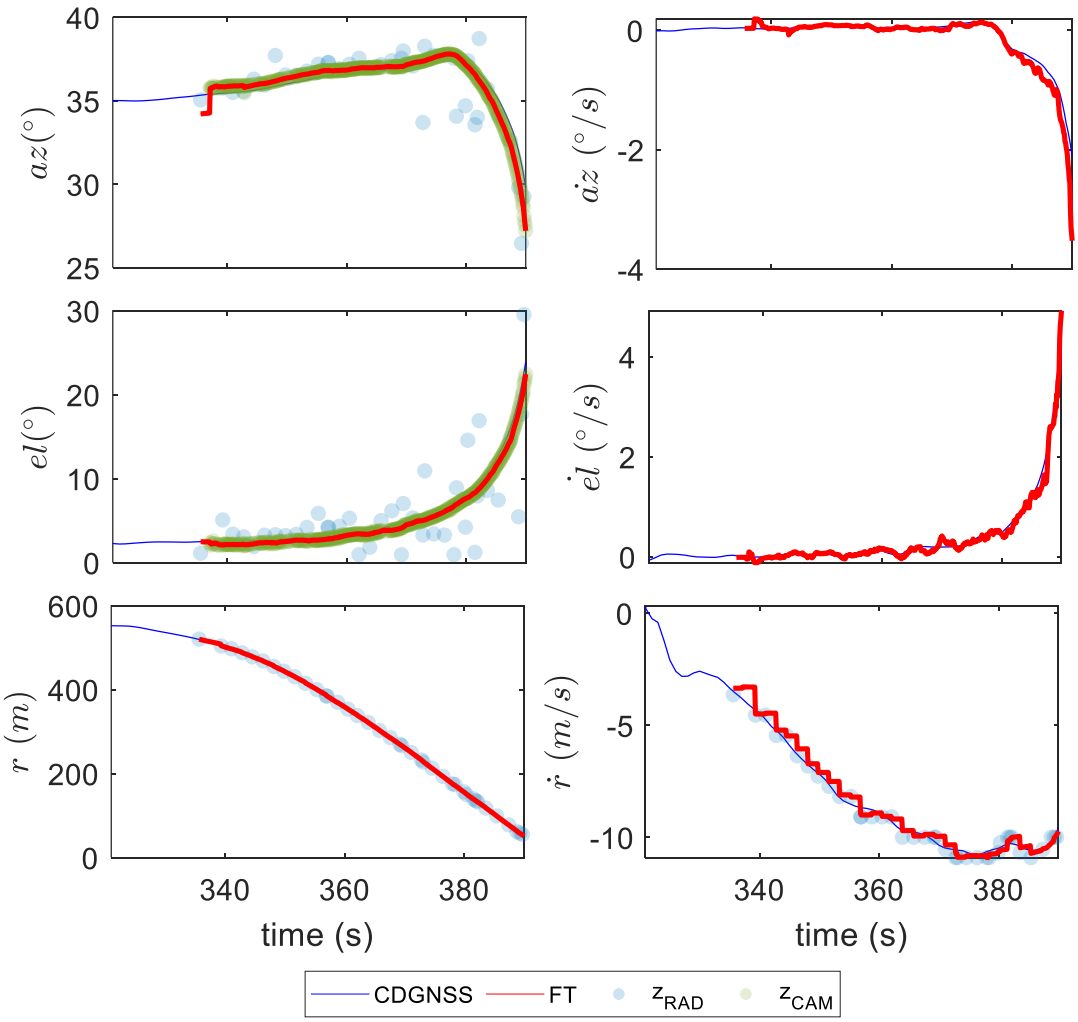

Figure 6.6 Dataset 2 – Flight 1 – Encounter 2. Results of the hierarchical visual/RADAR fusion strategy with MF-TM approach.

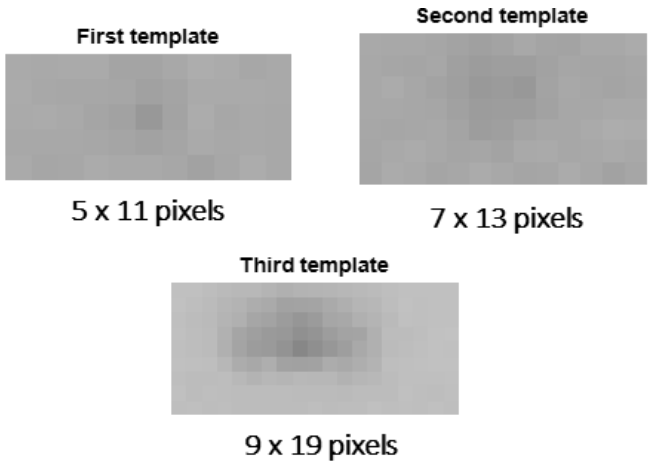

Figure 6.7 Dataset 2 – Flight 1 – Encounter 2. Templates generated during the template generator and update procedures of the visual/RADAR fusion strategy with MF-TM approach.

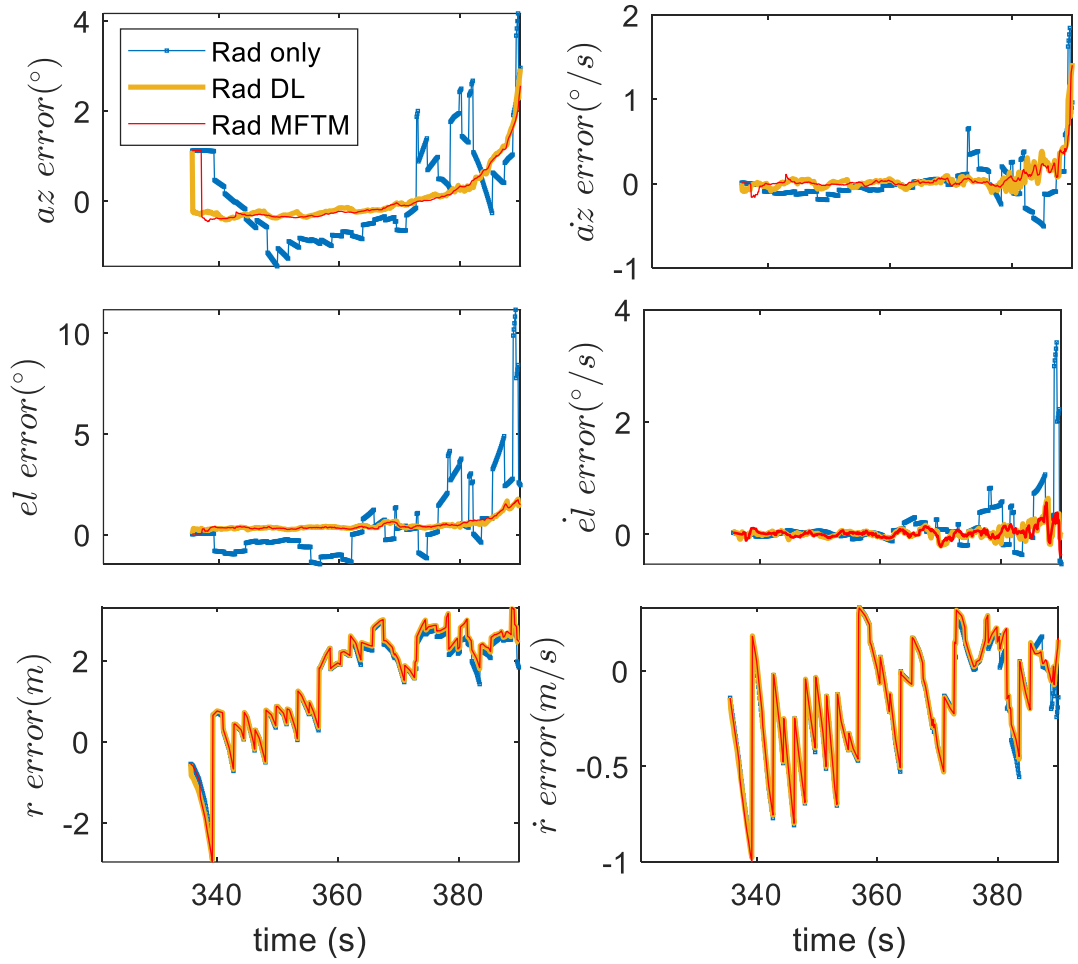

Figure 6.8 Dataset 2 - Flight 1 – Encounter 2. Comparison of errors with respect to benchmark achieved with the different fusion strategies. Standalone RADAR solution is also reported.

Table 6.1 Dataset 2 - Flight 1 – Encounter 2. RMS for fused visual/RADAR trackers.

	r error (m)	*ṙ* error (m/s)	*az* error (°)	*ȧz* error (°/s)	*el* error (°)	*ėl* error (°/s)
Rad DL	1.98	0.32	0.65	0.21	0.75	0.25
Rad MFTM	1.98	0.32	0.67	0.2	0.76	0.23
Rad only (section 5.4.2)	1.46	0.32	1	0.24	1.85	0.44

6.4.2 Fuse-Before-Track Fusion Results

The results achieved with the FBT fusion approach are divided in three different sections. The first one focuses on the analyses of the output of the RADAR filtering strategy which, within the proposed approach, represents the first level of data fusion. Then, the tracking results achieved exploiting the RADAR measurements retrieved with FBT and the visual measurements within the hierarchical tracker are discussed. Finally, the application of the double fusion

scheme is also evaluated in terms of conflict detection performance. The latter is evaluated in terms of accuracy with respect to the benchmark.

All analyses are carried out exploiting all encounters (from both flights) of dataset 2. Therefore, for the sake of brevity of the following discussions, each of the cases are reported by following the nomenclature F[N_{flight}]E[$N_{encounter}$]where N_{flight} is the flight number, either 1 or 2, and $N_{encounter}$ is the encounter number, as reported in Table 4.4.

6.4.2.1 FBT results

A visualization of the results of the FBT procedure on the 445th frame of case F1E3 is shown in Figure 6.9, where detections retrieved with the CNN, are depicted as red circles, while RADAR ROIs are shown as colored rectangles. As it can be noticed, two different ROIs are projected on the image plane. Such ROIs correspond to RADAR beams which are the closest in time to the considered frame and verify both their projectability on the image plane and the occurrence of non-null $\dot{r}$ measurements. However, only one ROI appears to be confirmed (colored in green) due to the presence of an AH measurement which corresponds to Eagle, as shown in the left part of the figure where a zoom over the confirmed ROI is provided. The values set for ROI dimensions are Δu=160 pixels and Δv=300 pixels.

An example of the RADAR measurements retrieved on case F1E3 after FBT is shown in Figure 6.10 where the unprocessed RADAR measurements (a) and the corresponding FBT-filtered ones (b) are reported. The difference between the two outputs remarks the efficacy of the proposed solution in removing noise and clutter, thus only retaining measurements which are pertinent to objects of interest. Visual measurements confirming RADAR ones are shown as green crosses in the azimuth and elevation fields of Figure 6.10(b) where the CDGNSS benchmark is also reported to visualize the accuracy of the measurements. While confirmed RADAR range and range rate measurements show a good accordance with the benchmark, the same is not observed for the angular measurements. These verify the expected grid-like trend which derives from the RADAR operating procedure. Outliers in RADAR measurements, caused by false detections (which do not correspond to Eagle), are observed after the application of the FBT procedure in all the tested cases. The generation of such outliers can be imputed to different causes which range from the

presence of multi-detections in a single confirmed RADAR beam, to the observation of targets whose appearance is similar to Eagle's (typically birds flying at long distance from the camera) and, finally, also account for the occurrence of missed frames (verified during experimental tests). When the latter eventuality occurs, RADAR measurements are still collected around the frame time-tag and then centroided as discussed in section 5.3. In the cases of flight 2, an additional outlier generation phenomenon is observed which is due to the relation between the $\dot{r}$ estimates of the RADAR and the actual approaching speed of Eagle. During the encounters of flight 2 such speed reaches values of about 15 m/s which is slightly above the maximum unambiguous velocity of the RADAR, thus causing the generation of Doppler-only outliers. Outliers in measurements can be easily spotted by exploiting the available CDGNSS-based benchmark. Specifically, given the higher accuracy of the sensor in the range field, the error in range between the measurement and the benchmark can be computed and outliers can be removed if such error is found to be higher than a threshold, set to 4 meters. The number of outliers can then serve as a performance metric to evaluate the quality of FBT with respect to the filtering and centroiding procedure. On flight 1, a drastic reduction of outliers from an average of 20 to only 6 is verified. Still, such reduction is not likewise followed in flight 2 where FBT collects an average of 30 outliers, mostly found in encounter 1 (which is the only case when more outliers are found in the FBT results rather than in the filtering and centroiding ones).

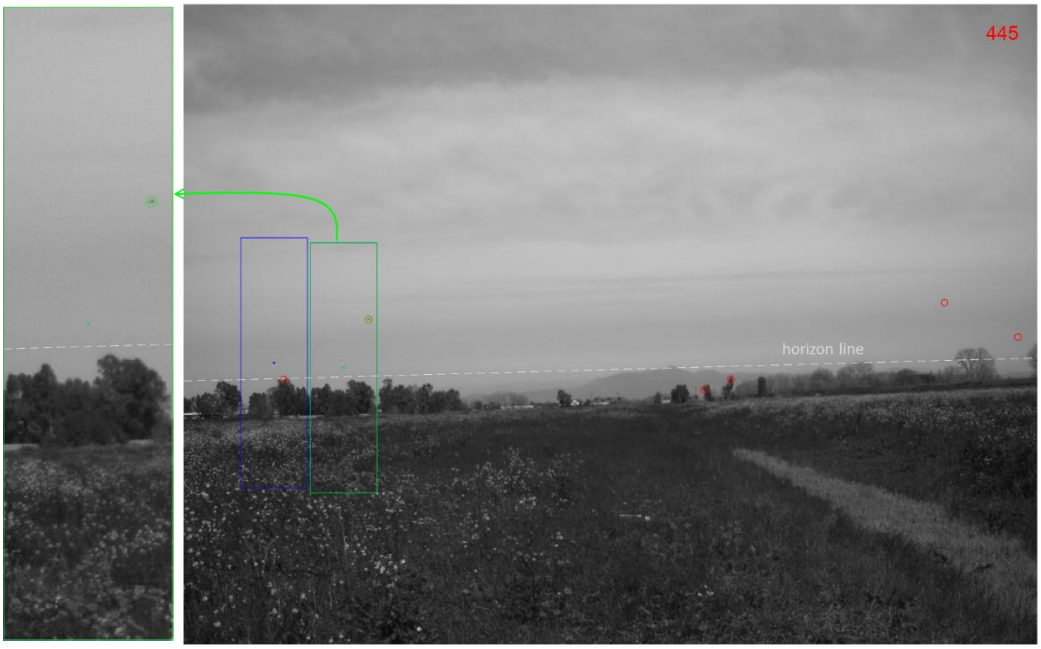

Figure 6.9 Results of the FBT filtering procedure on one frame from case F1E3 of dataset 2. RADAR ROI depicted as rectangles. Visual measurements are depicted as red circles. Confirmed RADAR ROI is highlighted in green and zoomed on the left part of the figure. Dataset 2.

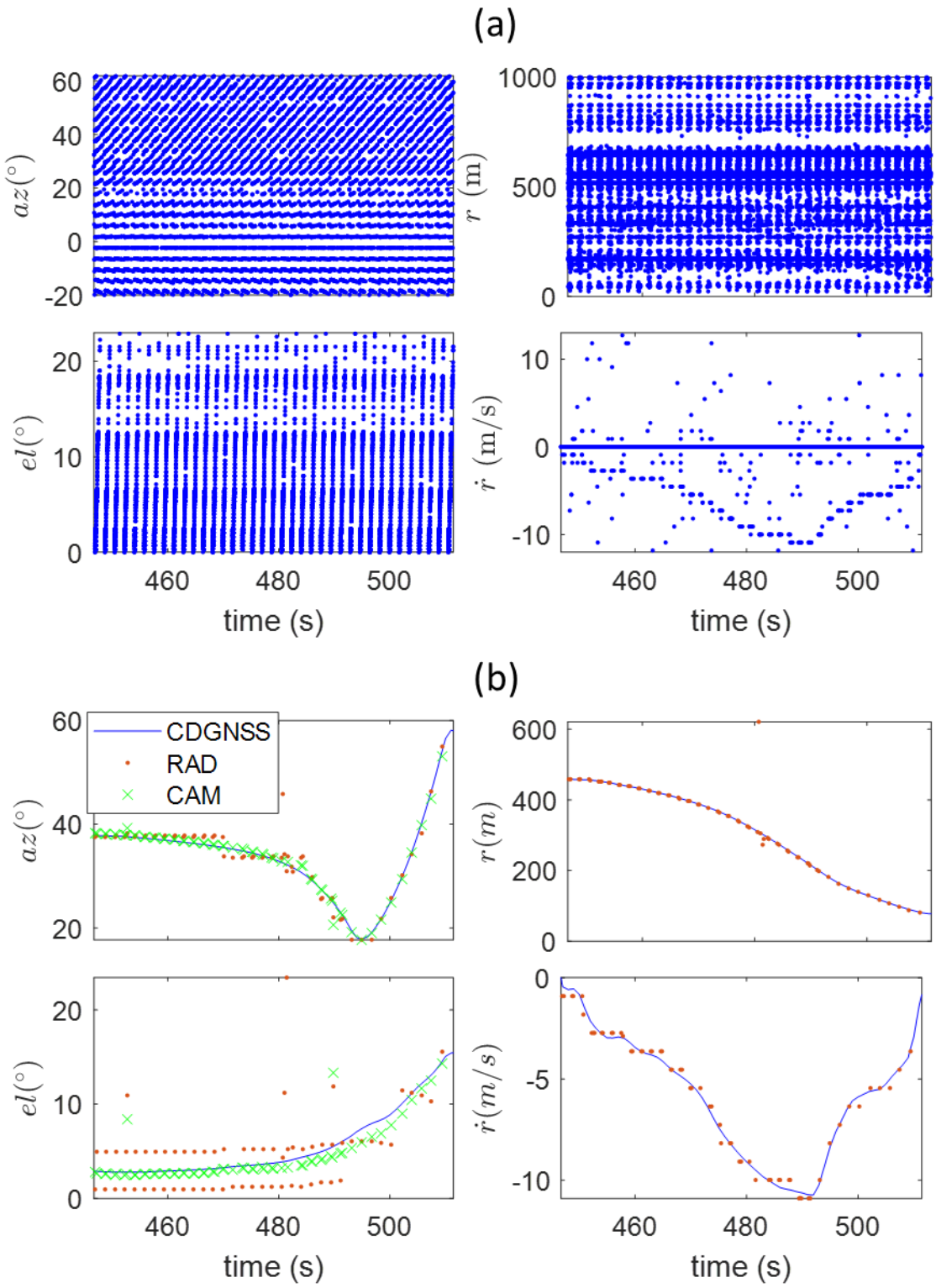

Figure 6.10 (a) Un-processed RADAR measurements rotated in NED for the case F1E3. (b) Results of the FBT procedure on case F1E3. Dataset 2.

6.4.2.2 Tracking and conflict detection results

Tracking results show the expected performance already observed in the previous case. Thus, for the sake of brevity, these are only shortly reported. Once again, performance can be evaluated by analysing the RMS achieved on the errors between tracking estimated and CDGNSS benchmark. These are reported in Table 6.2 where all the cases analysed are listed, demonstrating that meter-level accuracy on range and sub-degree accuracy on angles is once again achieved. With the proposed fusion strategy, whose tracking performance appear in any case comparable with the previous one, on average a reduction of about 79% in the angular error is achieved with respect to the standalone RADAR case. Declaration ranges (r_{FT}) are also reported in the table, showing high values, comparable to the maximum achieved during the encounter (listed in Table 4.4). However, by comparing the value achieved on the F1E2 case, which is the same analysed for the hierarchical fusion solution, a reduction of about 15 meters can be noticed. This can be imputed to the different RADAR measurement filtering strategy which evidently causes the loss of information due to lack of confirmation from the camera.

Table 6.2 Dataset 2 - Flight 1 – Encounter 2. RMS for fused visual/RADAR tracker with FBT strategy.

Case	r error (m)	$\dot{r}$ error (m/s)	az error (°)	$a\dot{z}$ error (°/s)	el error (°)	$\dot{el}$ error (°/s)	r_{FT} (m)
F1E1	1.54	0.31	0.28	0.05	0.40	0.07	386.5
F1E2	1.33	0.31	0.25	0.05	0.39	0.07	505.1
F1E3	1.56	0.49	0.41	0.28	0.77	0.08	457.9
F2E1	1.96	0.47	0.35	0.06	0.49	0.08	516.6
F2E2	1.89	0.47	0.31	0.05	0.35	0.04	502

Explicative examples of the conflict detection results are shown for the cases F1E3 and F2E2 in Figure 6.11. In the first, the behavior of t_{CPA}, $d_{CPA,hor}$ and $d_{CPA,vert}$ is shown with respect to time along with the reference benchmark, i.e., ground-truth "GT". The GT solution is also used to build up uncertainty envelopes (shown as grey lines) as $d_{CPA,horGT} \pm \sigma_{dCPA,hor}$ and $d_{CPA,vertGT} \pm \sigma_{dCPA,vert}$ for the horizontal and vertical components of the distance at closest point of approach, respectively. To better highlight parts of the encounters which appear to be more interesting in a DAA perspective, the evolution in time of the components shown in Figure 6.11 is limited to values of t_{CPA}<50 s. As it can be noticed, the estimated horizontal and vertical $\mathbf{d}_{\mathrm{CPA}}$ components are well contained within the boundaries of their uncertainty envelopes,

thus proving a satisfactory estimation. This condition is briefly not satisfied for the horizontal component during F1E3 (Figure 6.11 bottom, time≈485 s and time≈510 s) due to the occurrence of missed frames, thus camera dropouts, which cause a local increase in angular rates errors due to the exploitation of RADAR-only measurements within the EKF. The dependence of $\mathbf{d}_{CPA}$ on the angular rates estimates in near-collision conditions (Eq. (3.5)) is therefore here observed on an experimental basis. From Eq. (3.5), it is clear that larger distances act as an amplified of the effect of angular rates (due to the squared dependence on range) thus causing higher estimation errors, as visible in Figure 6.12 where the errors (Δ) of estimates with respect to the benchmark are reported. Here, the lines highlighted in green represent errors for t_{CPA}<50 s. Similar considerations can be made on t_{CPA} which, however, in near-collision conditions does not depend on the angular rates. In the case F1E3 a strong increase in the t_{CPA} error is observed during the last 2 seconds of the encounter. This is due to a sudden deceleration of the UAV (estimated $\dot{r}$ reaching 0 m/s) occurring at short distance (r<80 m). Error statistics are reported in terms of RMS values in Table 6.3 while Table 6.4 provides the same values but achieved exploiting the standalone RADAR tracker detailed in section 5.3. The comparison between the performance shows the benefits achieved using a fused solution not only at tracking level but also for conflict detection. The lower tracking performance achieved by the standalone RADAR EKF is reflected in a larger errors in $d_{CPA,hor}$ and $d_{CPA,vert}$. Instead, similar conflict assessment performance in terms of t_{CPA} is achieved since visual/RADAR fusion does not allow improving range and range rate estimates at tracking level.

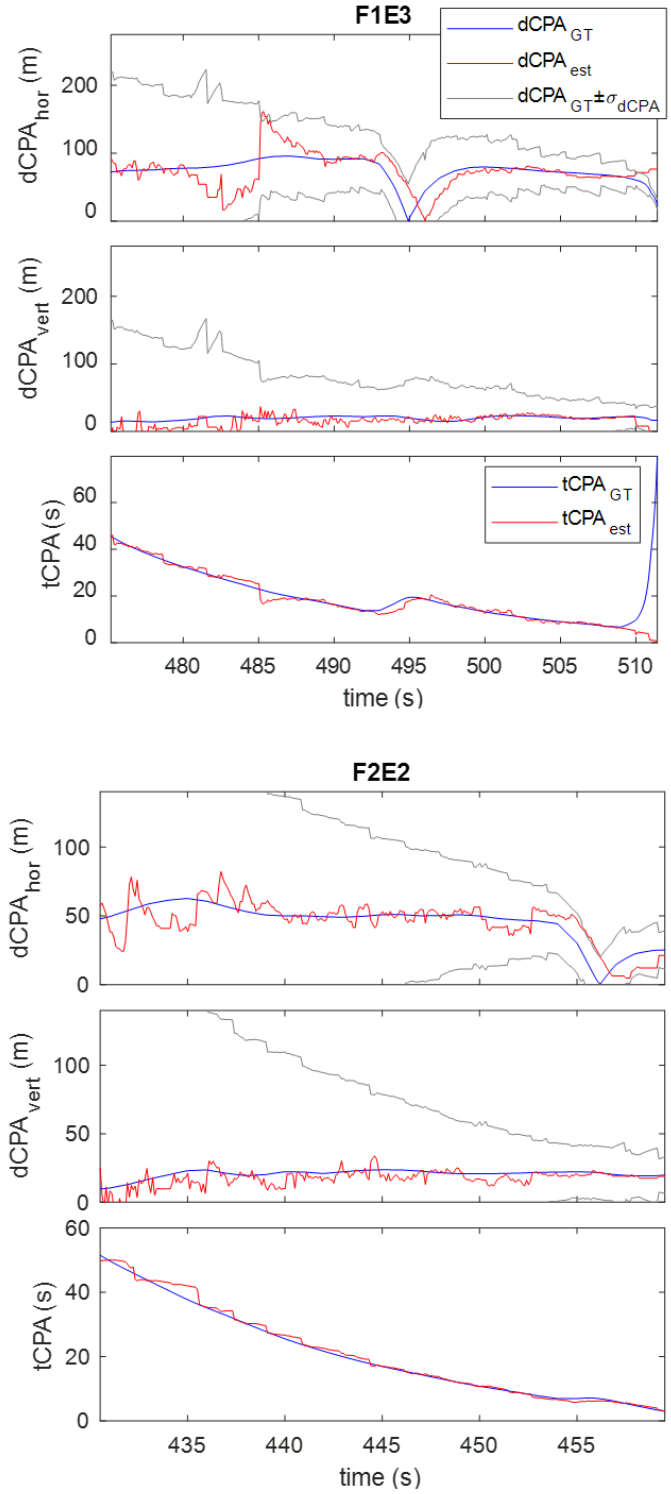

Figure 6.11 Results of the estimation of horizontal and vertical components of the distance at closest point of approach and time to closest point of approach (red lines) shown along with their reference ground truth solution (blue line). Cases F1E3 (top) and F2E2 (bottom). Dataset 2.

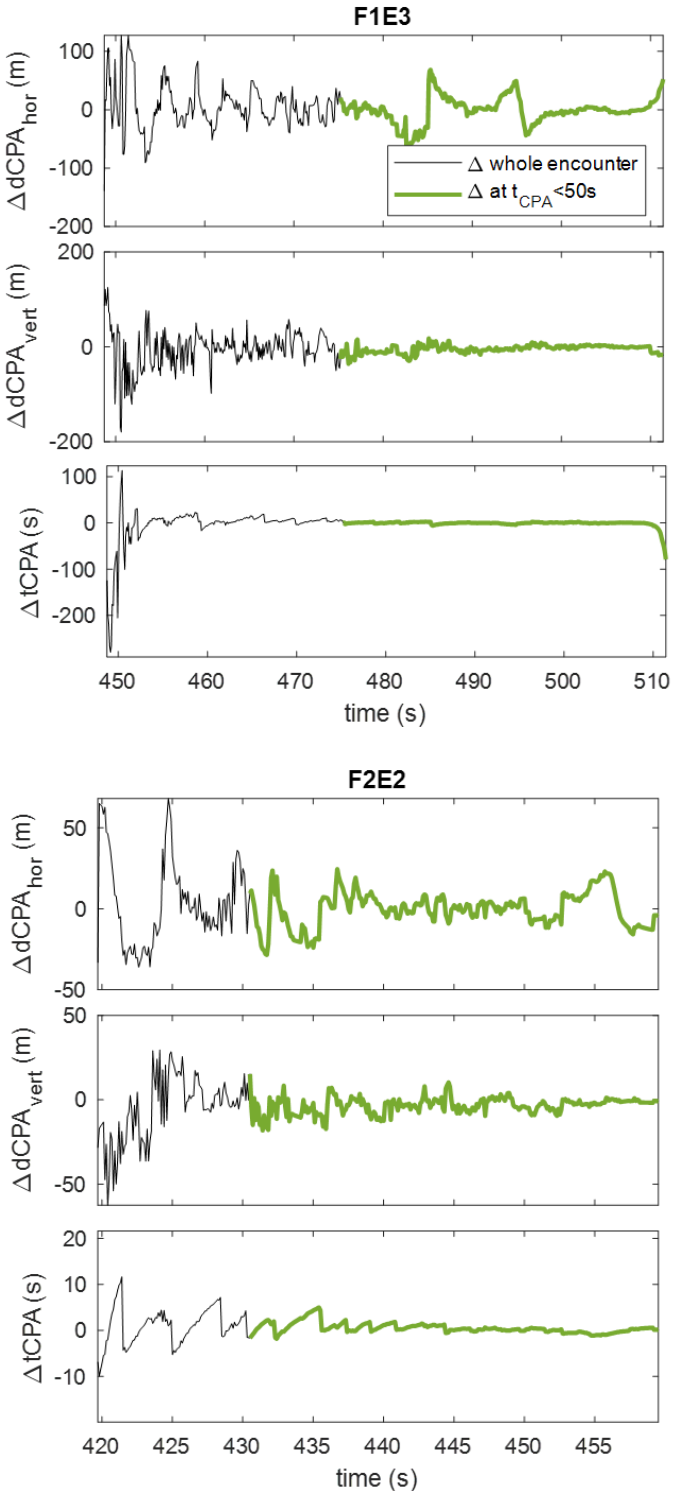

Figure 6.12 Errors in the horizontal and vertical components of the distance at closest point of approach and time to closest point of approach with respect to the ground truth. Green lines represent errors when tCPA<50 s. Cases F1E3 (top) and F2E2 (bottom). Dataset 2.

Table 6.3 Rms for conflict detection analysis using the fused visual/RADAR tracker with FBT strategy.

Case	rms $\Delta d_{CPA,hor}$ (m)	rms $\Delta d_{CPA,vert}$ (m)	rms Δt_{CPA} (s)
F1E1	6.84	10.72	0.96
F1E2	5.15	9.77	0.97
F1E3	22.29	9.34	1.43
F2E1	4.99	8.65	1.28
F2E2	10.52	5.82	1.21

Table 6.4 Rms for conflict detection analysis using standalone RADAR tracking strategy.

Case	rms $\Delta d_{CPA,hor}$ (m)	rms $\Delta d_{CPA,vert}$ (m)	rms Δt_{CPA} (s)
F1E1	20.34	22.12	0.89
F1E2	9.12	18.55	0.75
F1E3	29.76	25.07	7.64
F2E1	10.59	21.51	1,84
F2E2	17.18	19.26	1.92

6.4.3 Track-to-Track Fusion Results

The T2TF strategy is tested once again on data from dataset 2. In this case three encounter are considered: F1E1, F1E2 and F2E2 (following the nomenclature used for the discussion of the FBT strategy results). Specifically, the latter two encounters are chosen as they show the higher variation in range, with maximum range at the beginning of the encounter of the order of 500 meters. Since the local trackers exploit the standalone visual- and RADAR-based tracking solution, the settings used are the same as those presented in Chapter 5 with both trackers exploiting a sampling time T=0.1 s. In the visual case, the settings involve S=0.4, $\tau_{tr,gen}$=5 pixels. In the RADAR case, the threshold $\xi_{RAD,th}$=13.28 is used for association, instead. For the sake of brevity, performance are reported for one case only (F1E2) in Figure 6.13 where the output from each LT, RADAR (RAD_{FT}) in green, and visual (VIS_{FT}) in red, along with the results of their fusion ($FUSED_{FT}$) and the reference CDGNSS benchmark depicted in black and blue, respectively. Specifically, the output from local RADAR tracker and fusion center are shown in spherical coordinates (with range rate) by means of cartesian-to-spherical transformation. The first track to be generated among the three is the RADAR one, achieving declaration range of 530 m, this is reduced to 500 m for the visual track (as inferred from the CDGNSS benchmark). The fused track also demonstrates the same

declaration range as the visual, this is due to the fact that the strategy is modelled to attempt fusion when firm tracks from both sensors are available. Therefore, right after the generation of the visual track, which is delayed with respect to the RADAR one, a fused track is also generated, thus witnessing successful T2T association with the models described in section 6.3. Once again, as also verified with the other fusion strategies, accuracy with respect to the benchmark is settled on sub-degree and meter-level values for angular and distance estimates. RMS and declaration ranges (r_{FT}) are reported in Table 6.5.

Table 6.5 Dataset 2 - Flight 1 – Encounter 2. Performance statistics for fused visual/RADAR tracker with T2T strategy.

Case	r error (m)	$\dot{r}$ error (m/s)	az error (°)	$a\dot{z}$ error (°/s)	el error (°)	$e\dot{l}$ error (°/s)	r_{FT} (m)
F1E1	1.8	0.6	0.3	0.04	0.04	0.07	422
F1E2	1.8	0.3	0.3	0.07	0.4	0.06	500
F2E1	2.2	0.6	0.3	0.04	0.5	0.06	500

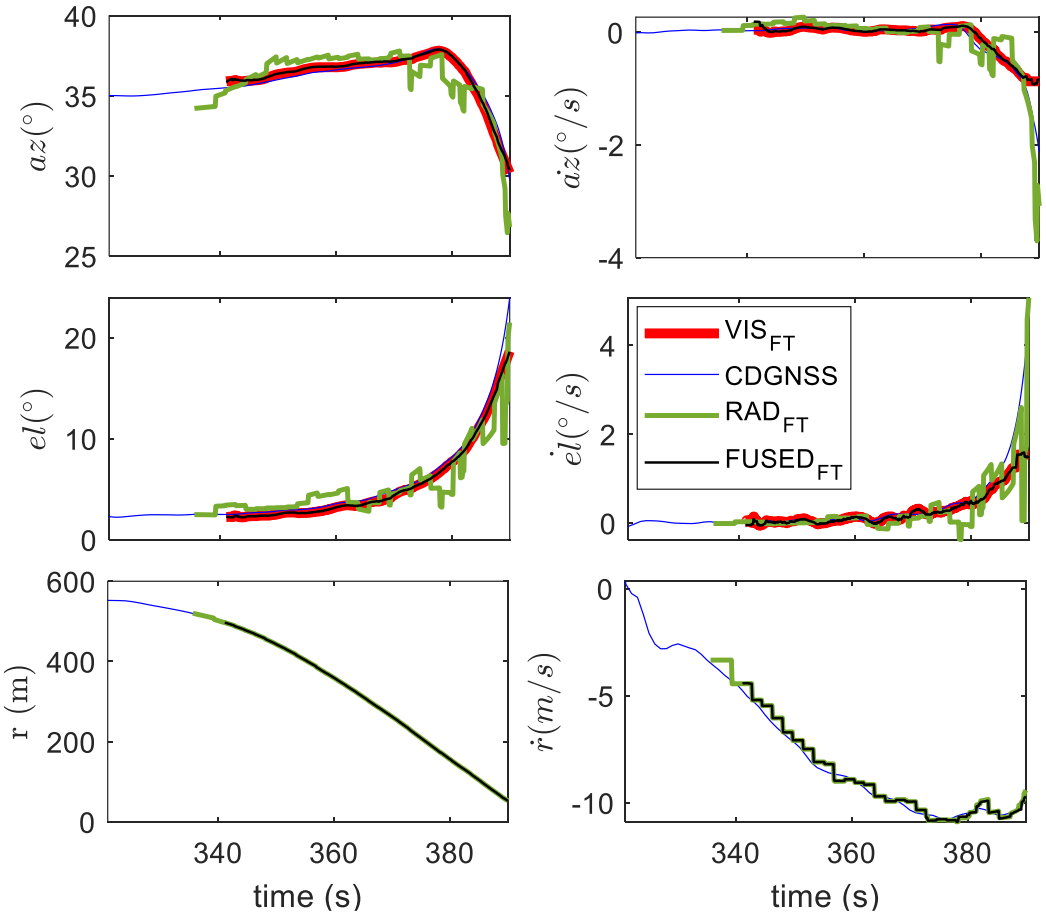

Figure 6.13 Case F1E2, dataset 2. Tracking results of the T2TF strategy with output from RADAR local tracker (green), visual local tracker with DL measurements (red) and fusion center (black) along with CDGNSS benchmark (blue).

Chapter 7: Benchmarking and Distributed Sensing

In the context of AAM/UAM a critical asset is the design and testing of surveillance strategies which will enable the safe operations of novel aircraft type, both sUAVs and eVTOLs, in and around urban areas. Compared to the well-assessed manned aviation systems scenarios, surveillance strategies in this environment need to detect smaller platforms flying at lower altitude against cluttered backgrounds in dense airspace. While a strong link there exists with the design of DAA strategies, which need to cope with the same challenges, in the vertical context of AAM/UAM major attention is being reserved to the development of distributed sensing strategies to support the expected large volumes of autonomous operations in the airspace. The concept is analogous to ground vehicles traffic surveillance solutions and envisions the use of multiple, interconnected sensing nodes to be placed, ideally, at regular intervals along flight corridors and with higher density around critical areas such as vertiports [124]. This idea is conceptually presented in Figure 7.1. In this context, attention must be allocated to the design of tracking strategies which account for information retrieved in very different locations and at different rates, with initial tests only carried out in simulation environments [125], [126]. The exploitation of a network of sensors to collect information on sUAV is an active area of research in the initial stages of investigation. In these regards, the NASA Revolutionary Aviation Mobility (RAM) subproject of the Transformational Tools and Technology (TTT) project is researching the development of distributed sensing architecture for UAM and sUAVs in the AAM context [27] with research works such as [97], [127], [128] aiming at developing sensing strategies for sUAVs observed by ground-based networks of distributed sensors.

This chapter is focused on this research thread and proposes sensing strategies for UAM/AAM surveillance tested on field data collected during joint experimental activities between the University of Naples “Federico II” and the NASA Langley Research center. The activities result from the conjunction of the TTT and AAM NASA projects and involved the collection of data during flight operations of the

High Density Vertiplex (HDV) subproject [129] which aimed at demonstrating autonomous BVLOS flights of multiple sUAVs, thus simulating a realistic future air traffic environment within UAM/AAM and enabling the collection of relevant data for the design of surveillance strategies. Specifically, data were collected using a network of three ground-based sensing nodes, equipped with RADARs and visual cameras, as well as an airborne node (included as an additional surveillance agent).

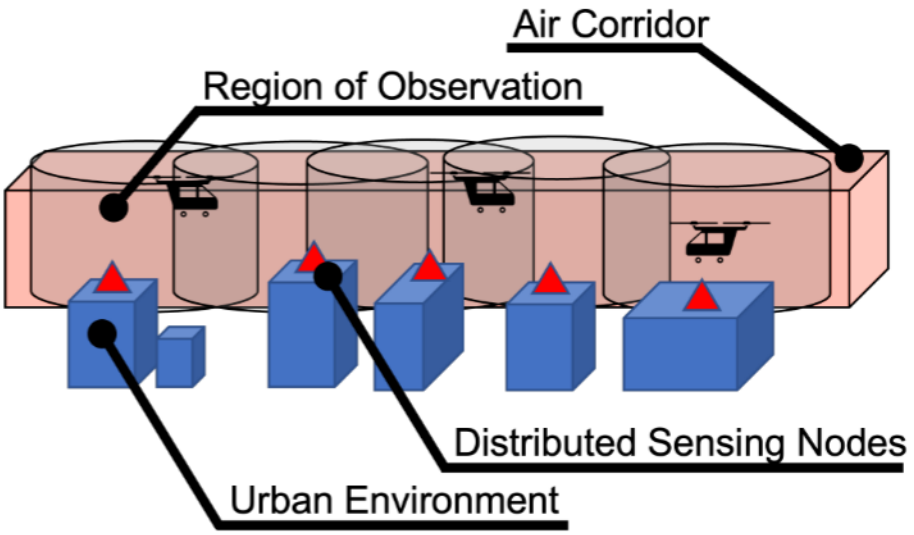

Figure 7.1 Graphical representation of the concept of distributed sensing for air corridor surveillance [124].

As a contribution towards the assessment of the performance of such nodes for the surveillance of low-altitude flying sUAVs, a first analysis is here proposed to benchmark sensing solutions exploiting standalone sensor information only. In this case, data collected with two ground-nodes in the same location and operating in similar way are used. This analysis is crucial to evaluate the feasibility of exploiting (and adapting) the already existing strategies in a scenario where multiple sUAVs are used and the external environment is different from the typically tested one.

Then, a sensor fusion strategy exploiting the information from the multiple RADARs is proposed. In this case, the standalone RADAR tracking logic (whose details are provided in section 5.3) runs on each node independently to retrieve firm tracks of all flying objects. The fusion of these pieces of information is then performed by exploiting a “leader-helper” strategy where the leader RADAR is the first to generate a firm track and exploits measurements from the helper to increase the lifespan of its tracks, thus improving track coverage. An additional analysis

focusing on RADAR interference phenomena, occurring when multiple RADARs operate with overlapping FOVs is also performed. The latter focuses on a preliminary interference removal strategy to enable tracking, which would otherwise be hindered by the large amount of unwanted RADAR data.

The chapter is structured as follows. Details on the experimental activities and data used for the analyses are provided in section 7.1. The benchmarking of different sensing strategies based on visual-only and RADAR-only information is discussed in section 7.2, while the fusion solution for the distributed network of ground-based RADARs is proposed in section 7.3. In the latter, the interference removal strategy is also presented. Experimental results arising from the application of these strategies to the collected data are discussed in section 7.4.

7.1 EXPERIMENTAL ACTIVITIES

The work carried out for the distributed sensing research thread exploits data collected over two months of experimental activities carried out at the NASA Langley City Environment Range Testing for Autonomous Integrated Navigation (CERTAIN) flight space [130] during HDV flights. Data were captured by exploiting three ground-based nodes and one aerial node, each of which is equipped with one Echoflight MESA RADAR, at least one global shutter visual camera and a uBlox F9P GNSS receiver with coupled antenna. During tests, nodes were mounted in different locations, thus capturing data from different perspectives. This is shown on the satellite map in Figure 7.2 where such locations are highlighted. Specifically, each node, shown in Figure 7.3 during tests, is labelled taking the name from its location; the gantry node was mounted to the Landing and Impact Research Facility (LIRF) structure (also known as gantry) approximately 60 meters above ground; the wythe creek node was mounted on a deployable tripod at the intersection with the wythe creek road; the rooftop node was also mounted on a deployable tripod located on top of a building's rooftop approximately 10 meters above ground. The experimental activities enabled the generation of a 25-Terabytes dataset containing RADAR, visual and GNSS information collected during nine days of flight tests where a varying number of sUAVs (up to 5) where flown simultaneously. The trajectories followed by such platforms also varied. However, in the cases considered

for this manuscript, only the loop-like trajectory shown in purple in Figure 7.2 was covered. Further details on the activities can be found in [131].

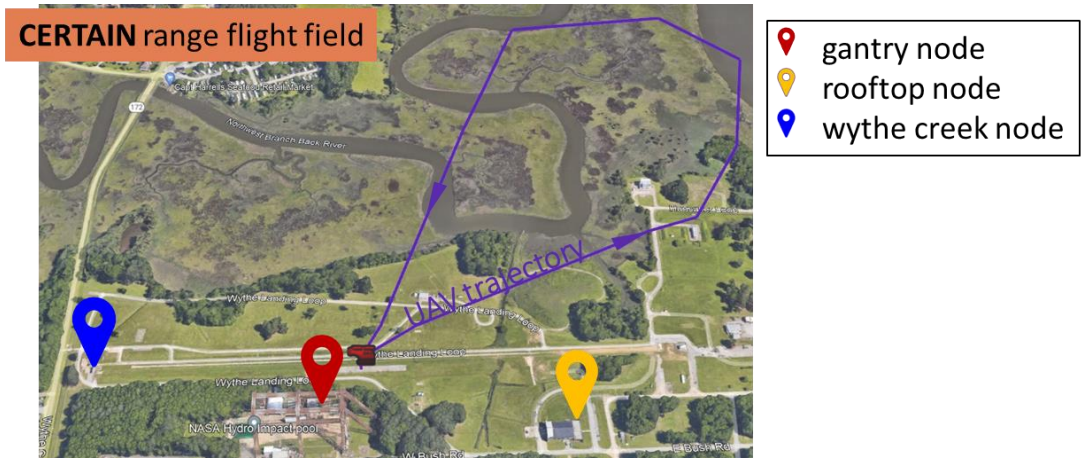

Figure 7.2 Satellite map of the CERTAIN flight field at NASA Langley showing location of ground nodes and trajectory of sUAV.

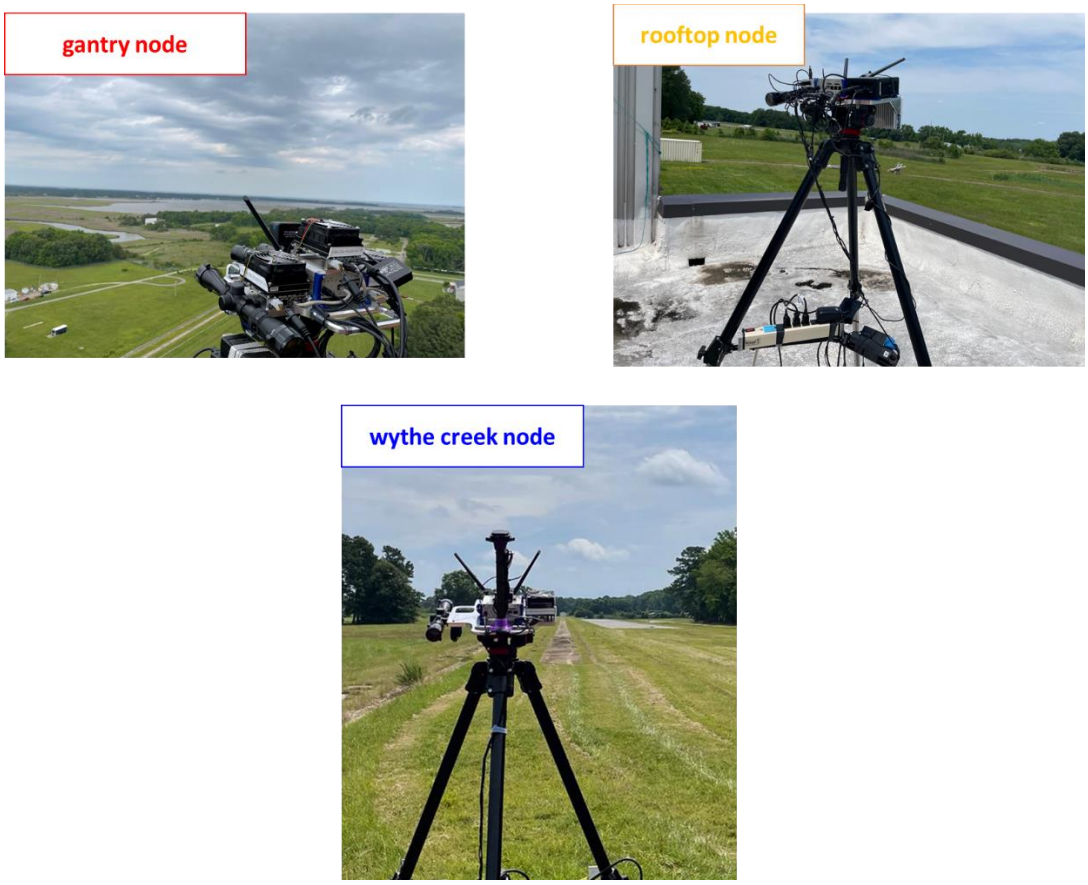

Figure 7.3 Ground nodes in their respective mounting locations during experimental activities.

7.1.1 Ground-based setup

Each of the ground node is equipped approximately with the same hardware, shown in Figure 7.4 for the rooftop node, taken as example. The processing units

(CPU), to which each sensor is connected, responsible for data acquisition and logging, range from AMD-64 architecture (rooftop node equipped with Intel NUC 11th generation, i7 processor) to ARM architectures (other nodes equipped with NVIDIA Jetson AGX Xavier boards). All the visual cameras have the same resolution, generating images with dimensions of 4096x3000 pixels. The FOV of the cameras are about 62°x48° in the case of rooftop and wythe creek node, while the gantry node mounts three different cameras with smaller FOV each (47°x36°), to achieve a higher coverage. As far as frequency is concerned, cameras acquired frames at 15 Hz, which was lowered to 10 Hz in the rooftop case. All nodes are also equipped with cellular routers which enable their remote control.

Differently from the tests described in section 4.1, the Echoflight RADAR was used operating in "search-while-track" which makes it possible to retrieve measurements from an intelligent scan of its FOV. When operating with this mode, the RADAR frequently interrupts the grid FOV scanning pattern to revisit areas where objects were detected, thus collecting more data of interest which is output at a frequency of 10 Hz. An additional advantageous aspect of this operative mode is the reduction in the complexity of the centroiding procedure, which will cope with a lower number of measurements. The FOVs of the RADARs were set accordingly to the environment surrounding their mounting location. Thus, in the wythe creek case a 60° horizontal FOV was chosen to avoid the inclusion of detections from the surrounding tree lines, while in the rooftop and gantry cases, the whole horizontal extension of 120° was used, instead. The gantry was the only location where the RADAR operated using the whole extension in the vertical direction (80°), while this was halved (about 40°) to avoid ground echoes in the rooftop and wythe creek cases.

On a software level, all nodes share the same acquisition software (briefly described in section 4.1) except for the rooftop node which utilizes the Robot Operating System (ROS) environment with a customized launch file.

The configuration shown in Figure 7.2 and Figure 7.3 was used during most tests. However, the first tests were performed to tackle the collection of data for the benchmarking of the different sensing strategies. Therefore, the rooftop and wythe creek nodes were located both at the wythe creek location and used with the RADARs operating in the same conditions, thus enabling a common basis for the

assessment of the strategies. To avoid confusions, in this case nodes will be referred to as “node 1” (wythe creek) and “node 2” (rooftop). A snapshot from the benchmarking experiments is shown in Figure 7.5. In this case, the FOV of both RADARs was set to 60° x 40° in the horizontal and vertical directions (thus being comparable to the FOV of the cameras).

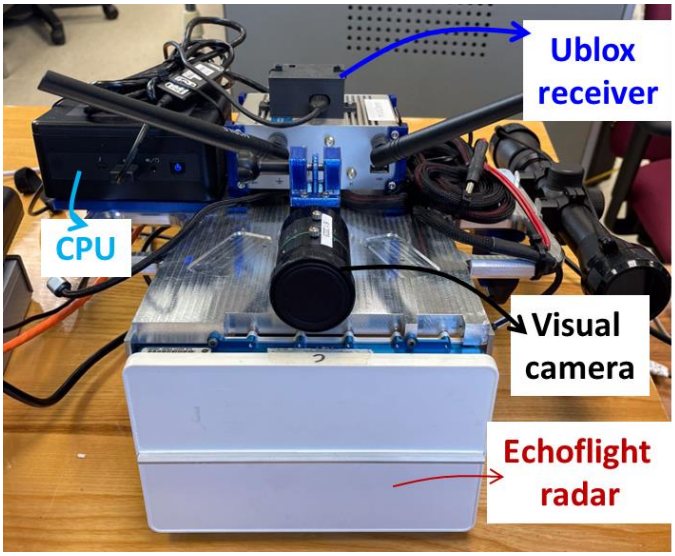

Figure 7.4 Hardware on rooftop node, GNSS antenna not shown.

Figure 7.5 Nodes during acquisition of data for the benchmarking of sensing strategies.

7.1.2 Flight scenario

The platforms used as targets for the sensing strategies are Alta-8 sUAVs from Freefly. These are shown both on their vertiports before and during flight (as captured from the gantry location) in Figure 7.6 left and right, respectively. When unfolded, these platforms can reach a maximum dimension of about 1.5 meters. The

flight scenarios considered in the following analyses are different as different datasets are used.

During the flight day when data for the benchmarking analyses were collected, four Alta-8 were flown simultaneously on the loop-like trajectory shown in Figure 7.2. A temporal separation between the departures of the platforms was used; after the first vehicle's take-off ('N556NU'), the second ('N557NU') and third ('N559NU') followed with a one-minute delay, while the fourth ('N561NU') was the last to depart with a 2-minutes separation from the previous. During the loop, the vehicles transversed a total distance of about 2 kilometres, reaching a maximum distance from the nodes located at wythe creek of about 1.2 kilometres and a maximum height of about 80 meters.

The data on which the distributed RADAR fusion strategy is tested were collected during the fligth day of two Alta-8 which also performed the loop-like trajectory. This is shown in the 3D representation of Figure 7.7 where the true trajectory (from onboard GNSS logs) is depicted along with the location of the RADARs (and respective nodes). In this case, the first sUAV to depart was 'N556NU', followed by 'N561NU'.

Figure 7.6 Left: sUAVs in their vertipads prior to take-off. Right: sUAVs during flight captured from gantry location. Location of vehicles is indicated with red arrows.

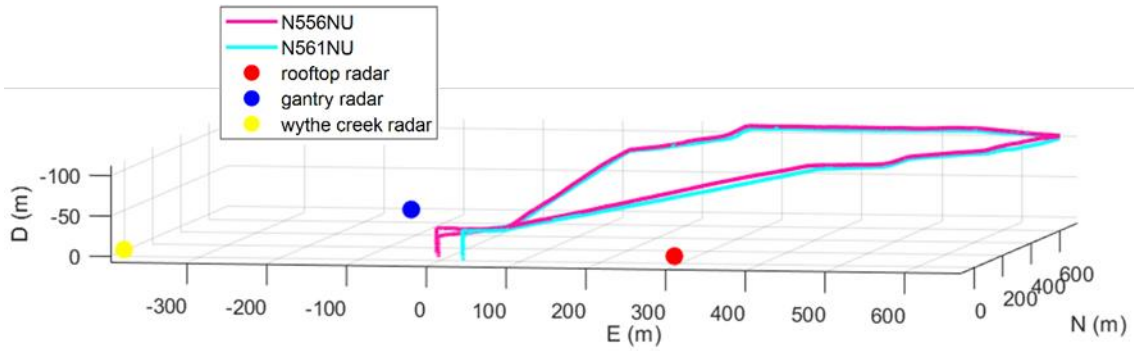

Figure 7.7 3D trajectory in NED of sUAVs flown during the acquisition of data on which the distributed RADAR fusion strategy is tested. Location of RADARs (hence respective nodes is also shown). For sake of clarity, the vertical axis direction is reversed.

7.2 BENCHMARKING OF SENSING STRATEGIES

The purpose of the benchmarking analysis is to highlight differences in the performance of visual-based and RADAR-based solutions using two nodes with similar architecture and located in the same spot, thus having the same view over the flight of the sUAVs. In the RADAR case, the built-in RADAR tracker with which the Echoflight device is equipped is used on node 1 as a mean of comparison with the customized EKF strategy (section 5.3 of this manuscript) adopted on the data collected by node 2, instead. However, due to the highly cluttered environment, more challenging with respect to the one tested in the previous experiments (section 4.3), additional filtering is applied on the RADAR data. Specifically, given the availability of the RADAR Cross Section (RCS) measurement, the condition RCS>$RCS_{th,up}$ and RCS<$RCS_{th,low}$ are used to filter out unwanted data using the thresholds $RCS_{th,up}$ and $RCS_{th,low}$ according to the typical RCS signature of sUAVs. Centroiding can then be applied to merge clusters, though reduced in density. Clusters are thus identified and merged (by averaging their measurements) if their difference in range, azimuth and elevation is smaller than δr, δaz and δel, respectively.

As far as the visual strategy is concerned, two different customized strategies are exploited.

7.2.1 Visual-based sensing strategy on node 1

The visual detection and tracking pipeline on node 1 is an extension of the methodology developed in [132] and uses a detection strategy combining temporal detection, with an image differencing technique, and spatial detection, with morphological filtering exploiting a 5 by 5 cross-shaped kernel. The tracker uses a

linear KF exploiting the Munkres algorithm [133] for measurement-to-track association. Specifically, a track can potentially be established if successful association is verified with no more than N_{fail} consecutive dropouts (or fails) over N_{frames}. An additional criterion is also added on the total number of associations successfully performed (N_{hits}) within the N_{frames} batch, thus effectively establishing a firm track if the ratio N_{hits}/N_{frames} is greater than or equal to a threshold (vis_{th}). This latter threshold is also used to decide upon the deletion of an already established track which is therefore performed if $(N_{hits}/N_{age}) \leq vis_{th}$, where N_{age} is the number of frames representing the age (or length) of the track. An age requirement parameter, $N_{req,\text{age}}$, sets the minimum amount of updates prior for a track being deleted with the vis_{th} criteria.

7.2.2 Visual-based sensing strategy on node 2

The tracking pipeline already presented in section 5.2 is exploited on node 2 with minor modifications, mostly applied on the detection level. In this case, in fact, only the morphological filtering strategy with the combination of top and bottom hat is used. Thus, the detections are looked for in the portion of the image above the horizon line which, in this case, also accounts for the presence of the tree line and other fixed obstacles within the FOV. Once found, detections are passed over to the tracker where association is verified using the Euclidean distance criterion (Eq. (5.4)) with threshold $\tau_{tr,gen}$. Given the high presence of fast-moving targets such as birds, this latter threshold is lowered with respect to the previously analysed cases. Nevertheless, this choice promotes a challenging condition for the preservation of firm tracks in cases when the sUAVs accelerate. Given the highly varying relative geometries covered during their flight with respect to the camera, a too low value of $\tau_{tr,gen}$ used at firm tracking can easily generate track interruptions. To avoid this, once a firm track is generated, the association condition is relaxed and shifted to the verification of the presence of measurements within a window centered at the track prediction (with fixed dimensions of nxm pixels).

7.3 DISTRIBUTED RADARS FUSION STRATEGY

7.3.1 Interference removal

RADAR data used for the proposed distributed sensing strategy is affected by the presence of clutter which arises from fixed objects (such as the ground or near-by buildings, for instance) in terms of direct or indirect, i.e., multipath, reflections, as well as from internal, device-driven phenomena. As in all other cases analysed so far, clutter can be removed by applying Doppler thresholds to discard measurements from ground and fixed echoes and RCS-based thresholds (as previously mentioned in section 7.2). If a priori knowledge on the environment is also available, additional thresholds can be set on the range, azimuth and elevation measurements, thus effectively reducing the area under surveillance in a post-processing fashion. Clustering of measurements from the same objects can then be applied as described in the previous section.

Unfortunately, the application of these filters is not enough to prevent the collection of outliers due to interference phenomena deriving from the partial overlap between the FOVs of RADARs in the distributed sensing network. If unmitigated, RADAR interference can degrade the quality of the data passed over to the tracker by generating excessive number of false tracks and lose information relevant to the targets of interest (i.e., the sUAVs). The interference phenomenon, which affects one of the two RADARs exploited in this work, is observed in terms of a large number of detections retrieved in the same RADAR beam (same values of *az* and *el* which define the center of the beam) and showing wide variations in *r*, *RCS* and $\dot{r}$. The retrieval of multiple detections in the same beam, thus at the same pointing direction, is a common occurrence for electronically-scanning array RADARs and results from the physical dimensions of the beam, which determines the angular accuracy of the RADAR. Still, when interference takes place, this phenomenon is enormously enhanced due to the reception of signals emitted by other RADARs. Such signals are received by the RADAR which translates them into range measurements due to their shift in frequency. The proposed filtering procedure leverages on the variability of the range measurements retrieved in the same beam. Specifically, the method detects interference when, at a given *az-el* pointing direction, a set of more than two detections show a standard deviation in their range measurements which is larger

than a threshold $r_{\sigma th}$. The value selected for $r_{\sigma th}$ (along with all the other setting parameters) is detailed in the results section.

7.3.2 Fusion approach

A flow diagram of the proposed RADAR fusion strategy is shown in Figure 7.8. In the following discussion, the subscript k is used to refer to the different RADARs within the distributed architecture, either acting as leader, l, or as helper, h. Each RADAR tracker exploits the model presented in section 5.3 to estimate the state of all detected objects defined as, $\mathbf{x}_k=[x_k,y_k,z_k,\dot{x}_k,\dot{y}_k,\dot{z}_k]^{NED}$, thus containing the components of the relative position and velocity vectors of the tracked object with respect to the RADAR in NED reference frame centered at the RADAR location. The measurement vector is defined as $\mathbf{z}_k=[r_k,az_k,el_k,\dot{r}_k]^{NED}$, which contains filtered measurements rotated in NED exploiting the knowledge of the RRF-to-NED rotation matrix ($M_{r,k}^{n,k}$).

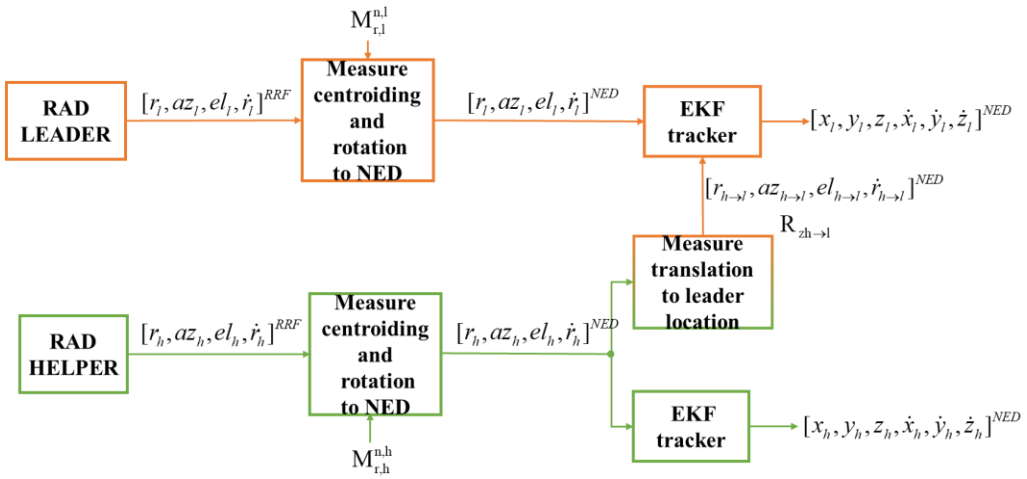

Figure 7.8 Flow diagram of the distributed RADAR strategy.

The tracking procedure is independently performed by the two RADARs, however, when the first firm track is generated by either of the two, the generating RADAR is elected as leader while the other is considered as a helper, instead. Assuming that a data link between the RADARs can be established, the leader tracker will then start using the helper's measurements whenever one of its generated firm tracks is at risk of being deleted. Therefore, in the leader case, a further measurement-to-track association, with respect to the one carried out on its own measurement, is attempted to extend its soon-to-end firm tracks based on the helper's

measurements. Specifically, such measurements are injected in the leader's tracker when one of its firm tracks verifies the condition $dt_{FT}/2 \leq dt_{pred} \leq dt_{FT}$. Here, dt_{pred} is the time elapsed from the last correction and dt_{FT} is the time threshold which promotes deletion if $dt_{pred} > dt_{FT}$. Measurements collected by the helper RADAR are referred to the NED reference which is centered at its location ($\mathbf{X}_h=[X_h,Y_h,Z_h]$), rather than the leader one ($\mathbf{X}_l=[X_l,Y_l,Z_l]$). Therefore, a translational transform must be applied to the helper's measurements within the leader EKF. To this aim, first, the relationship $\mathbf{x}_h=g(\mathbf{z}_h)$, transforming the spherical measurement (contained in the vector $\mathbf{z}_h$) in a cartesian measurement (contained in the vector $\mathbf{x}_h$) through the non-linear function g, shown in Eq. (7.1), is applied.

$$\begin{bmatrix} x_h \\ y_h \\ z_h \\ \dot{x}_h \\ \dot{y}_h \\ \dot{z}_h \end{bmatrix} = \begin{bmatrix} r_h \cos(az_h)\cos(el_h) \\ r_h \sin(az_h)\cos(el_h) \\ -r_h \sin(el_h) \\ \dot{r}_h \cos(az_h)\cos(el_h) \\ \dot{r}_h \sin(az_h)\cos(el_h) \\ -\dot{r}_h \sin(el_h) \end{bmatrix} \tag{7.1}$$

Then, the measurement vector in cartesian coordinates is translated to the leader's location ($\mathbf{x}_{h\to l}$) using the relationship $\mathbf{x}_{h\to l}=\mathbf{x}_h+\mathbf{\Delta X}$ where $\mathbf{\Delta X}=[X_h-X_l,Y_h-Yl,Zh-Z_l,0,0,0]$ is the vector containing the relative position and velocity of the helper location with respect to the leader one. The relative velocity components listed in $\mathbf{\Delta X}$ are all equal to zero m/s due to the fixed location of the two devices. Once translated, the measurement vector can be converted back to spherical coordinates by exploiting the relationship $\mathbf{z}_{h\to l}=h(\mathbf{x}_{h\to l})$, as shown in Eq. (7.2).

$$\begin{bmatrix} r_{h\to l} \\ az_{h\to l} \\ el_{h\to l} \\ \dot{r}_{h\to l} \end{bmatrix} = \begin{bmatrix} \sqrt{x_{h\to l}^2 + y_{h\to l}^2 + z_{h\to l}^2} \\ \tan^{-1}\left(\dfrac{y_{h\to l}}{x_{h\to l}}\right) \\ -\sin^{-1}\left(\dfrac{z_{h\to l}}{\sqrt{x_{h\to l}^2 + y_{h\to l}^2 + z_{h\to l}^2}}\right) \\ \dfrac{x_{h\to l}\dot{x}_{h\to l} + y_{h\to l}\dot{y}_{h\to l} + z_{h\to l}\dot{z}_{h\to l}}{\sqrt{x_{h\to l}^2 + y_{h\to l}^2 + z_{h\to l}^2}} \end{bmatrix} \tag{7.2}$$

This coordinate system transformation introduces an additional uncertainty in the helper RADAR measurement. Such uncertainty is related to the errors in the GNSS-based-localization of both devices whose information is contained in the matrix Σ_{GNSS} of Eq. (7.3) where the covariances (σ) arising from the GNSS measurements along each direction are listed in the matrix Σ_{POS} while matrix Σ_{VEL} contains all null elements, instead.

$$\Sigma_{GNSS}=\begin{bmatrix}\Sigma_{POS} & O\\ O & \Sigma_{VEL}\end{bmatrix};\Sigma_{POS}=\begin{bmatrix}\sigma_{x,h}^2+\sigma_{x,l}^2 & 0 & 0\\ 0 & \sigma_{y,h}^2+\sigma_{y,l}^2 & 0\\ 0 & 0 & \sigma_{z,h}^2+\sigma_{z,l}^2\end{bmatrix} \quad (7.3)$$

When measurements from the helper are passed over to the leader RADAR, the increasing covariance effect needs to be accounted for. To do so the measurement covariance matrix ($R_{zh\rightarrow l}$), associated with the $\mathbf{z}_{h\rightarrow l}$ vector, is computed. Firstly, the helper RADAR measurement covariance matrix (R_{zh}) is transformed in its cartesian expression (R_{xh}) exploiting the relationship $R_{xh}=DR_{zh}D^T$, where the matrix D is the Jacobian of the spherical-to-cartesian transformation, obtained from derivation of Eq. (7.1). Then, the matrix $R_{xh\rightarrow l}$, representing the uncertainty in cartesian coordinates of the helper measurement translated to the leader location, can be computed as $R_{xh\rightarrow l}=R_{xh}+\Sigma_{GNSS}$, and it can then be transformed into a spherically-expressed matrix exploiting the relationship $R_{zh\rightarrow l}=HR_{zh\rightarrow l}H^T$. Here, H is the jacobian of the spherical-to-cartesian transformation, obtained from derivation of Eq. (7.2).

7.4 EXPERIMENTAL RESULTS

7.4.1 Benchmarking results

7.4.1.1 RADAR-based

Figure 7.9 left and right show the results of RADAR tracking on node 2 and 1, respectively. On the former, filtering of data is performed using the values $\dot{r}_{th,low}$=1.8 m/s, $RCS_{th,up}$=0 dBsm and $RCS_{th,low}$=-25 dBsm while only measurements corresponding to ranges between 350 m and 1200 m are considered. The results are shown both in terms of firm tracks of the different sUAVs and their respective benchmark ("GT") achieved by processing the onboard GNSS absolute position logged by their autopilot. For the sake of brevity, sUAVs are reported as numbered

from 1 to 4 following their take-off sequence. Tracks whose nature is uncertain are labelled as “other”.

The results on node 2 highlight the suitability of the tracker in maintaining multiple tracks of different objects, thus demonstrating its multi-target nature. The performance analyses are carried out by dividing the flight phases in departure (moving away from the sensors) and arrival (moving back to the vertiports). Average times at which tracks are generated reach values of 41 s and 13 s from first appearance of sUAVs in the RADAR FOV during departure and arrival, respectively. Such difference between the two phases can be explained with a higher number of valid RADAR measurements found when the UAVs are coming back from their loop, as a result of lower ground clutter presence. However, a higher departure flight coverage is achieved, leading to maximum ranges at firm track of about 1200 meters in all cases. Track coverage can be computed by evaluating the presence of a firm track and GNSS benchmark of the object (also accounting for the FOVs boundaries) at each time instant. The achieved results show departure coverage comprised within 69% and 89% and arrival coverages comprised within 49% and 56% for the four targets. The typical RADAR-based accuracy is observed by computing the error with respect to the benchmark. Thus, RMS values below 5 m on range and of the order of few degrees on angles are observed. This increase with respect to the values which were reported in previous analyses is also related to the quality of the benchmark which, in this case, is not processed with CDGNSS.

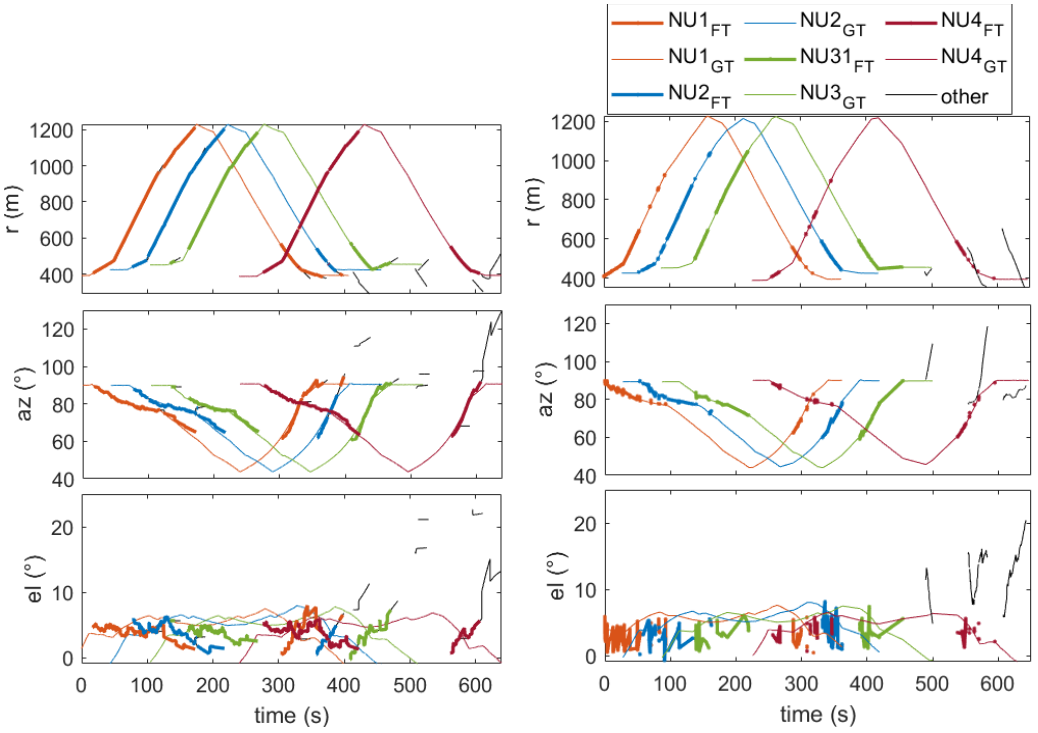

Figure 7.9 Left: Results of RADAR tracking on node 2. Right: Results of RADAR tracking on node 1.

Although measurements achieved with the two RADARs show the expected similarity, the results at tracking level witness a significant difference. Specifically, a higher occurrence of dropouts (track interruptions) can be observed on the FTs of node 1. This is likely caused by the relation between the complexity of the environment, characterized by a high clutter presence, and the settings used on the tracker, which aggravate its ability to discern objects of interest as well as perform the tracking of multiple targets simultaneously. This is especially visible during the departure of NU4, where highly frequent dropouts occur plausibly due to the arrival of the previous drones. As a consequence, 93 total tracks are obtained within 10 minutes and an average of 20 independent tracks are generated for each NU. These numbers are drastically higher than those verified in the case of node 2 where 15 different tracks are only produced during the whole process.

7.4.1.2 Visual-based

Results of the visual-based sensing strategy of node 2 are shown in Figure 7.10. Specifically, the angular estimates are shown on the left (following the same nomenclature of the RADAR case) while a collection of camera frames showing the motion of NU1 is reported on the right. The tracker utilizes $\tau_{tr,gen}$=3 pixels, n=40

pixels and m=50 pixels. The multi-object nature of the tracker is proved for the visual case too as an even larger number of tracks are kept simultaneously (many of which belong to birds) with respect to the RADAR case. However, several points of interruption can be noticed in each track. Such interruptions are to be imputed to the NUs being occluded by the tree line. This is clearly visible on the right in Figure 7.10 where a zoom over the region where the drone is located during two different time instants is included to show both the variation in its appearance during the flight and its location with respect to the horizon line (yellow line). The first frame, captured at 168 s, depicts the departure of NU1, which starts at about 5 s and evolves leftwards on the image plane (Northward in the external local reference frame). Specifically, the zoom provided at 168 s, corresponds to few seconds before NU1 disappears from the image plane, due to the occlusion from the trees on the left side of the image. In the arrival phase of the flight (bottom frame in the figure), the drone moves rightwards (Eastwards), instead, before disappearing below the horizon few seconds after 380 s (zoom on the right). During such phase, track interruptions are also caused by the transit of the drone between trees (visible in the zoom at t=310 s). Still, track coverage is proved to be higher with respect to the RADAR case, with average values for the four sUAVs around 99.92% during departure and 97.29% during arrival.

Results for node 1 are shown in Figure 7.11 where the right figure shows an example of frame with the detection of three sUAVs. On the left of Figure 7.11, the evolution of track coverage for each platform is shown with respect to varying detection threshold (maximum number of detections allowed per single frame) and $N_{req\ age}$, reported on the x axis as "NumDetect" and "Age", respectively, followed by their numerical values. Fixed thresholds of N_{fail}=5 and vis_{th}=0.6 are used. An ideal tracker optimized for multirotor small UAVs would have 100% ground truth tracker accuracy for detection threshold 5 as there are at most 4 multirotor UAVs in the FOV, however, in addition to multirotor UAVs tracks of birds are also generated and increasing the detection threshold is needed to achieve tracking coverage greater than 90%. Varying age requirement of track results in minimal change to ground truth. Increasing the age requirement threshold increases the stability of the reported tracks as they have greater history. A detection threshold of 15 with an age requirement of 30 frames provides 96.1% coverage of the four Alta 8 over departures and returns.

Thus, slightly lower performance with respect to the visual solution of node 2 are achieved.

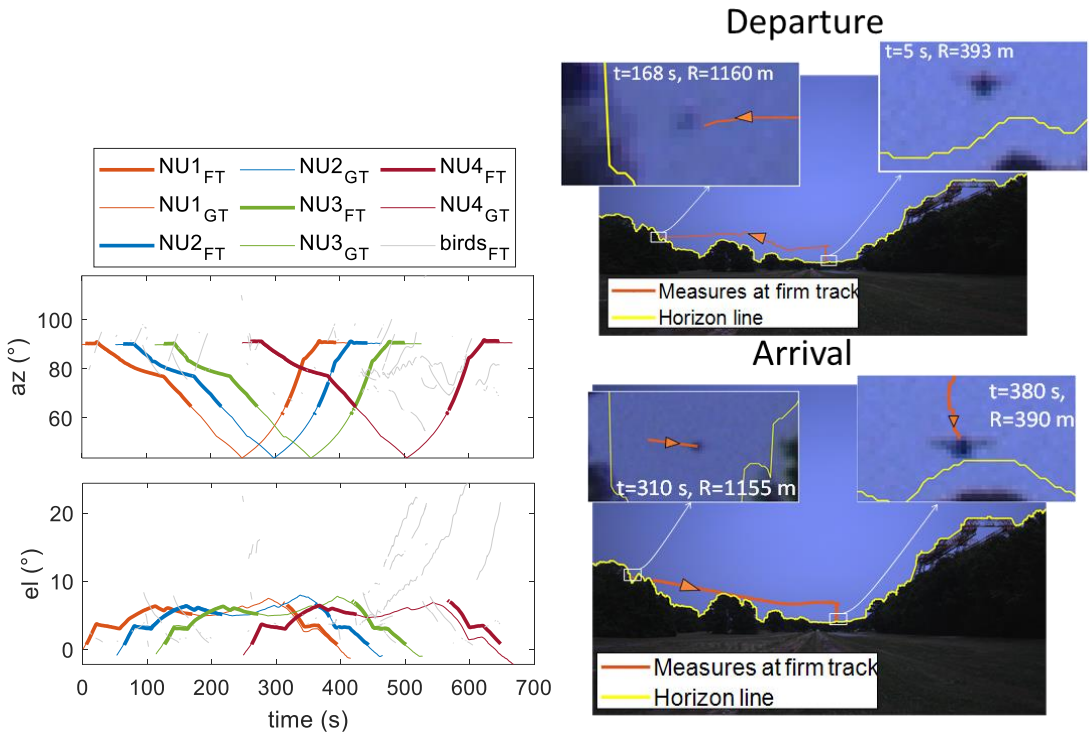

Figure 7.10 Left: Tracking results with visual camera on node 2 showing angular estimates in NED. Right: Collection of camera frames showing different flight phases of NU1. Departure (top), arrival (bottom). Horizon line, including trees, shown in yellow, detections used to update FT of NU1 shown in orange. Direction of motion is represented with the orange arrows.

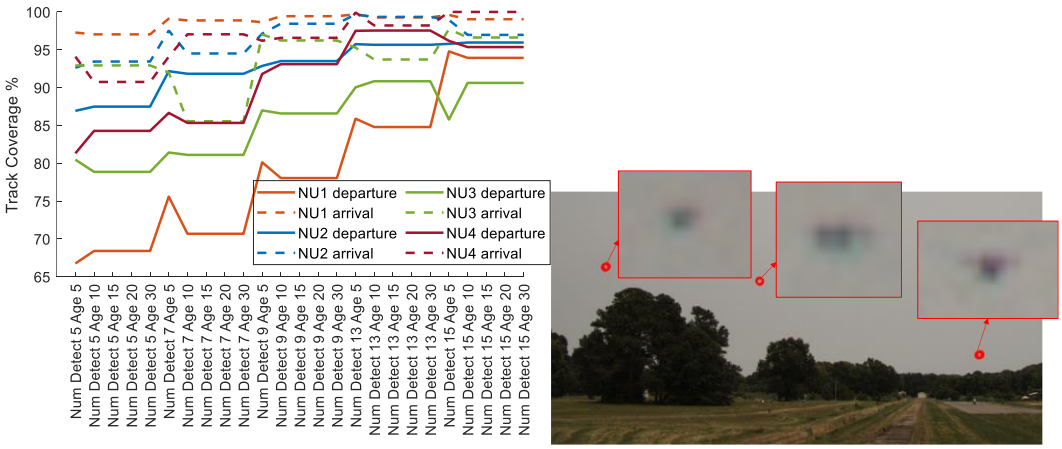

Figure 7.11 Left: Results of track coverage with varying tracker parameters on node 1. Right: Detection results on node 1.

7.4.2 Distributed RADARs fusion results

7.4.2.1 RADAR interference and clutter removal

Figure 7.12 and Figure 7.13 show the raw measurements acquired by the two RADARs in their own RRF coordinates. Although the two RADARs retrieve measurements up to a distance of 6000 meters the plots are constrained from 0 meters to 3000 meters to ease the understanding of the presented data. A difference between the behavior and distribution of measurements from the two RADARs can immediately be noticed. In the rooftop case (Figure 7.12), measurements belonging to the two UAVs can be seen in the time interval going from 200 seconds to almost 600 seconds. Additional targets are also detected by the RADAR, summing up to about 12400 single detections over 13 minutes of acquisition. The distribution of most of detections is spread widely over *r*, *az* and *el*, which traces their generation back to the clutter effect. In the gantry case (Figure 7.13), it is difficult to see any measurement corresponding to the flying UAVs. Here, the occurrence of interference-generated measurements can be observed in terms of bands of range measurements which appear to be concentrated around given time instants and which show a high variation, extending over the whole range span. This large amount of data yielded a total number of about 59600 single detections, which is almost five times greater than the rooftop RADAR's acquisitions. To understand such a difference in the data, the RADARs' geometrical disposition needs to be considered. While the rooftop RADAR was placed at a more distant location with respect to the wythe creek and gantry ones, it was also physically shielded by the presence of obstacles along the line of sight with the other devices (such as the building structure and the tree line). The gantry RADAR was completely exposed to the presence of the wythe creek RADAR and their FOVs overlapped at a shorter distance. The overlap between FOVs is clearly visible in Figure 7.14 where a satellite map of the CERTAIN range reporting the trajectory of the two sUAVs, location and FOVs of RADARs.

The filtering strategies applied to the two RADARs are based on the a priori knowledge of the environment where they operated and their geometrical disposition. In the rooftop case, filtering is only applied based on the measurements of $\dot{r}$, r and RCS by exploiting the thresholds $\dot{r}_{th,low}$=0.9 m/s, $RCS_{th,low}$=-25 dBsm and $RCS_{th,up}$=0

dBsm. An additional filter is then also applied to only retain data corresponding to range measurements below 1200 meters. The application of these filters reduces the clutter and noise as shown in the filtered data for the rooftop RADAR of Figure 7.15, thus reducing the number of single measurements down to 3638. Applying the filtering technique is not as effective in removing the interference-caused range bands for the gantry. Thus, the interference detection and removal strategy is applied using a value of $r_{\sigma th}$=50 meters. This makes it possible to completely remove the presence of the range bands. However, due to the very large vertical FOV set for the gantry RADAR, additional filters are applied on the elevation value, thus removing all detections arising from the ground (i.e., with elevation smaller than -30°). A further analysis to identify the presence of other objects (such as transmitting antennas), potentially generating noise in RADAR measurements, is also performed on such data.

After interference removal and data filtering process the RADAR measurements appear to be much clearer and more suitable to be used during tracking with a total number of measurements substantially reduced to 2586. This reduction is paid in terms of the reduction in useful measurements belonging to the UAVs as well. These can be identified by exploiting the positioning information logged by the UAVs autopilots and computing the difference between the RADAR range measurements and the GNSS-based range (with respect to the RADAR location). Measurements can then be inferred to UAVs if such difference is smaller than a threshold which is set to 4 meters. This method yields a loss of about 44% and 40% of measurements for the first and second UAV, respectively. The measurements retrieved after filtering on the gantry RADAR are shown in Figure 7.16.

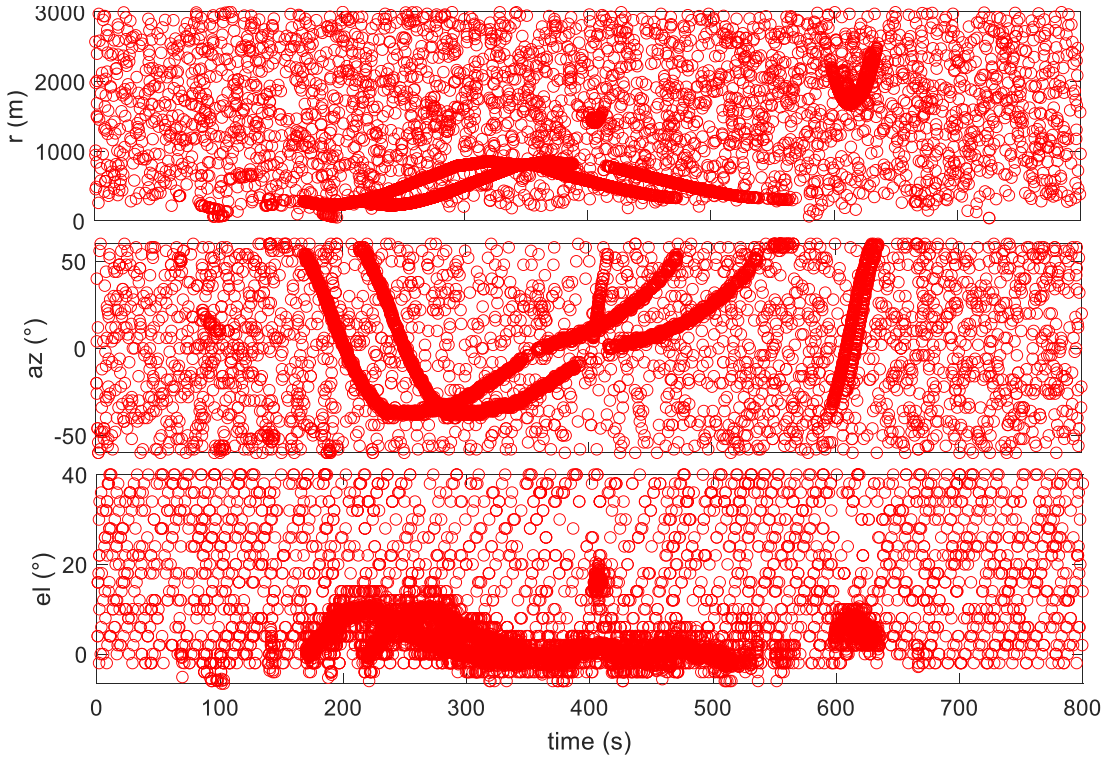

Figure 7.12 Unprocessed RADAR measurements collected by the rooftop RADAR. Only data belonging to a measured range of up to 3000 meters are reported.

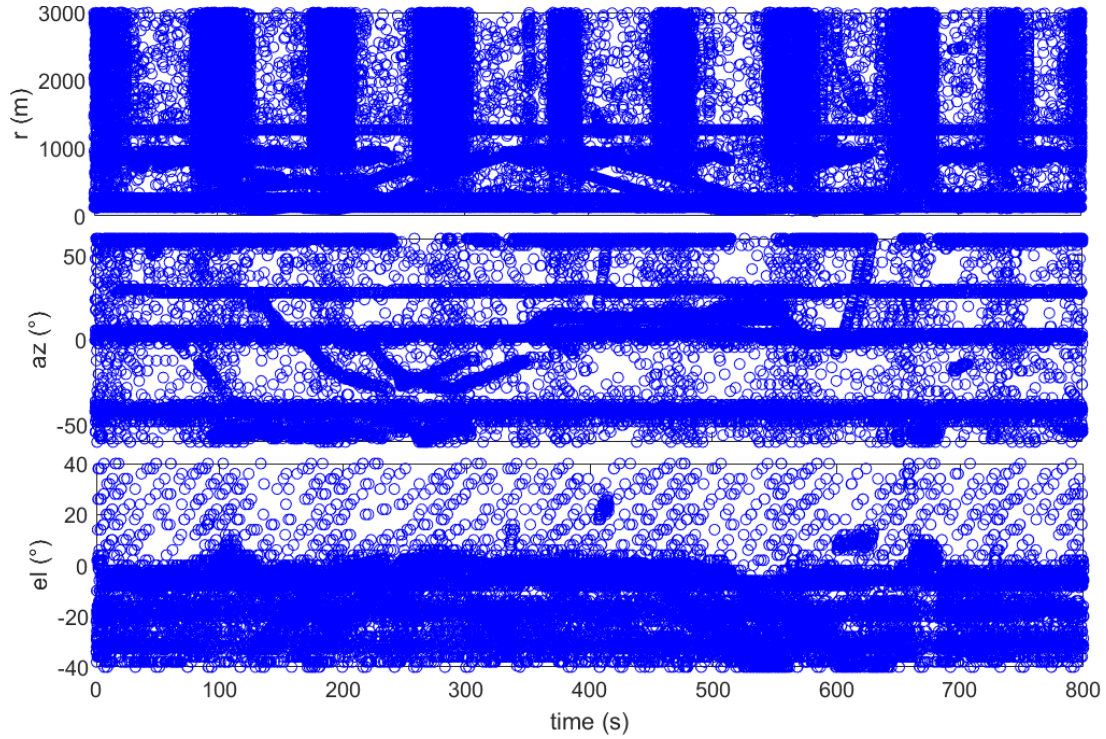

Figure 7.13 Unprocessed RADAR measurements collected by the gantry RADAR. Only data belonging to a measured range of up to 3000 meters are reported.

Figure 7.14 Satellite map of the CERTAIN Range flight area at NASA Langley. Trajectories flown by the UAVs are reported along with the position of the ground nodes operated during the flight. The FOVs of the RADARs are shown as faded triangles starting from the respective location (colored dots).

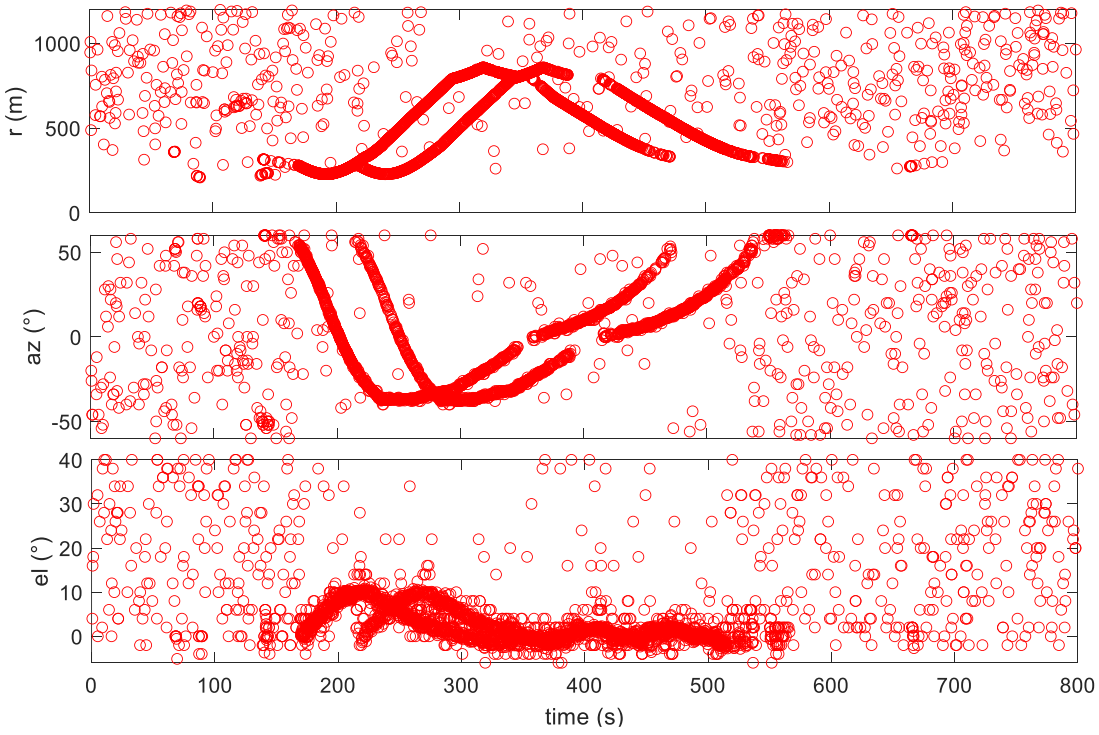

Figure 7.15 Filtered RADAR measurements collected by the rooftop RADAR.

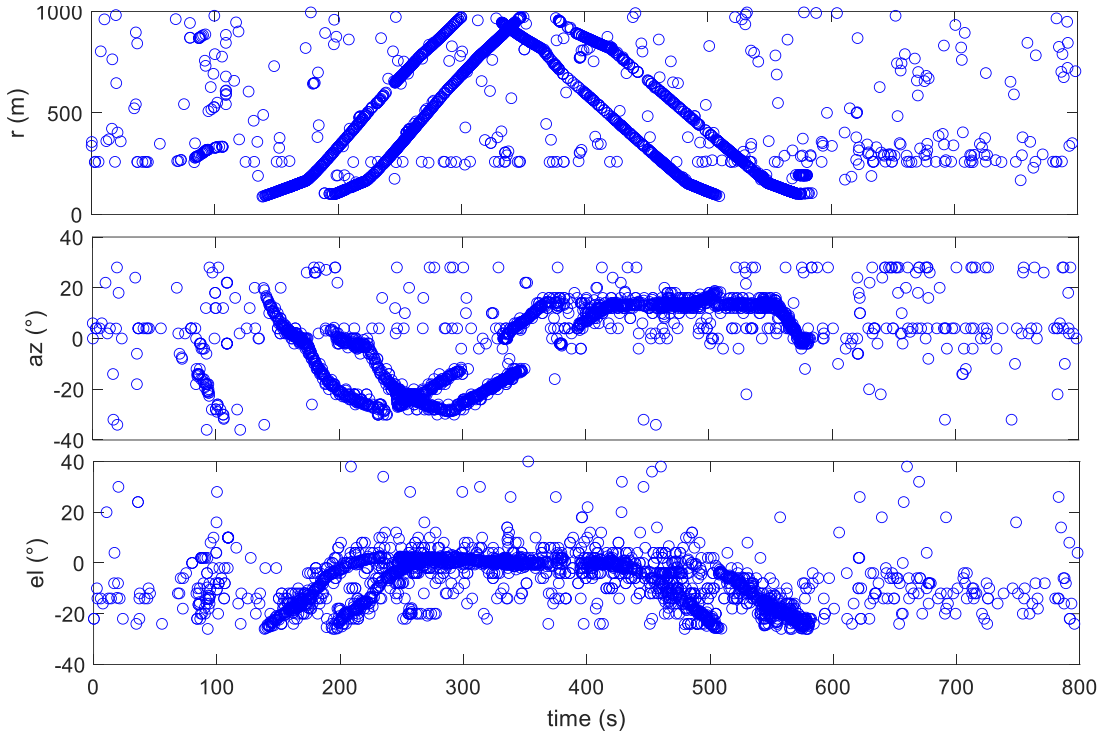

Figure 7.16 Filtered RADAR measurements collected by the gantry RADAR.

7.4.2.2 Leader-Helper Distributed RADAR Fusion Strategy

The proposed EKF makes use of a time step of 0.1 seconds, thus being comparable to the acquisition frequency of RADAR measurements. As a consequence of the complex data filtering process many valid RADAR measurements are lost. This is even more evident in the case of the gantry RADAR, where the interference removal process causes loss of useful information belonging to the UAVs. The fusion of data collected by a network of sensors distributed along the flight field can help reduce track dropouts caused by such losses. In the case of firm tracks, dropouts occur when the prediction steps are performed for more than dt_{FT}=4 seconds. To better highlight advantages in using the distributed fusion strategy, the standalone RADAR tracking solution of the leader RADAR is compared to the fused one, in which the helper RADAR injects its measurements. In both standalone and fused solutions, measurements are first centroided before being passed over to the tracker. During the centroiding, the values of δr=6 meters, δaz=2° and δel=12° are used.

During the tracking process, the two RADARs are used independently until the leader is established. This happens when the first RADAR retrieves a firm track. The second RADAR, thus, acts as helper and it continues its tracking independently

while also sharing useful data with the leader upon need. In the tested case, the first RADAR to retrieve a firm track is the gantry RADAR. Therefore, its standalone EKF-retrieved solution is used as a mean of comparison for the fusion strategy performance. The GNSS positioning information collected and processed by the autopilot of each UAV is taken as ground truth to extract accuracy of the firm tracking estimates. Finally, the difference in track coverage between the fused and standalone results is presented. Specifically, track coverage represents the ratio between the actual presence of the UAV within the FOV of the RADAR and the presence of an estimate of the UAV state from the tracker.

In Figure 7.17 the results of the firm tracking solutions are shown in terms of the estimated *r*, *az* and *el* in the NED reference frame along with the reference ground truth. The first values are reported with the subscript "FT", while the latter are reported with the subscript "GT". The figure shows both the results achieved on the standalone gantry RADAR (left) and the results achieved when such RADAR acts as the leader being aided by the rooftop RADAR (right). The leader RADAR appears to be able to generate tracks of the two UAVs during their flight starting at about 20 seconds from their appearance within the RADAR FOV (when the UAV elevation is larger than -30°). The multi-object nature of the exploited tracker makes it possible to generate and keep separate tracks of multiple objects at the same time. Tracks that cannot be associated to the UAV are reported as "other" in the figure. Some of such tracks show steep azimuth and elevation variations and may be generated by birds flying around the flight area while others, whose temporal length is comparable to dt_{FT}, arise from noise or unremoved clutter measurements. The longest-living tracks generated by the standalone leader tracker correspond to the UAVs, thus demonstrating the adequacy of the data pre-processing step, which is tailored for the preservation of measurements related to the UAV. Still, frequent tracks interruptions (dropouts), caused by measurement losses, occur in these tracks. These dropouts, though not affecting the maximum range at which UAVs are tracked (around 990 meters for both vehicles), cause an intermittent behavior in the UAV tracks, thus promoting the generation of three and five different tracks for N556NU and N561NU, respectively. The use of additional information retrieved by the helper RADAR and shared with the leader can be a powerful tool during dropouts. This can immediately be noticed by looking at the right part of Figure 7.17, where the results

of the fused leader-helper strategy are depicted. In this case, a continuous, unique track of the first UAV (N556NU) is generated with no dropout while, in the case of N561NU, two different tracks are generated, instead. This result promotes the increase of the track coverage which goes from 88.38% to 97.18%, for N556NU, and from 87.42% to 95.84%, for N561NU.

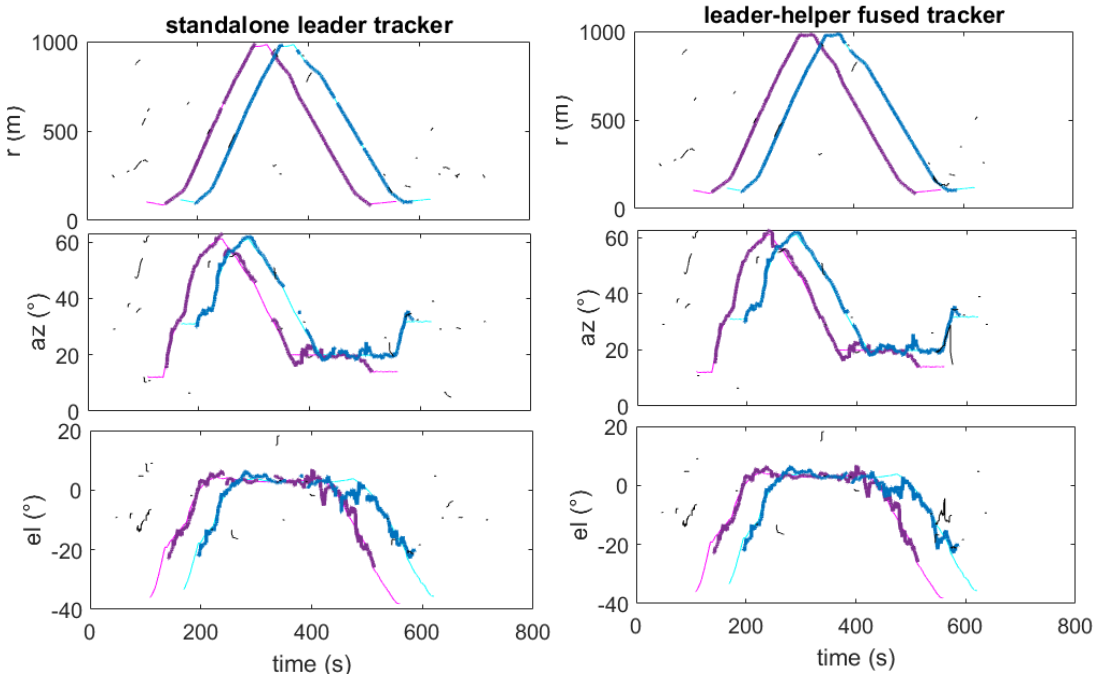

Figure 7.17 Left: Results of standalone leader (gantry) RADAR. Right: Results of fused leader-helper strategy.

A comparison is also performed in terms of tracking accuracy by computing the difference between the estimate from firm tracking and the ground-truth for each UAV. This is shown in terms of range (*r* error), azimuth (*az* error) and elevation (*el* error) root mean square (rms) errors in Table 7.1. In this context, no real benefit in the use of the fused solution (labelled as "L-H") is identified. Indeed, a slight increase in RMS can be noticed in the range case while the angular RMS values appear to be comparable for both cases. This occurrence can be related to the higher value of the range uncertainty contained within the $R_{zh \to l}$ matrix, which is used by the leader to filter its track with the helper's measurement. The range uncertainty increases, due to the translation of measurements between two different locations, at high ranges. The leader tracker completely loses information about the UAV at a range of 900 meters and is able to successfully associate helper's measurements to extend its tracks' life. However, the uncertainty related to such measurement is

higher with respect to the uncertainty of the leader's measurements, thus causing localized increases in the distance between the estimates and the ground truth.

Table 7.1 Performance statistics for standalone leader tracker (L) and fused leader-helper (L-H) tracker.

sUAV	*r* error (m)		*az* error (°)		*el* error (°)	
	L	***L-H***	***L***	***L-H***	***L***	***L-H***
N556NU	1.74	2.31	1.31	1.18	1.86	1.70
N561NU	1.71	2.03	1.18	1.14	2.43	2.40

Chapter 8: Cooperative Magnetic Calibration

Magnetometers play a key role onboard sUAVs both as navigation instruments and environment mapping sensors. With regards to the first point, despite some limitations such as low bandwidth and large measurement noise, magnetometers are typically used in outdoor flight operations to bound the error in heading estimation, unless tactical-grade gyros (accurate enough to sense Earth rotation rate) are exploited. Magnetic measurements enable relatively coarse heading estimates, which depend on intrinsic sensors limitations but above all on disturbances from onboard (e.g., electric rotors and electronic systems) and external sources (e.g., large metal infrastructures). Indeed, such disturbances may significantly alter the direction of the magnetic field and lead to highly inaccurate heading estimates, which may even compromise flight safety if position control is implemented with GNSS information used in feedback.

In this chapter, cooperation between multiple sUAVs is exploited to enable magnetometers' calibration by estimating onboard and external magnetic disturbances. The proposed strategy utilizes highly accurate relative positioning information computed with CDGNSS and visual measurements between two sUAVs: a "chief", whose magnetometers need to be calibrated, and a "deputy", acting as an aiding platform for the scope. The feasibility of such a solution was first analysed in works such as [134], [135] where attitude information independent from magnetic and inertial sources was built based on the use of one or more deputies. The addition of a magnetic calibration strategy also based on this cooperative approach was also introduced in [136], [137] where a single deputy is used and the onboard magnetic disturbances are estimated by formulating the problem as a non-linear system of equations solved using the Levenberg-Marquadt (LM) iterative method [138]. The approach presented in this final chapter of the manuscript builds up on these past research works and adds the following contributions.

- The problem is reformulated to simultaneously compute both the onboard magnetic biases and the external magnetic declination.

- Improvement of heading accuracy is demonstrated by a pointing analysis based on *ad hoc* Ground and Airborne Control Points.

The chapter is structured as follows. Section 8.1 briefly investigates literature examples dealing with usage the of magnetometers for sUAV, thus highlighting the role they play both for navigation and mapping applications. The method with which magnetic disturbances are estimated and magnetometers' calibration is performed is detailed in section 8.2. The experimental results achieved, with a brief description of the dataset used, are presented in section 8.3.

8.1 RELATED WORK

One possible solution for magnetic independent heading estimation is given by dual GNSS antenna architectures [139], though the dependence of heading accuracy on antenna baseline, and the additional weight and complexity, may pose challenges for small flight platforms. If magnetic information needs to be exploited, accurate calibration and estimation of onboard and external biases is the key to enable effective compensation of disturbances. State-of-the-art magnetic calibration methods model the intrinsic error sources with an ellipsoid error model whose parameters are estimated by applying a non-linear optimization process [140], [141]. Such a procedure, which requires in input a set of measurements collected in different pointing conditions of the sensor's axes to properly sample the ellipsoid surface, may encounter challenges when applied during UAV flight operations. Recent references addressing magnetometer calibration, but dealing only with estimation of onboard disturbances, can be found in [142], [143]. Indeed, recent approaches focus on the idea to exploit the variations of the external magnetic field also as a source of positioning information: in [144], a magnetic-based simultaneous localization and mapping (SLAM) approach is studied as an alternative to the usual GNSS-based navigation. Such work is mainly focused on the analysis of a magnetic-based navigation concept which does not rely on prior Earth magnetic anomaly field maps.

UAV-based magnetometry is gaining increasing popularity. For instance, the feasibility and effectiveness of using a small fixed-wing UAV for aeromagnetic missions in remote areas, such as the Bransfield Basin in Antarctica, was shown in

[145]. Specifically, a three-axis fluxgate magnetometer allows generating a magnetic anomaly map. A similar idea is shown in [146], where an 8-rotors copter (DJI S1000+) with a caesium-vapour magnetometer attached with ropes at a 3 meters distance below the UAV (to minimize the effects of onboard disturbances) is used for archaeological purposes or in [147], where both rotorcraft and fixed-wing UAVs are used to map the magnetic anomaly of outcrops in a mining district in Finland, showing results which finely compete with those achievable using ground-based sensors, but within a shorter time interval and with a smaller cost. Recent works propose more compact systems with magnetometers installed in closer proximity with respect to the drone frame [148]. In these cases, the need of accurate magnetic calibration also arises as a prerequisite for effective measurement processing.

8.2 COOPERATIVE MAGNETIC CALIBRATION METHOD

The Earth's magnetic field (**H**) components at the UAV flight altitude can be measured by a three-axes magnetometer along the Body Reference Frame (BRF) directions. From these measures, the magnetic heading angle can be easily estimated by exploiting the sensed horizontal components of the Earth's magnetic field as referred to the Body Stabilized Reference Frame (BSRF), which is obtained as a projection of BRF in the local horizontal North-East plane through a combined pitch (ϑ) and roll (φ) rotation as shown in Eq. (8.1). Here, M_φ and M_ϑ are the rotation matrices already expressed in section 4.2 (with φ and ϑ expressed as α and β, respectively).

$$\mathbf{H}^s = [\, M_\varphi M_\vartheta \,]^{-1} \mathbf{H}^b \tag{8.1}$$

The resulting magnetic heading can be therefore expressed as in Eq. (8.2), where d_m is the local magnetic declination, i.e., the angle between the local magnetic (N_m) and geographical (N) North directions.

$$\psi_m = tg^{-1}\left(-\frac{H_y^s}{H_x^s}\right) + d_m \tag{8.2}$$

However, the onboard electric devices, such as the electric rotors, introduce a disturbance on the quantity sensed by the magnetometers. This disturbance can be modelled as a bias, $\mathbf{\Delta H}$, constant in BRF, which induces an error in the estimation of

the Earth's magnetic field direction. Under the assumption of small roll and pitch rotations, **ΔH** can be assumed to be constant in BSRF, and the effect of the vertical component of **ΔH** in BRF (ΔH_z^b) on heading estimation can be considered negligible. This assumption is considered in this work since the main interest lies in improving heading and magnetic declination accuracy, without aiming at full 3d calibration.

A graphic illustration of the problem under analysis can be found in Figure 8.1, which clearly shows how the magnetic field vector estimated by magnetometers and projected in BSRF ($\mathbf{H}^s$) can be expressed as the sum of the true Earth magnetic field vector in BSRF ($\mathbf{H}_e^s$) which is aligned with the N_m direction, and the internal magnetic biases vector in the same reference frame ($\mathbf{\Delta H}^s$). The effect of such biases can be equivalently seen as an apparent shift of the magnetic and geographic North directions respectively to $N_{m,a}$ and N_a, as shown in Figure 8.1, thus resulting in the heading angle expressed in Eq. (8.2), which will be referred to as "non-calibrated" ($\psi_{m,nc}$), to be ill-defined. A more accurate angle, referred to as "calibrated" ($\psi_{m,c}$), can then be computed if the in-plane components of $\mathbf{\Delta H}^s$ are estimated and removed from its formulation, as expressed in Eq. (8.3).

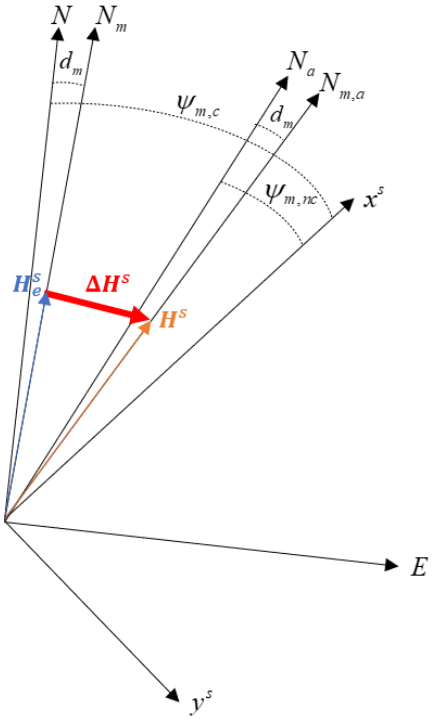

Figure 8.1 Graphic illustration of the effect of magnetic bias on the magnetic heading angle estimation.

$$\psi_{m,c} = tg^{-1}\left(\frac{-H_y^{\,s} + \Delta H_y^{\,s}}{H_x^{\,s} - \Delta H_x^{\,s}}\right) + d_m \tag{8.3}$$

The calibration strategy described in this work takes its roots from the previous work illustrated in [137] and computes bias components ΔH_x^s and ΔH_y^s by using the same iterative least-squares minimization (LM) procedure. However, the magnetic declination at the flight location is added to the unknowns of the problem. Hence, the proposed approach can be used to correct both "onboard" bias and external disturbances by means of multi-UAV cooperation. The iterative procedure is based on the minimization of the residual obtained as the difference between the unit vector representing the chief–deputy Line Of Sight (LOS) in NED as reported by CDGNSS data and projected in CRF ($\mathbf{u}^{\mathrm{c}}|_{\mathrm{cdgnss}}$), and the same quantity as estimated by visual-based techniques ($\mathbf{u}^{\mathrm{c}}|_{\mathrm{vision}}$). This can be mathematically put as in Eq. (8.4).

$$\mathbf{r} = \mathbf{u}^{\mathrm{c}}|_{\mathrm{vision}} - \mathbf{u}^{\mathrm{c}}|_{\mathrm{cdgnss}} = 0 \tag{8.4}$$

The LOS in CRF is obtained from the pixel coordinates by knowing the intrinsic camera parameters estimated by offline camera calibration. On the other hand, the CDGNSS-based estimate of the LOS in CRF can be obtained by rotating the unit vector corresponding to the CDGNSS relative position vector ($\mathbf{u}^{\mathrm{n}}|_{\mathrm{cdgnss}}$) from NED to BRF, and then from BRF to CRF.

These rotations are achieved by multiplying the vector with the matrices M_n^b and M_b^c. The misalignment angles between BRF and CRF (determining M_b^c), also referred to as extrinsic camera-IMU rotational parameters, can be computed by the camera offline calibration procedure [149]. More in general, the lever arm of the GNSS antenna with respect to the camera installation on the chief could be considered. However, if the offset is small, the resulting effect is negligible. The final cost vectorial function $\mathbf{r}$ can now be expressed in terms of the unknowns as written in Eq. (8.5).

$$\mathbf{r} = f(\Delta H_x^{\,s}, \Delta H_y^{\,s} d_m) = \mathbf{u}^c\big|_{vision} - M_b^c M_n^b\, \mathbf{u}^n\big|_{cdgnss} \tag{8.5}$$

This calibration technique fully relies on the availability of GNSS data for both platforms and on the deputy visibility with respect to the chief, thus implying that the

two vehicles must fly under nominal GNSS coverage conditions and that the deputy must fall in the FOV of the chief camera. For this reason, as a general condition, chief and deputy should be kept facing each other during the flight, if equipped with strapdown frontal-looking cameras. Moreover, the accuracy of the calibration technique is affected by the inter-UAV distance. As a rule of thumb, accurate calibration requires a minimum distance of a few tens of meters.

An additional condition for the proposed calibration procedure, is the need to ensure synchronization of GNSS data (from both the chief and deputy) and camera images, thus building a correspondence between the two vectors used in Eq. (8.5). In this respect, accurate synchronization is performed by time-tagging both chief and deputy data with GNSS time (as previously discussed in section 4.2 of this manuscript). Clearly, to ensure observability of the problem's unknowns, Eq. (8.5) must be written considering a set of *k* camera frames. This results in a 3*k*x1 residual vector **r** which can be minimized by applying the LM algorithm. The proposed approach is summarized by the scheme in Figure 8.2.

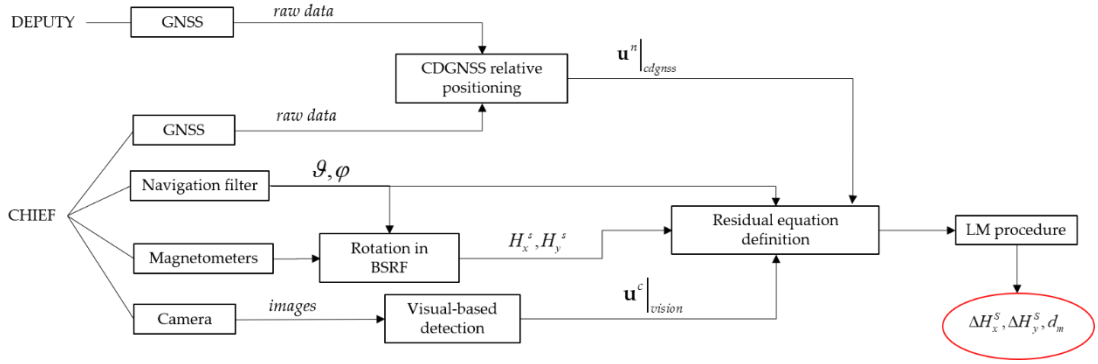

Figure 8.2 Flow diagram of the proposed magnetic calibration strategy.

Rather than computing the vectorial cost function as Eq. (8.5) states, an equivalent scalar chi-squared function (χ^2) is computed, and its minimization is carried-out. This function is expressed in Eq. (8.6) where the W matrix is the 3*k* x 3*k* block diagonal weight matrix associated to each residual. Such matrix is also shown in Eq. (8.6) where W_1,..,W_k are the 3 x 3 weight diagonal matrices associated to each of the *k* frames and defined, for the *i*-th frame, as $W_i = diag\left(\frac{1}{Diag\left(R^c_{cdgnss} + R_{vision}\right)}\right)$.

Here, R^c_{cdgnss} and R_{vision} are the covariance matrix associated to CDGNSS and vision measurements expressed in the same frame of the residual, i.e. CRF.

$$\chi^2(\Delta H_x^s, \Delta H_y^s, d_m) = \mathbf{r}^T W \mathbf{r}$$

$$W = \begin{bmatrix} W_1 & 0 & & \cdots & 0 \\ 0 & W_2 & 0 & \cdots & 0 \\ \vdots & \ddots & \ddots & \ddots & \vdots \\ 0 & & \cdots & 0 & W_k \end{bmatrix} \tag{8.6}$$

At each new iteration, a correction of the unknown quantities, i.e., $\mathbf{h}_{LM}$, is added to their value as computed at the previous step. This quantity is expressed in Eq. (8.7), where J is the Jacobian matrix representing the derivatives of the cost function **r** with respect to the three problem unknowns, also called parameters, of the LM procedure and identified by the vector $\mathbf{p} = [\Delta H_x^s, \Delta H_y^s, d_m]$, λ is the LM damping parameter representing how close the procedure is getting to the gradient descent or the Gauss-Newton methods, form which the LM is built, and $D(J^TWJ)$ is the matrix which does only contain the diagonal of the J^TWJ matrix.

$$\mathbf{h}_{LM} = (J^T W J + \lambda D(J^T W J))^{-1} J^T W \mathbf{r} \tag{8.7}$$

The iterative procedure is either stopped when one of the convergence criteria for the LM procedure, as listed in Eq. (8.8), is met or when the maximum number of iterations is reached.

$$\begin{aligned} &\max\left(\left|J^T W \mathbf{r}\right|\right) < \varepsilon_1 \\ &\max\left(\left|\frac{\mathbf{h}_{LM}}{\mathbf{p}}\right|\right) < \varepsilon_2 \\ &\frac{\chi^2}{k-1} < \varepsilon_3 \end{aligned} \tag{8.8}$$

8.3 EXPERIMENTAL RESULTS

8.3.1 Experimental Setup

Data used to test the proposed calibration strategies were collected during the flight of two customized DJI M100 sUAVs. The first, “Eagle” (already described in section 4.1 of this manuscript) is here used as the chief while the second, “Athena” (introduced in section 3.5 of this manuscript) is used as the deputy. As already mentioned, both platforms are equipped with visual cameras, mounted in a forward direction, and GNSS receivers and antennas. In addition, a ground-based GNSS antenna and receiver (Trimble AV59 and BD960) is used as a Ground Control Point

(GCP) for assessing the performance of the proposed methodology by means of a pointing accuracy which will be discussed in the following section.

The experimental campaign, which took place in Acerra (NA), Italy in December 2019, consisted in two flights. At this location and date the magnetic declination predicted by the International Geomagnetic Reference Field is 3.39° [150]. Due to the relative geometry of the two UAVs, including relative turns and large heading variations, the second flight is chosen to carry out magnetometer bias estimation.

During this flight, which lasted around 11 minutes, chief GNSS, magnetometers and IMU data were respectively collected at 1 Hz, 10 Hz and about 137 Hz.

The flight was characterized by manoeuvres to keep the two UAVs facing each other. Thus, the chief was rotated around the deputy as it is visible in Figure 8.3, where Easting and Northing of both UAVs as computed with their GNSS data (also indicating the starting and ending points of their trajectory) are shown. The above-ground altitude of both UAVs does not vary significantly during flight; mean values, as evaluated by GNSS, are about 16.0 meters for Athena and 16.8 meters for Eagle. A chief-taken image showing both Athena and the ground-based GNSS (Trimble) antenna is shown in Figure 8.4 where both targets can be easily detected by eye.

The magnetometers output during the flight is shown in Figure 8.5, where both x and y coordinates of the sensed Earth magnetic field in BSRF are depicted, such quantities are provided by the chief autopilot through the DJI Onboard SDK interface, in (non-better specified) “normalized” magnetic unit (based on DJI documentation, magnetic measurements are normalized so that the norm is included in the range be-tween 1000 and 2000). As a reference, the norm of the Earth magnetic field vector at flight location and date is equal to 46432 nT, as estimated from [150]. An analysis on a static portion of the data acquisition, i.e., including the first 60 seconds, shows a scale factor of about 29, which is used in the following to convert DJI normalized units to nT. This scale factor has been obtained by dividing the norm of the predicted magnetic field in nT by the norm of the measured magnetic field (in DJI normalized units) in static configuration.

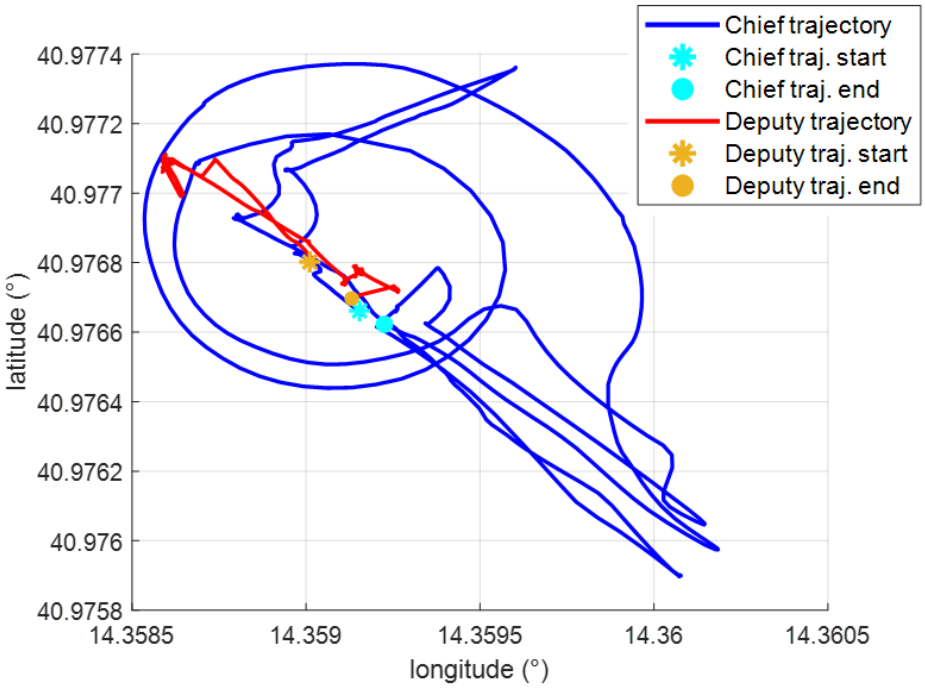

Figure 8.3 Trajectory of chief and deputy during experimental tests as computed with GNSS data.

Figure 8.4 Example of chief-taken frame where both deputy (Athena) and GCP (Trimble antenna) are visible.

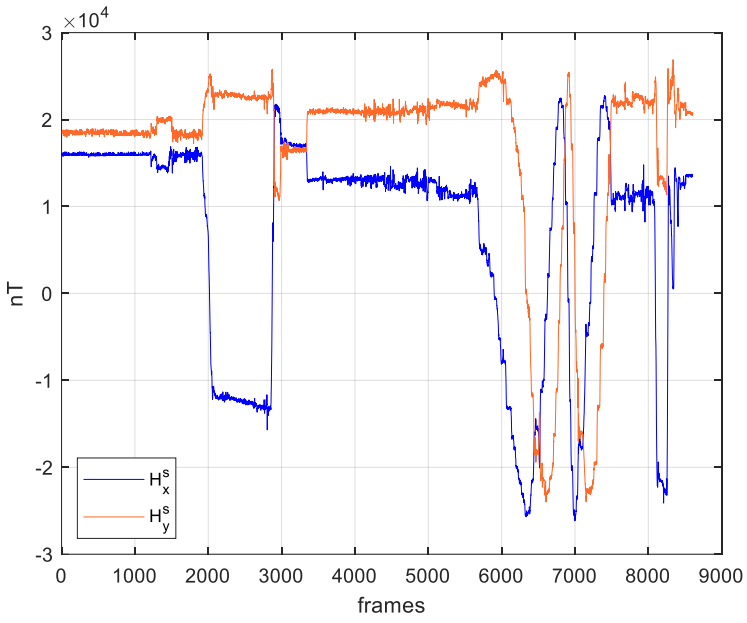

Figure 8.5 Horizontal BSRF components of the magnetometer measurements in nT as provided by the DJI Onboard SDK interface.

8.3.2 Experimental Results

The iteration process which leads to the estimation of both internal magnetic biases and external magnetic field declination starts by selecting a set of camera frames which will be used as input. To do so, constraints are imposed on chief-to-deputy distance, which is kept larger than 30 m to improve the accuracy of the CDGNSS-based LOS unit vector in NED, and on the absolute value of chief yaw rate and pitch and roll angles (as estimated by its onboard navigation system). In order to avoid too fast heading variations which may pose challenges due to the low magnetometer bandwidth and the residual data synchronization errors, the yaw rate is requested to be smaller than 1.5 °/s, while, in order for the small angles assumption to hold, maximum pitch and roll angles of 6.5° are considered. Once selected, frames are organized to cover three different flight portions identified as “Whole Flight”, in which all frames compliant with the aforementioned requirement are used for calibration, and “subset 1”, “subset 2” in which selected frames are extracted from smaller intervals. Each flight portion case is obtained from the previous ones by reducing the selected frames interval. The whole flight case involves the higher number of frames (43) which are reduced to 31 and 27 in the subsets 1 and 2 respectively. The latter are intended to represent different flight portions with variations in the heading of the chief during its rotation around the deputy. In subset

1 such variation goes from -69.8° to 59.4° while in subset 2 it is slightly wider, reaching a final heading of 124.7°. Furthermore, relatively short baselines (absolute value of $\mathbf{u}^c|_{cdgnss}$) on average of about 65 m are used. Results achieved in terms of estimated magnetic biases are reported in Table 8.1. The values set for LM iterations are 10^{-8}, 10^{-4} and 10^{-16} respectively for ε_1, ε_2 and ε_3 for the parameters of Eq. (8.8), while initial guess are set to zero, for the internal magnetic bias components in BSRF, and to the true value of magnetic declination (3.39°) for the d_m angle. An initial value of the damping parameter (λ_0) had also to be provided and is set to 10^{-4}.

The results show that estimated biases have small variation with respect to the number of frames exploited for their computation, thus demonstrating that the procedure can be performed by avoiding the exploitation of frames from the whole flight and, instead, utilize a reduced number of frames which belong to a specific flight portion (and dynamic).

Table 8.1 Estimated magnetic biases from LM iterations.

Case	ΔH_x^s	ΔH_y^s	d_m (°)
Whole Flight	-45.84	43.18	7.58
Subset 1	-44.04	41.89	7.69
Subset 2	-38.40	50.89	8.25

To evaluate the quality of the results, a pointing error analysis is performed following the same approach of [151] and using an *ad hoc* selected control point (CP). The unit vector between the chief UAV and the CP is computed in NED using CDGNSS processing, and the azimuth angle is extracted to be used as (attitude independent) reference measurement (az_{ref}). The azimuth angle is then evaluated using images and the estimated chief attitude angles. In particular, the pixels coordinates corresponding to the control point location in chief-taken images are first used to compute the chief-to-CP unit vector in CRF. This unit vector is then transformed in NED by using M_b^c and the NED-BRF rotation matrix evaluated by using three different heading angles: the calibrated and non-calibrated magnetic ones, which lead respectively to $az_{m,C}$ and $az_{m,NC}$, and the heading angle as estimated by the onboard DJI filter, leading to az_{DJI}. The pointing error is the difference between these angles and the reference one, i.e. az_{ref}, and it can thus be computed and used for performance assessment. The uncertainty of the pointing error estimate is evaluated

by summing up the CDGNSS covariance, expressed in angular quantities, and the camera angular uncertainty. These quantities are representative of the error on az_{ref} and camera estimated quantities (i.e. $az_{m,C}$, $az_{m,NC}$ and az_{DJI}), respectively.

Results of such analysis are shown on the left in Figure 8.6 for the whole flight case when the Trimble ground-based antenna is used as ground control point (GCP). In the top rows of the figure the pointing errors computed with $az_{m,C}$, $az_{m,NC}$ and az_{DJI} are respectively shown in orange, yellow and blue. While the bottom rows show the heading angle ψ as computed by the DJI filter. It has to be mentioned that pointing errors can only be computed with respect to frames where the Trimble antenna can be easily detected. This occurs in two main frame intervals, as Figure 8.6 left shows.

The calibrated pointing error performance appears to be significantly improved with respect to both non-calibrated and DJI-based heading estimates, thus clearly proving the effectiveness of the proposed calibration methodology. This can be inferred by considering the statistics of each pointing error, mainly in terms of mean and root mean squared error (rms). As a matter of fact, the calibrated mean value, equal to -0.14°, also shown in the figure as a dashed black line, is remarkably smaller than the non-calibrated and DJI-based ones, which are, instead, respectively equal to -8.5° and -2.3°. This trend is confirmed by the calibrated RMS, equal to 0.95°, which is again smaller than the non-calibrated one, equal to 8.6°, and DJI-based one, equal to 3.3°. Furthermore, the mean value of the pointing error for the calibrated heading appears to be well contained within the 3σ bound region for the benchmark, highlighted in grey in Figure 8.6. It is worth noting that pointing errors of the DJI onboard filter change in the initial and final phases of the flight though the heading angle is similar, as a result of the filter dependency on the experimented dynamics. It is also worth mentioning that performing calibration with the originally proposed method [134], i.e. ignoring the estimation of external bias, results in a pointing accuracy mean error equal to -2.7°. in the whole flight case.

To further assess the quality of the calibration procedure, the pointing analysis is also performed considering the other flight experiment carried out during the same day (flight 1) and using the deputy (Athena) as airborne control point (CP). As before, $az_{m,C}$ and $az_{m,NC}$ are estimated by using calibrated and un-calibrated heading angles (Eq. (8.3) and Eq. (8.2), respectively) with magnetometer biases set as those

reported in Table 6, for the whole flight case. Pointing analysis results are shown on the right in Figure 8.6. The difference between $az_{m,C}$ and az_{ref}, which is depicted in orange, has a mean that is well within the 3σ bound,. In addition, analyzing the link between the pointing results and the heading variation, it is possible to verify that pointing accuracy is independent from heading for the calibrated solution. Indeed, azimuth error results to be heading dependent, for other cases ($az_{m,NC}$ and az_{DJI}) thus demonstrating a worse compensation of onboard magnetic biases.

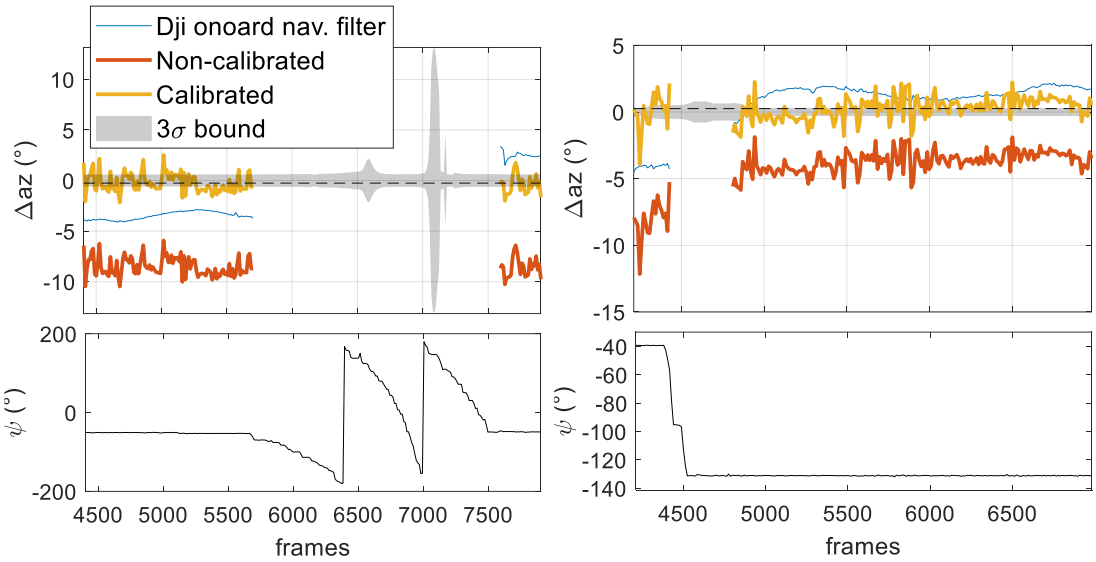

Figure 8.6 Left: Pointing analysis results of the whole flight case using Trimble as GCP. Right: Pointing analysis results on Flight 1 using deputy as CP.

Chapter 9: Conclusion

This thesis contributes to the international research efforts aimed at increasing autonomy of low-altitude sUAVs. Indeed, it focuses on sensing and data fusion strategies for Detect And Avoid and surveillance applications, on the one side, as well as for magnetic sensors' calibration exploiting multi-UAV cooperation, on the other side. Such capabilities are relevant to the novel applications which have arose in the latest years, foreseeing increasingly autonomous operations also performed in and around urban areas. From the Detect and Avoid perspective, non-cooperative (RADAR- and visual-based) strategies are investigated to tackle the issue of absent or unreliable GNSS-based positioning information while strengthening the solution towards all types of intruders, either transponder-equipped or not. Instead, from the navigation perspective, cooperation between multiple platforms is used to improve the performance of a single UAV.

First analyses are focused on the investigation of the conflict detection performance for multi-sensor and visual-only architectures. In the first case, the sensing approaches are tailored to near-collision geometries and possible closure rates of intruders in the different regions of the field of regard of the own-ship. This generates an adaptive strategy which effectively supports the design of an own-ship-borne sensing architecture. The concept is corroborated by numerical analyses showing that similar conflict detection performance is achieved when different sensors are used to cover specific regions of the field of regard; either using a RADAR/camera architecture, with the RADAR in the central region, or a two-cameras with different performance architecture. In the case of visual-only sensing strategies, the attention is shifted to the lack of ranging information. An adaptive, multi-mode conflict detection solution is exploited which utilizes range estimates achieved with a shape-based method, assuming the identifiability of the intruder's class. Experimental tests with two sUAVs show the reliability of the shape-based ranging information up to 150 meters in distance and higher consistency with actual collision conditions when exploited for conflict detection.

Performance assessment of RADAR-based and visual-based sensing for sUAVs is performed by exploiting data collected during ground-to-air experimental campaigns with a low SWaP FMCW scanning array RADAR and a sUAV performing encounters with the sensing setup. Kalman filters, either linear (for the camera) or extended (for the RADAR), are designed to perform multi-target tracking based on the measurements retrieved. In the visual case, different detectors, based on deep-learning approaches or morphological filtering and adaptive template matching, are tested and applied on the image region above the horizon line (given the geometry of the tests). The expected sub-degree angular accuracy is retrieved on the firm tracking estimates in both cases. In the RADAR case, filtering procedures are needed to pre-process RADAR data and remove clutter based on the available doppler measurements while an innovative centroiding strategy is also introduced to merge clusters of detection plausibly arising from the same target. At tracking level, due to the wide dimensions of the RADAR beam (especially in the vertical direction), the angular accuracy reaches degree-level root mean square errors, thus being not comparable to the visual one. However, benefits are found in terms of the meter-level and meter-per-second level accuracy in distance and velocity estimates.

Tests on the standalone sensing implementation highlight the advantages of a RADAR/visual fused solution which can leverage on the complementarity of the measurements while strengthening the architecture towards external factors such as weather and illumination, for the camera, and clutter presence, for the RADAR. Different fusion strategies exploiting variations in both structural and algorithmic levels, are thus proposed and their validation is also carried out on experimental data. Two centralized schemes with increasing computational complexity are proposed. In the first, the RADAR acts as the main sensor for firm track generation and the camera measurements are combined, within a unique EKF, to improve its angular and angular rates estimates. In the second, an additional fusion step, i.e., “Fuse-Before-Track”, is designed to filter RADAR data based on consistency checks with the camera before tracking, where both measurements are also combined. The comparable performance of both solutions shows their suitability for the desired improvements of RADAR accuracy in angular terms and the preservation of distance (and velocity) information with meter-level (and meter-per-second) errors. The beneficial effects of data fusion on conflict detection are also highlighted with

improvements in the accuracy of distance at closest point of approach with respect to a standalone RADAR solution. A further fusion strategy reducing the computational load is presented exploiting a de-centralized Track-to-Track fusion solution. In the latter, each sensor independently generates firm tracks which are then fused, accounting for heterogeneous state vectors, within a fusion center. This solution also proves the expected performance with slightly decreased declaration ranges, arising from the limitation of performing fusion only when both sensors have reached the firm tracking stage.

The design of surveillance strategies for AAM and UAM scenarios, exploiting a network of distributed ground-based sensing nodes, equipped with RADARs and cameras, is then investigated. In this framework, tests are performed with data collected during joint experimental activities with the NASA Langley Research Center, in which a realistic air traffic scenario was reproduced with up to five sUAVs flying simultaneously on the same route. In such scenario, first analyses show that the use of RADAR-only solutions leads to lower track coverage with respect to visual-only solutions. This is imputable to the number of valid measurements used for tracking, which is lower for the RADAR due to the highly cluttered operative environment. This is aggravated by the effects of interference, experimentally observed during the operations of multiple RADARs with overlapping FOVs. This effect can be mitigated, yielding to the possibility of using RADAR data for tracking, by adopting data-based filtering strategies which detect interference-affected measurements based on their distribution in range, azimuth and elevation. The compensation of interference and clutter effects, which lead to low track coverages, is proved to be feasible when fusion of data between the RADARs of the network is exploited. In this case, exploiting a two-RADARs "leader-helper" strategy, where measurements from a helper RADAR are used by the leader to increase the lifespan of its firm tracks, provides a 10% increase in coverage with respect to the one-RADAR-only solution.

Finally, a multi-UAV cooperation strategy is proposed to improve navigation performance of sUAVs by enabling calibration of magnetometers onboard a "chief" platform exploiting a "deputy" one. The method is based on the use of CDGNSS relative positioning information coupled with visual information for the computation

of both internal magnetic biases and external disturbance, promoting improvements in the heading angle estimation. A pointing analysis based on ground and airborne control points demonstrates that calibrated magnetic heading provides sub-degree mean errors for different heading angles, proving a clear improvement with respect to uncalibrated estimates and also to the estimates provided by the onboard navigation filter.

Future works for both DAA and UAM/AAM surveillance contexts share common aspects with current efforts being made towards the adaptation of the proposed fusion strategies to real-time applications. This aspect demands extensive experimental tests and investigation of the needed requirements for data exchange and budget constraints. Nevertheless, to enable a complete performance assessment of the strength and robustness of such strategies, the tests shall also account for non-nominal conditions in terms of illumination, scene background and environment, thus properly challenging the sensing architecture. The inclusion of airborne data in the fusion approach, enabling a proper assessment of conflict detection in air-to-air low altitude scenarios, is also a point which will be addressed in the near future. In these regards, scenarios with various conflict geometries between sUAVs will be reproduced yielding to the possibility of evaluating the impact of avoidance maneuvers on the sensing segment. As far as the distributed sensing work is concerned, future works will be focused on further improvements of the proposed fusion strategy by tackling several points. First, the hierarchical logic with which a leader RADAR is elected in the purely RADAR-based sensing strategy will be compared to a solution in which all measurements from all active RADARs are used when available. This latter approach will be studied aiming to promote an improvement in the accuracy of the tracking estimate which will benefit from the spatial diversity of the retrieved measurements. A final surveillance architecture exploiting all the information retrieved by the ground-based nodes will then be designed by incorporating visual data as well. In this latter context, major attention will be given to the evaluation of visual-based detection strategies encompassing both above and below the horizon targets. Finally, future developments will also focus on the characterization of the RADAR interference phenomenon, thus paving the way for the design of a robust and reliable surveillance strategy for a network of distributed active sensors.

As far as the magnetic calibration strategy is concerned, further research is foreseen in different directions. First, the cooperative method will be extended towards full 3D magnetic calibration. This requires proper attitude variations (in roll and pitch) to enhance the observability of vertical biases. Consistently with these developments, the potential of the technique towards UAV-based magnetometry will be explored, also taking advantage from high sensitivity magnetometers embarked as mission payloads.

List of publications

- Articles published in scientific journals:
  - F. Vitiello, F. Causa, R. Opromolla, and G. Fasano, "Onboard and external magnetic bias estimation for uas through cdgnss/visual cooperative navigation," Sensors, vol. 21, no. 11, 2021, doi: https://doi.org/10.3390/s21113582.
  - F. Vitiello, F. Causa, R. Opromolla, and G. Fasano, "RADAR/Visual Fusion With Fuse-Before-Track Strategy For Low Altitude Non-Cooperative Sense And Avoid," Aerospace Science and Technology, vol. 146, 2023, doi: https://doi.org/10.1016/j.ast.2024.108946.

- Articles published in conference proceedings:
  - F. Vitiello, F. Causa, R. Opromolla, and G. Fasano, "Improved Sensing Strategies for Low Altitude Non Cooperative Sense and Avoid," in 2021 IEEE/AIAA 40th Digital Avionics Systems Conference (DASC), San Antonio, TX, USA, Oct. 2021. doi: https://doi.org/10.1109/DASC52595.2021.9594495.
  - F. Vitiello, F. Causa, R. Opromolla, and G. Fasano, "Detection and tracking of non-cooperative flying obstacles using low SWaP RADAR and optical sensors: an experimental analysis," in 2022 International Conference on Unmanned Aircraft Systems, ICUAS 2022, Dubrovnik, Croatia, Jun. 2022. doi: https://doi.org/10.1109/ICUAS54217.2022.9836085.
  - F. Vitiello, F. Causa, R. Opromolla, and G. Fasano, "Ground-to-air experimental assessment of low SWaP RADAR-optical fusion strategies for low altitude Sense and Avoid," in 2022 41st AIAA/IEEE Digital Avionics Systems Conference (DASC), Portsmouth, VA, USA, Sep. 2022. doi: https://doi.org/10.1109/DASC55683.2022.9925826.
  - F. Vitiello, F. Causa, R. Opromolla, and G. Fasano, "Experimental analysis of RADAR/Optical track-to-track fusion for non-cooperative Sense and Avoid," in 2023 International Conference on Unmanned Aircraft Systems, ICUAS 2023, Warsaw, Poland, Jun. 2023. doi: https://doi.org/10.1109/ICUAS57906.2023.10156570.
  - F. Vitiello et al., "Assessing Performance of RADAR and Visual Sensing Techniques for Ground-To-Air Surveillance in Advanced Air Mobility," in AIAA/IEEE 42nd Digital Avionics Systems Conference - Proceedings, Barcelona, Spain, Sep. 2023. doi: https://doi.org/10.1109/DASC58513.2023.10311270.
  - C. V Dolph et al., "Distributed Sensor Fusion of Ground and Air Nodes using Vision and RADAR Modalities for Tracking Multirotor Small Uncrewed Air Systems and Birds," in AIAA SCITECH 2024 Forum, Orlando, FL, USA, Jan. 2024. doi: https://doi.org/10.2514/6.2024-1781.
  - F. Vitiello et al., "Experimental testing of data fusion in a distributed ground-based sensing network for Advanced Air Mobility," in AIAA SCITECH 2024 Forum, Orlando, FL, USA, Jan. 2024. doi: https://doi.org/10.2514/6.2024-2008.

Bibliography

[1] M. Erdelj, E. Natalizio, and I. F. Akyildiz, "Help from the Sky: Leveraging UAVs for Disaster Management," *IEEE Pervasive Computing*, vol. 16, no. 1, pp. 24–32, 2017, doi: 10.1109/MPRV.2017.11.

[2] C. Deng, S. Wang, Z. Huang, Z. Tan, and J. Liu, "Unmanned aerial vehicles for power line inspection: A cooperative way in platforms and communications," *Journal of Communications*, vol. 9, no. 9, pp. 687–692, Sep. 2014, doi: 10.12720/jcm.9.9.687-692.

[3] J. Primicerio *et al.*, "A flexible unmanned aerial vehicle for precision agriculture," *Precis Agric*, vol. 13, no. 4, pp. 517–523, Aug. 2012, doi: 10.1007/s11119-012-9257-6.

[4] "Amazon Prime Air prepares for drone deliveries Sta." Accessed: Jan. 28, 2024. [Online]. Available: https://www.aboutamazon.com/news/transportation/amazon-prime-air-prepares-for-drone-deliveries

[5] SESAR JU, "European Drones Outlook Study Unlocking the value for Europe," 2016.

[6] John A. Volpe National Transportation Systems Center (U.S.), "Unmanned Aircraft System (UAS) service demand 2015 - 2035 : literature review & projections of future usage," 2014. Accessed: Jan. 04, 2024. [Online]. Available: https://rosap.ntl.bts.gov/view/dot/12029

[7] A. Zeitlin, "Performance Tradeoffs and the Development of Standards," in *Sense and Avoid in UAS: Research and Applications*, John Wiley and Sons, 2012, pp. 35–54. doi: 10.1002/9781119964049.ch2.

[8] M. Orefice, V. Di Vito, and G. Torrano, "Sense and Avoid: Systems and Methods," in *Encyclopedia of Aerospace Engineering*, vol. 9, John Wiley & Sons, Ltd, 2015. doi: 10.1002/9780470686652.eae1149.

[9] D. M. Marshall *et al.*, "Regulatory and Technology Survey of Sense-and-Avoid for UAS," 2007.

[10] G. Fasano, D. Accado, A. Moccia, and D. Moroney, "Sense and avoid for unmanned aircraft systems," *IEEE Aerospace and Electronic Systems Magazine*, vol. 31, no. 11, pp. 82–110, Nov. 2016, doi: 10.1109/MAES.2016.160116.

[11] M. Consiglio, J. Chamberlain, C. Muñoz, and K. Hoffler, "Concept of integration for UAS operations in the NAS," in *28 TH INTERNATIONAL CONGRESS OF THE AERONAUTICAL SCIENCES (ICAS)*, Brisbane, Australia, Sep. 2012. Accessed: Jan. 18, 2024. [Online]. Available: https://ntrs.nasa.gov/citations/20120015770

[12] S. M. Lee, C. Park, M. A. Johnson, and E. R. Mueller, "Investigating Effects of Well Clear Definitions on UAS Sense-And-Avoid Operations in Enroute and Transition Airspace," in *2013 Aviation Technology, Integration, and Operations Conference*, Reston, Virginia: American Institute of Aeronautics and Astronautics, Aug. 2013. doi: 10.2514/6.2013-4308.

[13] T. Kotegawa, "Proof-of-concept airborne sense and avoid system with ACAS-XU flight test," *IEEE Aerospace and Electronic Systems Magazine*, vol. 31, no. 9, pp. 53–62, Sep. 2016, doi: 10.1109/MAES.2016.150163.

[14] G. Fasano, D. Accardo, A. E. Tirri, A. Moccia, and E. De Lellis, "Radar/electro-optical data fusion for non-cooperative UAS sense and avoid," *Aerosp Sci Technol*, vol. 46, pp. 436–450, Oct. 2015, doi: 10.1016/j.ast.2015.08.010.

[15] T. McCarthy, L. Pforte, and R. Burke, “Fundamental elements of an urban UTM,” *Aerospace*, vol. 7, no. 7, Jul. 2020, doi: 10.3390/AEROSPACE7070085.

[16] F. Matus, “CNS for UTM-What are some of the initial challenges we face?,” in *2018 Integrated Communications, Navigation, Surveillance Conference (ICNS)*, Herndon, VA, USA, Apr. 2018. doi: 10.1109/ICNSURV.2018.8385018.

[17] “UTM Project Technical Interchange Meeting (TIM) - NASA Aeronautics Research Institute.” Accessed: Jan. 18, 2024. [Online]. Available: https://nari.arc.nasa.gov/events/utm2021tim/

[18] B. J. Holmes and R. A. Parker, “A vision and opportunity for transformation of on-demand air mobility,” in *16th AIAA Aviation Technology, Integration, and Operations Conference*, Washington, D.C, USA , Jun. 2016. doi: 10.2514/6.2016-3465.

[19] Aubuchon Vanessa, K. Hashemi, R. Shively, and J. Wishart, “Multi-Vehicle (m:N) Operations in the NAS - NASA’s Research Plans,” in *AIAA AVIATION 2022 Forum*, Chicago, IL, USA, Jun. 2022. doi: 10.2514/6.2022-3758.

[20] “Uber Air | Uber Elevate.” Accessed: Jan. 05, 2024. [Online]. Available: https://www.uber.com/it/it/elevate/

[21] “THE PROJECT | SAFIR-Med.” Accessed: Jan. 05, 2024. [Online]. Available: https://www.safir-med.eu/project

[22] B. Allen Hamilton, “Final Report Urban Air Mobility (UAM) Market Study,” 2018.

[23] C. Xu, X. Liao, J. Tan, H. Ye, and H. Lu, “Recent Research Progress of Unmanned Aerial Vehicle Regulation Policies and Technologies in Urban Low Altitude,” *IEEE Access*, vol. 8, pp. 74175–74194, 2020, doi: 10.1109/ACCESS.2020.2987622.

[24] K. H. Goodrich and C. R. Theodore, “Description of the NASA Urban Air Mobility Maturity Level (UML) Scale,” in *AIAA Scitech 2021 Forum*, Jan. 2021. doi: 0.2514/6.2021-1627.

[25] C. W. Lum, R. Larson, W. Handley, S. Lui, and Z. Caratao, “Flight testing an ADS-B equipped sUAS in GPS-denied environments,” in *AIAA Flight Testing Conference, 2017*, Denver, Colorado, USA, Jun. 2017. doi: 10.2514/6.2017-3139.

[26] K. K. Ellis, P. Krois, J. Koelling, L. J. Prinzel, M. Davies, and R. Mah, “A Concept of Operations (ConOps) of an In-time Aviation Safety Management System (IASMS) for Advanced Air Mobility (AAM),” in *AIAA Scitech 2021 Forum*, Reston, Virginia, USA: American Institute of Aeronautics and Astronautics, Jan. 2021. doi: 10.2514/6.2021-1978.

[27] C. A. Ippolito *et al.*, “Concepts for Distributed Sensing and Collaborative Airspace Autonomy in Advanced Urban Air Mobility,” in *2023 AIAA SciTech Forum*, National Harbor, MD, USA, Jan. 2023.

[28] I. Maza, K. Kondak, M. Bernard, and A. Ollero, “Multi-UAV cooperation and control for load transportation and deployment,” *Journal of Intelligent and Robotic Systems: Theory and Applications*, vol. 57, no. 1–4, pp. 417–449, Jan. 2010, doi: 10.1007/s10846-009-9352-8.

[29] Bandala A *et al.*, “Payload Lift and Transport Using Decentralized Unmanned Aerial Vehicle Quadcopter Teams,” in *TENCON 2018 - 2018 IEEE Region 10 Conference*, Jeju, Korea (South), Oct. 2018. doi: 10.1109/TENCON.2018.8650540.

[30] J. R. Martínez-de-Dios, L. Merino, A. Ollero, L. M. Ribeiro, and X. Viegas, “Multi-UAV experiments: Application to forest fires,” *Springer Tracts in Advanced Robotics*, vol. 37, pp. 207–228, 2007, doi: 10.1007/978-3-540-73958-6_8.

[31] B. Savidge, A. Kopeikin, R. Arnold, and D. Larkin, “UAS Swarm Shares Survey Data to Expedite Coordinated Mapping of Radiation Hotspots,” in *2019 IEEE*

International Symposium on Technologies for Homeland Security (HST), Woburn, MA, USA, Nov. 2019. doi: 10.1109/HST47167.2019.9032952.

[32] C. Dumitrescu, M. Minea, I. M. Costea, I. C. Chiva, and A. Semenescu, "Development of an acoustic system for uav detection," *Sensors* , vol. 20, no. 17, pp. 1–27, Sep. 2020, doi: 10.3390/s20174870.

[33] W. Wang, K. Fan, Q. Ouyang, and Y. Yuan, "Acoustic UAV detection method based on blind source separation framework," *Applied Acoustics*, vol. 200, Nov. 2022, doi: 10.1016/j.apacoust.2022.109057.

[34] B. Harvey and S. O'young, "Acoustic detection of a fixed-wing UAV," *Drones*, vol. 2, no. 1, pp. 1–18, Mar. 2018, doi: 10.3390/drones2010004.

[35] A. Zelnio, E. Case, and B. Rigling, "A Low-Cost Acoustic Array for Detecting and Tracking Small RC Aircraft," in *2009 IEEE 13th Digital Signal Processing Workshop and 5th IEEE Signal Processing Education Workshop*, Marco Islan, FL, USA, 2009.

[36] H. Salloum, A. Sedunov, N. Sedunov, A. Sutin, and D. Masters, "Acoustic System for Low Flying Aircraft Detection," in *2015 IEEE International Symposium on Technologies for Homeland Security (HST)*, Waltham, MA, USA, 2015.

[37] C. Yuan, Z. Liu, and Y. Zhang, "Fire Detection Using Infrared Images for UAV-based Forest Fire Surveillance," in *2017 International Conference on Unmanned Aircraft Systems (ICUAS)*, Miami, FL, USA, 2017.

[38] G. Tanda, M. Balsi, P. Fallavollita, and V. Chiarabini, "A uav-based thermal-imaging approach for the monitoring of urban landfills," *Inventions*, vol. 5, no. 4, pp. 1–13, Dec. 2020, doi: 10.3390/inventions5040055.

[39] C. Jiang *et al.*, "Object detection from UAV thermal infrared images and videos using YOLO models," *International Journal of Applied Earth Observation and Geoinformation*, vol. 112, Aug. 2022, doi: 10.1016/j.jag.2022.102912.

[40] P. Andraši, T. Radišić, M. Muštra, and J. Ivošević, "Night-time Detection of UAVs using Thermal Infrared Camera," in *Transportation Research Procedia*, Elsevier B.V., 2017, pp. 183–190. doi: 10.1016/j.trpro.2017.12.184.

[41] Z. Yang, J. Lian, and J. Liu, "Infrared UAV Target Detection Based on Continuous-Coupled Neural Network," *Micromachines (Basel)*, vol. 14, no. 11, Nov. 2023, doi: 10.3390/mi14112113.

[42] J. Martin, J. Riseley, and J. J. Ford, "A Dataset of Stationary, Fixed-wing Aircraft on a Collision Course for Vision-Based Sense and Avoid," in *2022 International Conference on Unmanned Aircraft Systems, ICUAS 2022*, Dubrovnik, Croatia, Jun. 2022, pp. 144–149. doi: 10.1109/ICUAS54217.2022.9836180.

[43] "Airborne Object Tracking Dataset." Accessed: Jan. 15, 2024. [Online]. Available: https://registry.opendata.aws/airborne-object-tracking

[44] A. Coluccia *et al.*, "Drone-vs-Bird Detection Challenge at IEEE AVSS2021," in *AVSS 2021 - 17th IEEE International Conference on Advanced Video and Signal-Based Surveillance*, Washington, DC, USA, Nov. 2021. doi: 10.1109/AVSS52988.2021.9663844.

[45] L. Lu, G. Fasano, A. Carrio, M. Lei, H. Bavle, and P. Campoy, "A comprehensive survey on non-cooperative collision avoidance for micro aerial vehicles: Sensing and obstacle detection," *J Field Robot*, vol. 40, no. 6, pp. 1697–1720, Sep. 2023, doi: 10.1002/rob.22189.

[46] J. M. Loffi, S. M. Vance, J. Jacob, L. Spaulding, and J. C. Dunlap, "Evaluation of Onboard Detect-and-Avoid System for sUAS BVLOS Operations," *International*

Journal of Aviation, Aeronautics, and Aerospace, vol. 9, no. 2, 2022, doi: 10.15394/ijaaa.2022.1701.

[47] "Iris Automation | Casia Detect-and-Avoid." Accessed: Dec. 09, 2022. [Online]. Available: https://www.irisonboard.com/casia/ .

[48] J. Lai, L. Mejias, and J. J. Ford, "Airborne vision-based collision-detection system," *J Field Robot*, vol. 28, no. 2, pp. 137–157, Mar. 2011, doi: 10.1002/rob.20359.

[49] J. Lai, J. J. Ford, L. Mejias, and P. O'Shea, "Characterization of sky-region morphological-temporal airborne collision detection," *J Field Robot*, vol. 30, no. 2, pp. 171–193, Mar. 2013, doi: 10.1002/rob.21443.

[50] D. Bratanov, L. Mejias, and J. J. Ford, "A vision-based sense-and-avoid system tested on a ScanEagle UAV," in *2017 International Conference on Unmanned Aircraft Systems (ICUAS)*, Miami, FL, USA, 2017. doi: 10.1109/ICUAS.2017.7991302.

[51] A. Nussberger, H. Grabner, and L. Van Gool, "Aerial Object Tracking from an Airborne Platform," in *2014 International Conference on Unmanned Aircraft Systems (ICUAS)*, Orlando, FL, USA, 2014. doi: 10.1109/ICUAS.2014.6842386.

[52] C. V Dolph *et al.*, "Sense and Avoid for Small Unmanned Aircraft Systems," in *AIAA Information Systems-AIAA Infotech @ Aerospace*, Grapevine, TX, USA, 2017. doi: 10.2514/6.2017-1151.

[53] J. Shi and C. Tomasi, "Good Features to Track," in *IEEE Computer Society Conference on Computer Vision and Pattern Recognition*, Publ by IEEE, 1994, pp. 593–600. doi: 10.1109/cvpr.1994.323794.

[54] H. Bay, T. Tuytelaars, and L. Van Gool, "SURF: Speeded Up Robust Features," in *European Conference on Computer Vision (ECCV)*, Graz, Austria, May 2006, pp. 404–417.

[55] E. Rosten and T. Drummond, "Machine Learning for High-Speed Corner Detection," in *European Conference on Computer Vision (ECCV)*, 2006, pp. 430–443.

[56] C. Dolph, L. Glaab, B. Allen, M. Consiglio, and K. Iftekharuddin, "An Improved Far-Field Small Unmanned Aerial System Optical Detection Algorithm," in *2019 IEEE/AIAA 38th Digital Avionics Systems Conference (DASC)*, San Diego, CA, USA, 2019. doi: 10.1109/DASC43569.2019.9081609.

[57] J. James, J. J. Ford, and T. L. Molloy, "Below Horizon Aircraft Detection Using Deep Learning for Vision-Based Sense and Avoid," in *2019 International Conference on Unmanned Aircraft Systems (ICUAS)*, Atlanta, GA, USA, Mar. 2019. doi: 10.1109/ICUAS.2019.8798096.

[58] U. Seidaliyeva, D. Akhmetov, L. Ilipbayeva, and E. T. Matson, "Real-time and accurate drone detection in a video with a static background," *Sensors*, vol. 20, no. 14, pp. 1–18, Jul. 2020, doi: 10.3390/s20143856.

[59] A. Schumann, L. Sommer, J. Klatte, T. Schuchert, and J. Beyerer, "Deep Cross-Domain Flying Object Classification for Robust UAV Detection," in *2017 14th IEEE International Conference on Advanced Video and Signal Based Surveillance (AVSS)*, Lecce, Italy, Aug. 2017. doi: 10.1109/AVSS.2017.8078558.

[60] Y. Lyu, Q. Pan, C. Zhao, H. Zhu, T. Tang, and Y. Zhang, "A Vision Based Sense and Avoid System for Small Unmanned Helicopter," in *2015 International Conference on Unmanned Aircraft Systems, ICUAS 2015*, Institute of Electrical and Electronics Engineers Inc., Jul. 2015, pp. 586–592. doi: 10.1109/ICUAS.2015.7152339.

[61] C. Briese, A. Seel, and F. Andert, "Vision-based detection of non-cooperative UAVs using frame differencing and temporal filter," in *2018 International Conference on Unmanned Aircraft Systems (ICUAS)*, Dallas, TX, USA, Jun. 2018. doi: 10.1109/ICUAS.2018.8453372.

[62] R. Opromolla and G. Fasano, “Visual-based obstacle detection and tracking, and conflict detection for small UAS sense and avoid,” *Aerosp Sci Technol*, vol. 119, Dec. 2021, doi: 10.1016/j.ast.2021.107167.

[63] J. Zhang and S. Singh, “LOAM: Lidar Odometry and Mapping in Real-time,” in *Robotics: Science and Systems Conference 2014* , 2014.

[64] S. Hening, C. Ippolito, K. Krishnakumar, V. Stepanyan, and M. Teodorescu, “3D LiDAR SLAM integration with GPS/INS for UAVs in urban GPS-degraded environments,” in *AIAA Information Systems-AIAA Infotech at Aerospace, 2017*, American Institute of Aeronautics and Astronautics Inc, AIAA, 2017. doi: 10.2514/6.2017-0448.

[65] S. Zhang, L. Xiao, Y. Nie, B. Dai, and C. Hu, “Lidar Odometry and Mapping Based on Two-stage Feature Extraction; Lidar Odometry and Mapping Based on Two-stage Feature Extraction,” 2020.

[66] T. A. Abir, E. Kuantama, R. Han, J. Dawes, R. Mildren, and P. Nguyen, “Towards Robust Lidar-based 3D Detection and Tracking of UAVs,” in *DroNet 2023 - Proceedings of the 9th ACM Workshop on Micro Aerial Vehicle Networks, Systems, and Applications*, Association for Computing Machinery, Inc, Jun. 2023, pp. 1–7. doi: 10.1145/3597060.3597236.

[67] Uijt de Haag Maarten, Bartone Chris G., and Braasch Michael S., “Flight-Test Evaluation of Small Form-Factor LiDAR and Radar Sensors for sUAS Detect-and-Avoid Applications,” in *2016 IEEE AIAA 35th Digital Avionics Systems Conference (DASC)*, Sacramento, CA, USA, Sep. 2016. doi: 10.1109/DASC.2016.7778108.

[68] M. Vrba *et al.*, “On Onboard LiDAR-based Flying Object Detection,” *arXiv preprint 2303.05404*, Mar. 2023, [Online]. Available: http://arxiv.org/abs/2303.05404

[69] S. Ramasamy, R. Sabatini, A. Gardi, and J. Liu, “LIDAR obstacle warning and avoidance system for unmanned aerial vehicle sense-and-avoid,” *Aerosp Sci Technol*, vol. 55, pp. 344–358, Aug. 2016, doi: 10.1016/j.ast.2016.05.020.

[70] E. Aldao, L. M. González-de Santos, and H. González-Jorge, “LiDAR Based Detect and Avoid System for UAV Navigation in UAM Corridors,” *Drones*, vol. 6, no. 8, Aug. 2022, doi: 10.3390/drones6080185.

[71] M. Ritchie, F. Fioranelli, H. Griffiths, and B. Torvik, “Micro-drone RCS analysis,” in *2015 IEEE Radar Conference*, Johannesburg, South Africa, Oct. 2015. doi: 10.1109/RadarConf.2015.7411926.

[72] V. Semkin *et al.*, “Analyzing Radar Cross Section Signatures of Diverse Drone Models at mmWave Frequencies,” *IEEE Access*, vol. 8, pp. 48958–48969, 2020, doi: 10.1109/ACCESS.2020.2979339.

[73] G. Galati *et al.*, “Visibility Trials of Unmanned Aerial Vehicles (Drones) by commercial X-Band Radar in Sub-urban Environment,” in *2017 AEIT International Annual Conference*, Cagliari, Italy, Sep. 2017. doi: 10.23919/AEIT.2017.8240554.

[74] F. Paonessa *et al.*, “UAV-mounted Corner Reflector for In-Situ Radar Verification and Calibration,” in *2018 IEEE Conference on Antenna Measurements & Applications (CAMA)*, Vasteras, Sweden, Sep. 2018. doi: 10.1109/CAMA.2018.8530616.

[75] H. G. McClelland *et al.*, “Small aircraft flight encounters database for UAS sense and avoid,” in *AIAA Information Systems-AIAA Infotech at Aerospace, 2017*, Grapevine, TX, USA: American Institute of Aeronautics and Astronautics Inc, AIAA, Jan. 2017. doi: 10.2514/6.2017-1152.

[76] P. Pierre, P. Michel, and L. Patrick, “Challenges in Detecting UAS with Radar,” in *2017 International Carnahan Conference on Security Technology (ICCST)*,

[77] "AiRanger™ UAS NASA SIO Program Final Report." [Online]. Available: http://www.sti.nasa.gov

[78] W. Chekkar, J. Lanteri, J. Marot, and C. Migliaccio, "Clutter Removal for Detection of Slow-moving Targets with a 76-81 GHz FMCW Radar," in *2021 IEEE Conference on Antenna Measurements and Applications, CAMA 2021*, Antibes Juan-les-Pins, France: Institute of Electrical and Electronics Engineers Inc., Nov. 2021, pp. 409–412. doi: 10.1109/CAMA49227.2021.9703653.

[79] C. Liang, N. Cao, X. Lu, and Y. Ye, "UAV Detection Using Continuous Wave Radar," in *2018 IEEE International Conference on Information Communication and Signal Processing (ICSP 2018)*, Singapore, Sep. 2018. doi: 10.1109/ICICSP.2018.8549736.

[80] C. Zhou, Y. Liu, and Y. Song, "Detection and tracking of a UAV via hough transform," in *2016 CIE International Conference on Radar, RADAR 2016*, Guangzhou, China: Institute of Electrical and Electronics Engineers Inc., Oct. 2017. doi: 10.1109/RADAR.2016.8059453.

[81] S. Rudys, P. Ragulis, A. Laučys, D. Bručas, R. Pomarnacki, and D. Plonis, "Investigation of UAV Detection by Different Solid-State Marine Radars," *Electronics (Basel)*, vol. 11, no. 16, Aug. 2022, doi: 10.3390/electronics11162502.

[82] G. Szatkowski, A. Kriz, L. Ticatch, R. Briggs, J. Coggin, and C. Morris, "Airborne Radar for sUAS Sense and Avoid," in *2019 IEEE/AIAA 38th Digital Avionics Systems Conference (DASC)*, San Diego, CA, USA, Sep. 2019. doi: 10.1109/DASC43569.2019.9081656.

[83] P. J. B. Morris and K. V. S. Hari, "Detection and Localization of Unmanned Aircraft Systems Using Millimeter-Wave Automotive Radar Sensors," *IEEE Sens Lett*, vol. 5, no. 6, Jun. 2021, doi: 10.1109/LSENS.2021.3085087.

[84] L. R. Sahawneh *et al.*, "A Ground-Based Sense-and-Avoid System for Small Unmanned Aircraft," *Journal of Aerospace Information Systems*, vol. 15, 2018, doi: 10.2514/1.I010627.

[85] A. Johnson and A. Kurumunda, "Using automotive radar to enable detection and tracking of small UAVs," in *AIAA SCITECH 2023 Forum*, National Harbor, MD, Jan. 2023. doi: 10.2514/6.2023-1810.

[86] S. Rahman and D. A. Robertson, "Radar micro-Doppler signatures of drones and birds at K-band and W-band," *Sci Rep*, vol. 8, no. 1, Dec. 2018, doi: 10.1038/s41598-018-35880-9.

[87] D. Raval, E. Hunter, S. Hudson, A. Damini, and B. Balaji, "Convolutional neural networks for classification of drones using radars," *Drones*, vol. 5, no. 4, Dec. 2021, doi: 10.3390/drones5040149.

[88] B. K. Kim, H. S. Kang, and S. O. Park, "Drone classification using convolutional neural networks with merged doppler images," *IEEE Geoscience and Remote Sensing Letters*, vol. 14, no. 1, pp. 38–42, Jan. 2017, doi: 10.1109/LGRS.2016.2624820.

[89] J. Dudczyk, R. Czyba, and K. Skrzypczyk, "Multi-Sensory Data Fusion in Terms of UAV Detection in 3D Space," *Sensors*, vol. 22, no. 12, Jun. 2022, doi: 10.3390/s22124323.

[90] S. Ramasamy, R. Sabatini, and A. Gardi, "Avionics Sensor Fusion for Small Size Unmanned Aircraft Sense-and-Avoid," in *2014 IEEE International Workshop on Metrology for Aerospace (MetroAeroSpace)*, Benevento, Italy, May 2014, p. 632. doi: 10.1109/MetroAeroSpace.2014.6865933.

[91] F. Svanström, C. Englund, and F. Alonso-Fernandez, "Real-time drone detection and tracking with visible, thermal and acoustic sensors," in *Proceedings - International*

Conference on Pattern Recognition, Institute of Electrical and Electronics Engineers Inc., 2020, pp. 7265–7272. doi: 10.1109/ICPR48806.2021.9413241.

[92] F. Svanström, F. Alonso-Fernandez, and C. Englund, "Drone Detection and Tracking in Real-Time by Fusion of Different Sensing Modalities," *Drones*, vol. 6, no. 11, p. 317, Oct. 2022, doi: 10.3390/drones6110317.

[93] J. Kim *et al.*, "Deep Learning Based Malicious Drone Detection Using Acoustic and Image Data," in *2022 6th IEEE International Conference on Robotic Computing, IRC 2022*, Italy: Institute of Electrical and Electronics Engineers Inc., Dec. 2022, pp. 91–92. doi: 10.1109/IRC55401.2022.00024.

[94] B. Pardhasaradhi and L. R. Cenkeramaddi, "GPS Spoofing Detection and Mitigation for Drones Using Distributed Radar Tracking and Fusion," *IEEE Sens J*, vol. 22, no. 11, pp. 11122–11134, Jun. 2022, doi: 10.1109/JSEN.2022.3168940.

[95] E. Kawamura, K. Kannan, T. Lombaerts, V. Stepanyan, C. Dolph, and C. Ippolito, "Ground-Based Vision Tracker for Advanced Air Mobility and Urban Air Mobility," in *AIAA SCITECH 2024 Forum*, Orlando, FL, Jan. 2024. doi: 10.2514/6.2024-2010.

[96] C. V. Dolph *et al.*, "Ground to air testing of a fused optical-radar aircraft detection and tracking system," in *AIAA Science and Technology Forum and Exposition, AIAA SciTech Forum 2022*, American Institute of Aeronautics and Astronautics Inc, AIAA, 2022. doi: 10.2514/6.2022-0498.

[97] T. Lombaerts *et al.*, "Distributed Ground Sensor Fusion Based Object Tracking for Autonomous Advanced Air Mobility Operations," in *AIAA SCITECH 2023 Forum*, National Harbor, MD, Jan. 2023. doi: 10.2514/6.2023-0896.

[98] C. Huang, I. Petrunin, and A. Tsourdos, "Radar-Camera Fusion for Ground-based Perception of Small UAV in Urban Air Mobility," in *2023 IEEE 10th International Workshop on Metrology for AeroSpace, MetroAeroSpace 2023 - Proceedings*, Institute of Electrical and Electronics Engineers Inc., 2023, pp. 395–400. doi: 10.1109/MetroAeroSpace57412.2023.10189934.

[99] R. Opromolla, G. Fasano, and D. Accardo, "Perspectives and Sensing Concepts for Small UAS Sense and Avoid," in *2018 IEEE/AIAA 37th Digital Avionics Systems Conference (DASC)*, London, UK, Sep. 2018. doi: 10.1109/DASC.2018.8569338.

[100] F. Causa, R. Opromolla, and G. Fasano, "Cooperative navigation and visual tracking with passive ranging for UAV flight in GNSS-challenging environments," in *2021 International Conference on Unmanned Aircraft Systems, ICUAS 2021*, Athens, Greece: Institute of Electrical and Electronics Engineers Inc., Jun. 2021, pp. 1538–1547. doi: 10.1109/ICUAS51884.2021.9476681.

[101] J. Redmon and A. Farhadi, "YOLO9000: Better, Faster, Stronger," in *2017 IEEE Conference on Computer Vision and Pattern Recognition (CVPR)*, Honolulu, HI, 2017. doi: 10.1109/CVPR.2017.690.

[102] S. Scholes, A. Ruget, G. Mora-Martin, F. Zhu, I. Gyongy, and J. Leach, "DroneSense: The Identification, Segmentation, and Orientation Detection of Drones via Neural Networks," *IEEE Access*, vol. 10, pp. 38154–38164, 2022, doi: 10.1109/ACCESS.2022.3162866.

[103] Y. Cai, O. Krasnov, and A. Yarovoy, "Simulation of Radar Micro-Doppler Patterns for Multi-Propeller Drones," in *2019 International Radar Conference, RADAR 2019*, Toulon, France: Institute of Electrical and Electronics Engineers Inc., Sep. 2019. doi: 10.1109/RADAR41533.2019.171372.

[104] "EchoFlight | Echodyne - Echodyne." Accessed: Mar. 11, 2024. [Online]. Available: https://www.echodyne.com/radar-solutions/echoflight/

[105] "Blackfly S USB3 | Teledyne FLIR." Accessed: Jan. 20, 2024. [Online]. Available: https://www.flir.it/products/blackfly-s-usb3/?model=BFS-U3-31S4C-C&vertical=machine+vision&segment=iis

[106] A. Yasuda and T. Takasu, "Development of the low-cost RTK-GPS receiver with an open source program package RTKLIB," 2009. [Online]. Available: https://www.researchgate.net/publication/228811569

[107] M. D. Shuster and S. D. Oh, "Three-axis attitude determination from vector observations," *Journal of Guidance, Control, and Dynamics*, vol. 4, no. 1, pp. 70–77, 1981, doi: 10.2514/3.19717.

[108] S. Blackman and R. Popoli, *Design And Analysis of Modern Tracking Systems*. Artech House Publishers, 1999.

[109] R. E. Kalman, "A New Approach to Linear Filtering and Prediction Problems," *Journal of Basic Engineering*, vol. 82, no. 1, pp. 35–45, 1960, doi: 10.1115/1.3662552.

[110] R. A. Singer, "Estimating Optimal Tracking Filter Performance for Manned Maneuvering Targets," *IEEE Transactions on Aerospace and Electronic Systems*, vol. AES-6, no. 4, pp. 473–483, 1970, doi: 10.1109/TAES.1970.310128.

[111] J.-Y. Bouguet, "Camera Calibration Toolbox for Matlab (1.0). CaltechDATA.," 2022, Accessed: Jan. 03, 2023. [Online]. Available: https://doi.org/10.22002/D1.20164

[112] G. Fasano, D. Accardo, A. E. Tirri, A. Moccia, and E. De Lellis, "Sky Region Obstacle Detection and Tracking for Vision-Based UAS Sense and Avoid," *Journal of Intelligent and Robotic Systems: Theory and Applications*, vol. 84, no. 1–4, pp. 121–144, Dec. 2016, doi: 10.1007/s10846-015-0285-0.

[113] R. C. Gonzalez, R. E. Woods, and P. Prentice Hall, *Digital Image Processing Third Edition*. Pearson, 2007.

[114] T. Kirubarajan, Y. Bar-Shalom, W. D. Blair, and G. A. Watson, "IMMPDAF for radar management and tracking benchmark with ECM," *IEEE Trans Aerosp Electron Syst*, vol. 34, no. 4, pp. 1115–1134, 1998, doi: 10.1109/7.722696.

[115] G. Fasano and R. Opromolla, "Analytical Framework for Sensing Requirements Definition in Non-Cooperative UAS Sense and Avoid," *Drones*, vol. 7, no. 10, Oct. 2023, doi: 10.3390/drones7100621.

[116] M. W. M. Edwards and J. K. Mackay, "Determining Required Surveillance Performance for Unmanned Aircraft Sense and Avoid," in *17th AIAA Aviation Technology, Integration, and Operations Conference*, Denver, CO, USA, Jun. 2017. doi: 10.2514/6.2017-4385.

[117] D. L. (David L. Hall and James. Llinas, "Handbook of multisensor data fusion," *Journal of Basic Engineering*, vol. 82, no. 1, pp. 35–45, 1960, doi: 10.1115/1.3662552.

[118] D. G. Danu, "Track Fusion in Multisensor-Multitarget Tracking," PhD dissertation, McMaster University, Hamilton, Ontario, Canada, 2011.

[119] C.-Y. Chong, S. Mori, W. H. Barker, and K.-C. Chang, "Architectures and Algorithms Track Association and Fusion," *IEEE Aerospace and Electronic Systems Magazine*, vol. 15, no. 1, pp. 5–13, Jan. 2000, doi: 10.1109/62.821657.

[120] D.C. Brown, "Decentering Distortion of Lenses," *Photometric Engineering*, vol. 32, no. 3, pp. 444–462, 1966.

[121] "Sense And Avoid (SAA) for unmanned aircraft systems (UAS)," *FAA sponsored Sense And Avoid Workshop*. Oct. 2009.

[122] M. Mallick, K. C. Chang, S. Arulampalam, and Y. Yan, "Heterogeneous Track-to-Track Fusion in 3-D Using IRST Sensor and Air MTI Radar," *IEEE Trans Aerosp Electron Syst*, vol. 55, no. 6, pp. 3062–3079, Dec. 2019, doi: 10.1109/TAES.2019.2898302.

[123] X. Tian, T. Yuan, and Y. Bar-Shalom, "Track-to-Track Fusion in Linear and Nonlinear Systems," in *Advances in Estimation, Navigation, and Spacecraft Control*, Springer Berlin Heidelberg, 2015, pp. 21–41. doi: 10.1007/978-3-662-44785-7_2.

[124] G. E. Gorospe, C. Ippolito, and K. Hashemi, "Distributed Sensing and Reasoning for Advanced Air Mobility Health Management and Mission Assurance," in *AIAA AVIATION 2023 Forum*, San Diego, CA, USA, Jun. 2023. doi: 10.2514/6.2023-3323.

[125] V. Stepanyan, K. Kannan, E. T. Kawamura, T. Lombaerts, and C. Ippolito, "Distributed Target Tracking With Optimal Data Migration," in *2023 AIAA SciTech Forum*, National Harbor, MD, US, Jan. 2023. doi: 10.2514/6.2023-2194.

[126] V. Stepanyan, C. Ippolito, E. T. Kawamura, and T. Lombaerts, "Optimal Sensor Mobility Design for Target Tracking with Distributed Sensing, Communication and Computing Infrastructure," in *AIAA SCITECH 2024 Forum*, Orlando, FL, USA, Jan. 2024. doi: 10.2514/6.2024-1778.

[127] T. Lombaerts *et al.*, "Development and Field Test Results of Distributed Ground-Based Sensor Fusion Object Tracking," in *AIAA SCITECH 2024 Forum*, Orlando, FL, Jan. 2024. doi: 10.2514/6.2024-1389.

[128] C. A. Ippolito *et al.*, "Adaptive Sensor Registration Across Distributed Airspace Surveillance Networks," in *AIAA SCITECH 2024 Forum*, Orlando, FL, Jan. 2024. doi: 10.2514/6.2024-1779.

[129] L. J. Glaab, M. A. Johnson, R. G. McSwain, S. C. Geuther, Q. V. Dao, and J. R. Homola, "The High Density Vertiplex Advanced Onboard Automation Overview," in *AIAA/IEEE Digital Avionics Systems Conference - Proceedings*, Portsmouth, VA, USA: Institute of Electrical and Electronics Engineers Inc., Sep. 2022. doi: 10.1109/DASC55683.2022.9925834.

[130] J. Brown, "CERTAIN City Environment Range Testing for Autonomous Integrated Navigation," 2016. Accessed: Jul. 12, 2023. [Online]. Available: https://ntrs.nasa.gov/citations/20160009254

[131] C. V Dolph *et al.*, "Distributed Sensor Fusion of Ground and Air Nodes using Vision and Radar Modalities for Tracking Multirotor Small Uncrewed Air Systems and Birds," in *AIAA SCITECH 2024 Forum*, Orlando, FL, USA, Jan. 2024. doi: 10.2514/6.2024-1781.

[132] C. V Dolph, C. Minwalla, L. J. Glaab, M. J. Logan, B. D. Allen, and K. M. Iftekharuddin, "Detection and Tracking of Aircraft in the Far-Field from Small Unmanned Aerial Systems Senior Technologist for Intelligent Flight Systems, AIAA Associate Fellow," *Journal of Aerospace Information Systems*, vol. 18, no. 11, 2021, doi: 10.2514/1.I010911.

[133] J. Munkres, "Algorithms for the Assignment and Transportation Problems," *Journal of the Society for Industrial and Applied Mathematics*, vol. 5, no. 1, pp. 32–38, 1957.

[134] A. R. Vetrella, F. Causa, A. Renga, G. Fasano, D. Accardo, and M. Grassi, "Multi-UAV Carrier Phase Differential GPS and Vision-based Sensing for High Accuracy Attitude Estimation," *Journal of Intelligent and Robotic Systems: Theory and Applications*, vol. 93, no. 1–2, pp. 245–260, Feb. 2019, doi: 10.1007/s10846-018-0821-9.

[135] A. R. Vetrella, G. Fasano, and D. Accardo, "Attitude estimation for cooperating UAVs based on tight integration of GNSS and vision measurements," *Aerosp Sci Technol*, vol. 84, pp. 966–979, Jan. 2019, doi: 10.1016/j.ast.2018.11.032.

[136] R. Opromolla, G. Esposito, and G. Fasano, “In-flight estimation of magnetic biases on board of small UAVs exploiting cooperation,” in *2019 IEEE International Workshop on Metrology for AeroSpace (MetroAeroSpace)*, Torino, Italy, Jun. 2019.

[137] R. Opromolla, “Magnetometer calibration for small unmanned aerial vehicles using cooperative flight data,” *Sensors (Switzerland)*, vol. 20, no. 2, Jan. 2020, doi: 10.3390/s20020538.

[138] H. P. Gavin, “The Levenberg-Marquardt algorithm for nonlinear least squares curve-fitting problems.” Accessed: Jan. 26, 2024. [Online]. Available: https://people.duke.edu/~hpgavin/ExperimentalSystems/lm.pdf

[139] G. Lu and M. E. Cannon, “Attitude determination using a multi-antenna gps system for hydrographic applications,” *Marine Geodesy*, vol. 17, no. 4, pp. 237–250, 1994, doi: 10.1080/15210609409379733.

[140] J. Fang, H. Sun, J. Cao, X. Zhang, and Y. Tao, “A novel calibration method of magnetic compass based on ellipsoid fitting,” *IEEE Trans Instrum Meas*, vol. 60, no. 6, pp. 2053–2061, Jun. 2011, doi: 10.1109/TIM.2011.2115330.

[141] J. F. Vasconcelos, G. Elkaim, C. Silvestre, P. Oliveira, and B. Cardeira, “Geometric Approach to Strapdown Magnetometer Calibration in Sensor Frame,” *IEEE Transactions on Aerospace and Electronic Systems* , vol. 47, no. 2, pp. 1293–1306, 2011, doi: 10.1109/TAES.2011.5751259.

[142] H. Wu, X. Pei, J. Li, H. Gao, and Y. Bai, “An improved magnetometer calibration and compensation method based on Levenberg–Marquardt algorithm for multi-rotor unmanned aerial vehicle,” *Measurement and Control (United Kingdom)*, vol. 53, no. 3–4, pp. 276–286, Mar. 2020, doi: 10.1177/0020294019890627.

[143] M. Chodnicki, M. Mazur, M. Nowakowski, and G. Kowaleczko, “Algorithms for the detection and compensation interferance of magnetic field measurement,” in *2018 5th IEEE International Workshop on Metrology for AeroSpace (MetroAeroSpace)*, Rome, Italy, Jun. 2018. doi: 10.1109/MetroAeroSpace.2018.8453528.

[144] T. Lee and A. Canciani, “MagSLAM: Aerial Simultaneous Localization and Mapping Using Earth’s Magnetic Anomaly Field,” *Journal of the Institute of Navigation*, vol. 67, no. 1, pp. 95–107, 2020, doi: 10.1002/navi.352.

[145] M. Funaki *et al.*, “Small unmanned aerial vehicles for aeromagnetic surveys and their flights in the South Shetland Islands, Antarctica,” *Polar Sci*, vol. 8, no. 4, pp. 342–356, Dec. 2014, doi: 10.1016/j.polar.2014.07.001.

[146] V. Schmidt, M. Becken, and J. Schmalzl, “A UAV-borne magnetic survey for archaeological prospection of a Celtic burial site,” *First Break*, vol. 38, no. 8, pp. 61–66, Aug. 2020, doi: 10.3997/1365-2397.fb2020061.

[147] R. Jackisch *et al.*, “Drone-borne hyperspectral and magnetic data integration: Otanmäki Fe-Ti-V deposit in Finland,” *Remote Sens (Basel)*, vol. 11, no. 18, Sep. 2019, doi: 10.3390/rs11182084.

[148] P. Le Maire, L. Bertrand, M. Munschy, M. Diraison, and Y. Géraud, “Aerial magnetic mapping with a UAV and a fluxgate magnetometer: a new method for rapid mapping and upscaling from the field to regional scale”, doi: https://doi.org/10.1111/1365-2478.12991.

[149] P. Furgale, J. Rehder, and R. Siegwart, “Unified Temporal and Spatial Calibration for Multi-Sensor Systems,” in *2013 IEEE/RSJ International Conference on Intelligent Robots and Systems*, Tokyo, Japan, Nov. 2013. doi: 10.1109/IROS.2013.6696514.

[150] “National Center for Environmental Information. Magnetic Declination Calculator.” Accessed: Jan. 26, 2024. [Online]. Available: https//www.ngdc.noaa. gov/geomag/calculators/magcalc.shtml

[151] R. Opromolla, G. Inchingolo, and G. Fasano, “Airborne visual detection and tracking of cooperative UAVs exploiting deep learning,” *Sensors (Switzerland)*, vol. 19, no. 19, Oct. 2019, doi: 10.3390/s19194332.